

Deciphering the Mysteries of Hailstone formation: Linking satellite and physicochemical studies of hail in Argentina

By
Anthony Crespo Bernal Ayala

A dissertation submitted in partial fulfillment of
the requirements for the degree of

Doctor of Philosophy
(Atmospheric and Oceanic Sciences)

at the
UNIVERSITY OF WISCONSIN-MADISON
2025

Date of final oral examination: 03/03/2025

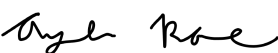
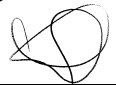
The dissertation is approved by the following members of the Final Oral Committee:
Angela K. Rowe, Professor, Atmospheric and Oceanic Sciences (AOS)
Lucia E. Arena, Professor Emeritus, AOS and Universidad Nacional de Córdoba
William O. Nachlas, Assistant Scientist, Department of Geosciences
Ankur R. Desai, Professor, AOS
Tristan L'Ecuyer, Professor, AOS
Ana Carolina Amarillo, Department of Physical and Chemical Sciences, University of L'Aquila

Dissertation Declaration and Approval

I, Anthony Crespo Bernal Ayala, declare that this Dissertation titled 'Deciphering the Mysteries of Hailstone Formation: Linking Satellite and Physicochemical Studies of Hail in Argentina' and the work presented in it are my own.

Anthony Crespo Bernal Ayala		05/01/2025
Author	Signature	Date

I hereby approve and recommend for acceptance this work in partial fulfillment of the requirements for the degree of Doctor of Philosophy:

Angela K Rowe		03/10/2025
Committee Chair	Signature	Date
Lucia E. Arena		03/03/2025
Outside Member	Signature	Date
William O. Nachlas		03/08/2025
Outside Member	Signature	Date
Ankur R. Desai		March 7, 2025
Faculty Member	Signature	Date
Tristan L'Ecuyer	TRISTAN L'ECUYER 	7 March, 2025
Faculty Member	Signature	Date
Ana C. Amarillo		03/05/2025
Outside Member	Signature	Date

Abstract

Deciphering the Mysteries of Hailstone formation: Linking satellite and physicochemical studies of hail in Argentina

by Anthony Crespo Bernal Ayala

This dissertation advances our understanding of hail formation processes and environments in Argentina, a global hail hotspot, through a multi-scale analysis spanning from individual particles to storm-scale characteristics. First, we introduce an innovative microscopy analysis methodology that preserves in situ non-soluble particles within hailstones using a protective porous plastic coating. This method combines confocal laser scanning microscopy and scanning electron microscopy with energy-dispersive spectroscopy to analyze particle characteristics while maintaining their spatial distribution within the hailstone structure.

Applying this methodology to hailstones collected in central Argentina reveals how different storm modes access distinct particle populations. In supercell environments with strong upslope flow, particles originate primarily from local sources, while organized systems associated with the South American Low-Level Jet incorporate particles from more distant regions. Particle sizes reach 256 microns, with agglomerated mineral/organic particles dominating the composition, demonstrating how regional land use patterns influence potential ice nuclei availability.

We then examine environmental conditions supporting hail production by combining GOES-East Overshooting Top detections with Global Precipitation Measurement Dual-frequency Precipitation Radar (GPM-DPR) hail detection data (2014-2022). Larger and deeper OTs occur in environments characterized by higher moisture content and elevated wet bulb zero heights, particularly when combined with steeper mid-level lapse rates. The strong negative correlation between OT area and IR-tropopause temperature difference ($r = -0.72$) indicates that larger OTs consistently achieve deeper penetration. Environmental conditions show distinct diurnal patterns, supporting both afternoon discrete storms with peak MUCAPE (~ 3000 J/kg) and nocturnal organized systems with enhanced wind shear (median ~ 16 m/s in hail-matched cases). These patterns reveal how Argentina's hail-producing environments support a broader range of storm modes compared to U.S. storms. The diversity in storm modes and environmental conditions helps explain why Argentina experiences significant hail production across a wider variety of atmospheric conditions, particularly through the interaction between the South American Low-Level Jet and local terrain features.

This research provides new insights into how particle characteristics and environmental conditions interact to support hail formation in Argentina while developing methodological approaches that can be applied to study severe storms in other traditionally under-observed regions globally.

"No solo las grandes mentes cambian este mundo, sino aquellas que creen en él, crecen con él y trabajan para convertirlo en un lugar limpio, seguro y feliz para vivir."

"Not only do great minds change this world, but also those who believe in it, grow with it, and work to make it a clean, safe, and happy place to live."

Anthony Crespo Bernal Ayala

Acknowledgments

Growing up in the small town of Caguas, Puerto Rico, I could only dream of the amazing things I have been fortunate enough to accomplish today. Becoming an early-career scientist is not a journey one can undertake alone. I am blessed to have had so many extraordinary people along the way who helped me achieve this milestone. To them, I dedicate this section of my dissertation.

First, I want to honor an incredible woman, my mother. A mother of three who, against all odds, raised a remarkable family. She was a warrior, a role model, and someone I am proud to call my mother. Her independence, dedication, and adaptability shaped me into the scientist I am today. Alongside her stands my family, the Ayala family, who have supported me from afar, always paying attention to my progress. With this work, I want to make them proud and shine our last name across the world.

I would also like to express my gratitude to the teachers who inspired me during high school at CIMATEC. Even after ten years, they still follow my progress and continue to cheer me on. Their dedication planted the seeds that gave me the tools to become the scientist I am today. A special thank you goes to Eva Torres, who has cherished my achievements as a young scientist just as she did when I was her student in high school.

Like every other scientist, my undergraduate experience was pivotal in shaping the work presented in this dissertation. If it weren't for Dr. Jay Thomas, whose contagious curiosity and exceptional teaching in petrology inspired me, I wouldn't have dared pursue what seemed impossible back then but has now become an incredible opportunity to better understand our planet. During that time, I also had the privilege of meeting Dr. William O. Nachlas, who was then Dr. Thomas's postdoc. It feels like a small world that he later ended up at UW-Madison, where we reconnected, and I had the opportunity to share my thesis with him. Dr. Nachlas played a significant role in shaping the geological aspects of this dissertation, and for that, I am deeply grateful.

Continuing on this journey, I want to thank Dr. Ankur R. Desai. Not only did he provide an amazing introduction to Madison, but his unconditional support allowed me to pursue what I was most passionate about. He found and recommended the opportunity to be part of the RELAMPAGO field campaign, a transformative experience that solidified my research interests and opened doors to the work discussed here.

Through RELAMPAGO, I had the honor of meeting Dr. Lucia E. Arena. Dr. Arena not only became a member of my master's and PhD committees but also welcomed me into her home, trained me in ice physics, and shared her curiosity about the world in ways I never imagined until I met her.

This journey ultimately led me to my advisor, Dr. Angela K. Rowe. Who would've thought that across continents, I would meet such an extraordinary mentor? Dr. Rowe's kind heart profoundly impacted my development as a scientist. Her constant growth alongside her students, her unwavering support, and her sensitivity beyond academia inspire everyone who works with her and undoubtedly inspire me.

I want to extend my heartfelt thanks to my PhD committee members: Angela K. Rowe, Lucia E. Arena, Ankur R. Desai, William O. Nachlas, Tristan L'Ecuyer, and Ana C. Amarillo. Your guidance and expertise have been invaluable throughout this journey. Each of you has contributed uniquely to shaping this dissertation and supporting my growth as a researcher.

I also want to thank the RELAMPAGO team, which includes members from the University of Washington and Colorado State University. A special thanks goes to Kristen Rasmussen; back in Argentina at a coffee shop, during a simple conversation about what was then just a dream for my master's and PhD work, she encouraged me and reinforced that even the sky wasn't the limit.

I extend my gratitude to my team at the Laboratorio de Análisis de Materiales por Espectrometría de Rayos X (LAMARX). Special thanks go to Sebastián García for his invaluable help during the initial stages of this project, particularly Chapter 1, and for sharing his expertise in material sciences that greatly contributed to its development. My heartfelt thanks also go to María José Cabrera for her constant support during remote analyses and for ensuring uninterrupted services throughout this process. To each operator who assisted with my analyses: your unique contributions made this experience both productive and enriching.

I am deeply grateful to Universidad Nacional de Córdoba for their hospitality and for granting me visiting researcher status, a privilege that enabled significant progress in this work through their facilities and support.

I would like to acknowledge funding from the National Science Foundation (grant AGS-1640452 and AGS-2146708), which made it possible for me to advance scientific understanding of hailstorms through unique analyses presented in this dissertation. This research contributes toward improving weather forecasts for hailstorms, helping build resilient communities worldwide.

To Angela Rowe's lab: thank you for fostering an environment of growth since its inception at UW-Madison. Special thanks go to Ian Cornejo for his assistance with the programming aspects of my thesis and for being both a collaborator and friend throughout this journey.

To the AOS Department staff, Kristi Levenson, Carolyn Lipke, Kaitlyn Heinlein, and Dee VanRuyven, your incredible support made my time at UW-Madison truly memorable.

Finally, I want to express endless gratitude to my loving husband, Daniel Camilo Bernal Ayala. Despite being separated by continents and an ocean during much of this journey, his unwavering support has been a source of strength and inspiration every step of the way. Sharing life with such an extraordinary human being is one of my greatest honors.

To you, the reader, whether you are young or experienced in your career, whether you come from this scientific field or another entirely, I sincerely hope you enjoy reading this dissertation as much as I enjoyed creating it. This thesis represents more than scientific advancements; it reflects a lifelong curiosity sparked in childhood, a fascination with the Earth and the sky that evolved into a passion for understanding their interactions. What began as a dream has now become reality, embodied in the work presented here.

Table of Contents

ABSTRACT	I
ACKNOWLEDGMENTS	III
TABLE OF CONTENTS	V
TABLE OF FIGURES	VII
LIST OF TABLES	XIII
CHAPTER 1	1
CHAPTER 2	20
2.1 PREFACE	21
2.1.1 PRINCIPLES OF SCANNING MICROSCOPY TECHNIQUES AS APPLIED TO PARTICLE ANALYSIS	24
2.1.1.1 Confocal laser scanning microscope (CLSM)	24
2.1.1.2 Scanning electron microscopy (SEM) and energy-dispersive X-ray spectroscopy (EDS)	25
2.1.1.3 Protected particle deposit in hailstone samples for CLSM and SEM–EDS analysis	26
2.2 MATERIALS AND METHODS	28
2.2.1 HAILSTONE COLLECTION	28
2.2.2 HAILSTONE PREPARATION WITH AN ADAPTED SUBLIMATION METHOD	29
2.1.3 MICROSCOPY ANALYSIS	32
2.3.3.1 CLSM analysis	32
2.3.3.2 SEM–EDS analysis	33
2.3 APPLICATION OF THE MICROSCOPY TECHNIQUE TO HAILSTONES	36
2.4 LIMITATIONS AND RECOMMENDATIONS	40
2.5 CONCLUSIONS	43
2.6 APPENDIX A: CLEANING PROTOCOL FOR QUASI-CLEAN SUBZERO FACILITIES	45
2.7 APPENDIX B: OPTIMUM THICKNESS OF THE POROUS PLASTIC COATING LAYER	46
2.8 FIGURES	49
CHAPTER 3	63
3.1 PREFACE	64
3.2 DATA AND METHODS	69
3.2.1 HAILSTONE COLLECTION AND PREPARATION	69
3.2.2 MICROSCOPY ANALYSIS	71
3.2.3 ELEMENTAL CHARACTERIZATION	73
3.2.4 AIR MASS TRAJECTORIES	76
3.3 RESULTS	78
3.3.1 8 FEBRUARY 2018	78

3.3.1.1 Particle Size and Elemental Composition of Individual Particles	78
3.3.1.2: Possible Source Regions	81
3.3.2 13-14 DECEMBER 2018	83
3.3.2.1 Particle Size and Elemental Composition of Individual Particles	84
3.3.2.2: Possible Source Regions	86
3.4 DISCUSSION:	87
3.5 CONCLUSION	92
3.6 FIGURES	96
CHAPTER 4	106
4.1 PREFACE	107
4.2 DATA AND METHODS	113
4.2.1 SMASH DATASET	113
4.2.2 ENVIRONMENTAL PARAMETERS	114
4.2.3 ANALYSIS APPROACH	115
4.3 RESULTS	119
4.3.1 SPATIAL DISTRIBUTION AND TEMPORAL EVOLUTION	119
4.3.2 OT CHARACTERISTICS AND ENVIRONMENTAL PARAMETERS	121
4.3.3 PARAMETER RELATIONSHIPS AND STORM ORGANIZATION	124
4.4 DISCUSSION AND CONCLUSIONS	130
4.5 FIGURES	137
CHAPTER 5	150
CONCLUSIONS AND FUTURE WORK	150
5.1 BROADER MOTIVATION AND GOALS	151
5.2 RESEARCH QUESTIONS AND KEY RESULTS	152
5.3 SYNTHESIS OF PHYSICAL INSIGHTS	154
5.4 METHODOLOGICAL ADVANCES AND LIMITATIONS	160
5.5 FUTURE DIRECTIONS	165
6 REFERENCES	167

Table of Figures

Figure 2.1: A particle trapped in a hailstone as observed by CLSM and SEM for the 1 % Formvar coating.....	49
Figure 2.2: An example of a thin cross section of a hailstone sectioned through its equatorial plane. It is affixed to several thin glass sections arranged in a mosaic pattern on a thin glass slide with dimensions of 25×75 mm	50
Figure 2.3: The figure shows the preparation stages of a hailstone. (a) The hailstone is attached to a glass section and then to a metal section plate with ultrapure liquid water. (b) The hailstone is cut in the equatorial symmetric plane to provide a view of the hailstone's embryo.....	51
Figure 2.4: Images showing before (a) and after (b) a hailstone is evenly polished to the desired thickness with a microtome to obtain a top view of the embryo. (c) The hailstone is then left to sublimate in a humidity-controlled container with silica gel.....	52
Figure 2.5: Example CLSM imagery from the coated, sublimated hailstone shows (a) a 2-D cross section along an axis in the equatorial plane at $108 \times$ magnification and (b) a subsector scanned at higher magnification for creating (c) visible and (d) laser images for individual particles. (e) 3-D particle surface topography from the visible imagery is analyzed with ProfilmOnline software.	53
Figure 2.6: Panel (a) displays the particle prior to undergoing EDS analysis, while panel (b) illustrates the particle's post-EDS analysis, revealing subtle breakage and disintegration concentrated at the center of the particle where the SEM laser was centered.	54
Figure 2.7: (a) A SEM backscattered-electron image for an individual particle categorized as carbon-based with (b) the corresponding EDS elemental composition for that particle. The first peak, closest to 0 keV, is caused by noise from the EDS detector and can be ignored when analyzing the elemental composition of a particle, as it does not represent any actual element. The second spectral peak corresponds to gold (2.12 keV) and was excluded from the analysis since it was used for coating the sample.	55
Figure 2.8: Activation volume producing Fe X-rays within the soda–lime glass for 8 kV (a) and 15 kV (b) accelerating voltage from the Monte Carlo simulations. Lines indicate the pathways of individual electrons backscattered from within the sample (blue) and from the sample surface (red) as a function of the particle size (in nm).....	56
Figure 2.9: An example of an analyzed hailstone (V-7) for which the areas highlighted by red rectangles indicate where particles were randomly selected to measure the particle size distribution, using CLSM and elemental composition via SEM–EDS. The orange circle marks the location of the embryo.	57

Figure 2.10: Particle size distributions for hailstone samples collected during the event on 8 February 2018. Panels (a) and (b) display particle sizes for two different cross sections from sample V-7, while panels (c) and (d) show particle sizes for samples V-16 and V-17, respectively. 58

Figure 2.11: Examples from each of the primary particle categories are presented, along with their ProfilmOnline topographical output obtained through a confocal laser scanning microscope (CLSM; top), and accompanied by their corresponding scanning electron microscopy (SEM; bottom) image. 58

Figure 2.12: EDS-based elemental composition distribution of particles for (a) V-7V and (b) V-7H cross sections, as seen in Fig. 9..... 59

Figure 2.13: EDS-based elemental composition distribution of particles found in the embryo for sample V-7 for (a) V-7V and (b) V-7H..... 59

Figure 2.14: Mathematical operations on the spectrum using DTSaII were done to analyze the EDS spectrum data and differentiate a particle's spectrum from the glass substrate. Panel (a) depicts the spectrum of the particle presented in Fig. 7b. Panel (b) illustrates the spectrum of the glass. Panel (c) demonstrates the outcome of the subtraction, revealing the presence of elements C, Na, Cl, and K in the particle. The first peak, closest to 0 keV, is caused by noise from the EDS detector and can be ignored when analyzing the elemental composition of a particle, as it does not represent any actual element. The second spectral peak corresponds to gold (2.12 keV) and was excluded from the analysis since it was used for coating the sample. 60

Figure 2.15: Panels (a), (c), and (e) display a single-point spectral analysis of a C-based particle with Formvar (a), a clear area with Formvar (c), and a clear area without Formvar (e). Each panel in the figure to the right (b, d, f) is the corresponding panel providing a closer view of the C peak. Due to Formvar's thickness and the results in this figure, the Formvar layer's impact on the C peak is considered negligible. The first peak, closest to 0 keV, is caused by noise from the EDS detector and can be ignored when analyzing the elemental composition of a particle, as it does not represent any actual element. The second spectral peak corresponds to gold (2.12 keV) and was excluded from the analysis since it was used for coating the sample. 61

Figure 2.16: A snapshot from the Olympus LEXT Analysis software of a sublimated ice sample with a Formvar coating. Panel (a) shows the 2-D CLSM laser imagery, with the red line indicating the transect through an area with and without the coating. Panel (b) shows the height (y axis in μm) across that transect (x axis in μm) for calculating the Formvar thickness (as seen along the blue segment), plotting the height used for Formvar's thickness calculation shown with the blue dot. 62

Figure 3.1: Map of northern Argentina covering an area shown in the black box in the lower right panel, including the Córdoba study area and nearby provinces. Within the dashed box covering northern Córdoba province is an inset (top left) highlighting Córdoba City to the east of the Sierras de Córdoba (SDC) and points of interest for this analysis: the site of the CACTI experiment observations in Villa Yacanto (black star), the hail collection locations: Villa Carlos Paz, Villa del Dique (lime green and blue stars, respectively), and the initiation point for air mass back trajectory run for 8 February and 13-14 December (red and blue star, respectively). Color fill represents the

C3S Land Cover map available through the C3S Climate Data Store (CDS): 1-cropland rainfed, 2-cropland rainfed, 3-cropland rainfed tree or shrub cover, 4-cropland irrigated, 5-mosaic cropland, 6-mosaic natural vegetation, 6-tree broadleaved evergreen closed to open, 7-tree broadleaved deciduous closed to open, 8-tree broadleaved deciduous closed, 9-tree broadleaved deciduous open, 10-tree needleleaved evergreen closed to open, 11-tree needleleaved evergreen closed, 12-tree needleleaved evergreen open, 13-tree needleleaved deciduous closed to open, 14-tree needleleaved deciduous closed, 15-tree needleleaved deciduous open, 16-tree mixed, 17-mosaic tree and shrub, 18-mosaic herbaceous, 19-shrubland, 20-shrubland evergreen, 21-shrubland deciduous, 22-grassland, 23-lichens and mosses, 24-sparse vegetation, 25-sparse tree, 26-sparse shrub, 27-sparse herbaceous, 28-tree cover flooded fresh or brackish water, 29-tree cover flooded saline water, 30-shrub or herbaceous cover flooded, 31-urban, 32-bare areas, 33-bare areas consolidated, 34-bare areas unconsolidated, 35-water, 36-snow and ice. 97

Figure 3.2: 2-D cross-section along an axis in the equatorial plane at 108x magnification for sample V-7 collected on 8 February 2018. Sectors (S) 4 and 5 indicate the embryo, while S1-S3, S6-S8 represent the outer layers. 98

Figure 3.3: As in Figure 2, but for NG-1 collected on 13-14 December 2018. Sectors are grouped by layers relative to the embryo (layers 1-5) and outer layer (6-10). 99

Figure 3.4: Examples of particles analyzed using three complementary techniques: Confocal Laser Scanning Microscopy (CLSM, top row), Scanning Electron Microscopy (SEM, middle row), and Energy-Dispersive X-ray Spectroscopy (EDS, bottom row). Left column shows an agglomerated mineral/organic particle. Middle column displays a Fe-rich organic particle. Right column shows a salt particle from V-7H Sector 1, with prominent Na and Cl peaks characteristic of halite. The CLSM images provide optical characteristics and context within the hailstone, while SEM reveals detailed surface morphology and EDS spectra confirm elemental composition. Scale bars in CLSM images represent 20 μm 100

Figure 3.5: Particle size distribution in μm through the V-7 cross-section is shown in Figure 2, where the particle size distribution in the hailstone embryo region is represented by blue pastel bars, and the particle size distribution in the outer layers of the hailstone is shown by orange pastel bars. 101

Figure 3.6: Elemental composition distributions for particles selected within the 2-D cross sections for a) V-7 and b) NG-1. 102

Figure 3.7: Elemental composition distribution for particles identified in the V-7 cross-section shown in Figure 2. 102

Figure 3.8: HYSPLIT analysis for 8 February 2018. (a) (top) shows 24-hour HYSPLIT back trajectories color-coded by height (in meters), with Córdoba City marked by a white star. The bottom of (a) displays terrain analysis in meters above sea level for the same time periods as the back trajectories. (b) shows residence time coefficients calculated for 5-day back trajectories overlaid on the C3S Land Cover map with Córdoba City marked by a white star. The land cover colors correspond to a subset of categories shown in Figure 1, specifically: 1/2/3-Cropland rainfed, 4-Cropland irrigated, 5-Mosaic cropland, 6-Mosaic natural vegetation, 7-Evergreen

broadleaved, 8/9/10-Deciduous broadleaved, 11-Evergreen needleleaved, 12-Mixed trees, 13-Mosaic tree/shrub, 14-Mosaic herbaceous, 15/16-Shrubland, 17-Grassland, 18-Sparse vegetation, 19-Sparse herbaceous, 20-Fresh water flooded tree cover, 21- Saline water flooded tree cover, 22-Flooded shrub/herbaceous cover, 23-Urban, 24-Bare areas, 25-Water, 26-Snow and ice. (c) displays the predominant land uses within the residence time coefficient pixels observed in b). Similar land uses were grouped into the following categories: Urban (23), Water (25,26), Cropland(1,2,3,4,5), Shrubland(15,16,17), Mixed Vegetation (6,7,8,9,10,11,12,13,14,18,19). Flooded Vegetation (20,21,22) and bare areas (24) were not included. 103

Figure 3.9: Particle size distribution in μm through the NG-1 cross-section is shown in Figure 3, where the particle size distribution in the hailstone embryo region is represented by blue pastel bars, and the particle size distribution in the outer layers of the hailstone is shown by orange pastel bars. 104

Figure 3.10: Elemental composition distribution for particles identified in the NG-1 cross-section shown in Figure 3. 104

Figure 3.11: HYSPLIT analysis for 13-14 December 2018. (a) (top) shows 24-hour HYSPLIT back trajectories color-coded by height (in meters), with Córdoba City marked by a white star. The bottom of (a) displays terrain analysis in meters above sea level for the same time periods as the back trajectories. (b) shows residence time coefficients calculated for 5-day back trajectories overlaid on the C3S Land Cover map with Córdoba City marked by a white star. The land cover colors correspond to a subset of categories shown in Figure 1, specifically: 1/2/3-Cropland rainfed, 4-Cropland irrigated, 5-Mosaic cropland, 6-Mosaic natural vegetation, 7-Evergreen broadleaved, 8/9/10-Deciduous broadleaved, 11-Evergreen needleleaved, 12-Mixed trees, 13-Mosaic tree/shrub, 14-Mosaic herbaceous, 15/16-Shrubland, 17-Grassland, 18-Sparse vegetation, 19-Sparse herbaceous, 20-Fresh water flooded tree cover, 21- Saline water flooded tree cover, 22-Flooded shrub/herbaceous cover, 23-Urban, 24-Bare areas, 25-Water, 26-Snow and ice. (c) displays the predominant land uses within the residence time coefficient pixels observed in b). Similar land uses were grouped into the following categories: Urban (23), Water (25,26), Cropland(1,2,3,4,5), Shrubland(15,16,17), Mixed Vegetation (6,7,8,9,10,11,12,13,14,18,19). Flooded Vegetation (20,21,22) and bare areas (24) were not included. 105

Figure 4.1: Example of the spatial matching process between SMASH OT detections (probability in filled colors) and GPM-DPR FlagHail data (red dots) for February 14, 2020. The blue dashed circle illustrates the 5-km radius search area around the OT used for matching with FlagHail detections. This OT has a deep convection (dc) flag value of 1.0, indicating it meets the deep convection criteria. 138

Figure 4.2: Demonstration of the GPM-DPR FlagHail and GOES data matching process for a case study on February 14, 2020, around 0730 UTC. Top row shows GOES-16 data: (left) cloud height in m, (center) Channel 11 brightness temperature in K (BT), and (right) parallax-corrected Channel 11 brightness temperature (PC-BT). Bottom row shows: (left) original GPM FlagHail detections, (center) swath-edge displacement corrected FlagHail detections, and (right) the combined visualization of parallax-corrected GOES imagery with corrected FlagHail detections. Yellow regions in the BT images indicate areas meeting OT detection criteria, while pink shading shows the anvil cloud extent. 139

Figure 4.3: Spatial distribution of SMASH OT detections from October 2014 through February 2022. (a) Unfiltered OT counts (total: 2481) showing all detected OTs. (b) Filtered OT counts (total: 1298) showing only OTs with probability values greater than 0.5 and deep convection flag equal to 1. Both panels use a $1^\circ \times 1^\circ$ grid, with color intensity indicating the number of OTs per grid cell. The circled C marks the location of Córdoba city. 140

Figure 4.4: Comparison of (a) hail-matched SMASH OT detections (total: 189) and (b) GPM-DPR FlagHail detections (total: 21092) across Argentina from October 2014 through February 2022. Both panels use a $1^\circ \times 1^\circ$ grid, with the circled C marking Córdoba city. Panel (a) shows OTs that were successfully matched with FlagHail detections using spatial and temporal criteria, with counts per grid cell (in red shading). Panel (b) displays the total FlagHail detections, with counts per grid cell in blue shading. 140

Figure 4.5: As in Figure 4.4 but for 0-6 UTC, 21-03 local time. 141

Figure 4.6: As in Figure 4.4 but for 6-12 UTC, 03-09 local time. 141

Figure 4.7: As in Figure 4.4 but for 12-18 UTC, 09-15 local time. 142

Figure 4.8: As in Figure 4.4 but for 18-23 UTC, 15-20 local time. 142

Figure 4.9: Comparison of OT characteristics between filtered ($n=1298$) and hail-matched ($n=189$) cases from October 2014 through February 2022. Left panel shows OT area distributions (km^2). Right panel shows IR-tropopause temperature differences (K). Both panels include only OTs with probability values greater than 0.5. Box plots show median (green line), interquartile range (blue box), whiskers extending to 1.5 times the interquartile range, and outliers (black circles). 143

Figure 4.10: Comparison of environmental parameters between filtered ($n=1298$) and hail-matched ($n=189$) OT cases from October 2014 through February 2022. Parameters shown are: (a) MUCAPE (J/kg), (b) precipitable water (mm), (c) 0-3 km wind shear (m/s), (d) 0-6 km wind shear (m/s), (e) MUCIN (J/kg), (f) cloud top height (km), (g) wet bulb zero height (km), and (h) 500-700 hPa lapse rate ($^\circ\text{C}/\text{km}$). Box plots show median (green line), interquartile range (blue box), whiskers extending to 1.5 times the interquartile range, and outliers (black circles). Note that filtered cases include both hail-matched and non-matched OTs. 143

Figure 4.11: Diurnal variation of environmental parameters for hail-matched OTs across four time periods (0-6, 6-12, 12-18, and 18-23 UTC, where local time is UTC-3). Parameters and box plot lines are as in Figure 10. Sample sizes for each time period are: 0-6 UTC (52), 6-12 UTC (39), 12-18 UTC (20), and 18-23 UTC (78). 144

Figure 4.12: Scatterplots of environmental parameters as in Figure 4.10 as a function of OT area (km^2) for hail-matched OTs ($n=189$). Each panel shows individual cases (blue dots), linear regression fit (red line), and correlation coefficient (r). 144

Figure 4.13: As in Figure 4.12 but for IR-Tropopause Temperature difference (K). 145

Figure 4.14: Multi-parameter analysis of relationships between OT characteristics and environmental conditions for hail-matched cases ($n=189$). Each panel shows OT area (x-axis, km^2)

versus IR-tropopause temperature difference (y-axis, K), with points colored by: (a) MUCAPE (J/kg), (b) precipitable water (mm), (c) 0-3 km wind shear (m/s), (d) 0-6 km wind shear (m/s), (e) MUCIN (J/kg), (f) cloud top height (km), (g) wet bulb zero height (km), and (h) 500-700 hPa lapse rate ($^{\circ}\text{C}/\text{km}$). Each panel shows individual cases (color dots), linear regression fit (red line), and correlation coefficient (r). 145

Figure 4.15: Correlations between environmental parameters for hail-matched cases ($n=189$), shown twice with different color coding. Top row (a-d) shows points colored by OT area (km^2), while bottom row (e-h) shows points colored by IR-tropopause temperature difference (K). Relationships shown are: (a,e) MUCAPE vs 0-6 km wind shear, (b,f) wet bulb zero height vs 500-700 hPa lapse rate, (c,g) MUCAPE vs precipitable water, and (d,h) wet bulb zero height vs precipitable water. Each panel shows individual cases (color dots), linear regression fit (red line), and correlation coefficient (r). 146

Figure 4.16: Spatial distribution of overshooting tops (OTs) classified as single-cell storms (blue dots, $n=181$) and multicellular events (red dots, $n=4$) across Argentina during 2014-2022. Cordoba city is marked with (C). Multicellular events are observed in four distinct locations: the central region (26°S), along the Uruguay border (34°S), and in southern Argentina (38°S). 147

Figure 4.17: GOES-16 ABI Band 11 ($8.4\ \mu\text{m}$) brightness temperature (K) observations showing OTs classified as multicellular as defined in the text. Images are from: a) November 10, 2018 at 21:45 UTC, b) January 16, 2021 at 19:20 UTC, c) February 13, 2021 at 20:20 UTC, and d) February 26, 2021 at 17:00 UTC. White circles highlight the location of the OTs of interest... 148

Figure 4.18: Comparison of environmental parameters between single-cell ($n=181$) and multicellular ($n=8$) events. Box plots show: (a) Most Unstable CAPE (J/kg), (b) Precipitable Water (mm), (c) 0-1 km Wind Shear (m/s), (d) 0-6 km Wind Shear (m/s), (e) Most Unstable CIN (J/kg), (f) Cloud Top Height (km), (g) Wet Bulb 0°C Height (km), and (h) 500-700 hPa Lapse Rate ($^{\circ}\text{C}/\text{km}$). 149

List of Tables

Table 1: Particle size ranges for each elemental category identified in hailstone samples V-7 and NG-1.	49
Table 2: Particle size ranges for each elemental category identified in hailstone samples V-7 and NG-1.	96
Table 3: Monthly and annual OT counts for October (10) through February (02) from 2014-2022, showing three categories: unfiltered / filtered / hail-matched detections. Filtered counts include only OTs with probabilities greater than 0.5 and deep convection flag equal to 1, while hail-matched counts represent OTs successfully matched with GPM-DPR FlagHail detections. Total annual counts are shown in the bottom row.	137

Chapter 1

Introduction

Falling hailstones are among the most destructive natural phenomena in convectively active regions of the world, with impacts ranging from extensive property damage to agricultural devastation. In the U.S. alone, hail damage has exceeded 1 billion dollars since 1949 (Changnon 2008; Sander et al. 2013; Allen et al. 2017; Kumjian et al. 2019), making it the costliest natural hazard in terms of insured losses to homes, businesses, automobiles, aircraft, and agriculture (Dennis and Kumjian 2017). Insurance claims from hail events have shown exponential growth in recent decades, with single events capable of causing catastrophic losses. For example, a 2019 hailstorm in Munich, Germany, resulted in insurance claims exceeding €900 million, demonstrating how urban expansion into hail-prone regions has amplified the potential for significant economic losses (Munich Re 2020).

The vulnerability of different regions to hail damage varies significantly based on local infrastructure, agricultural practices, and economic resources. In the U.S., building codes and construction practices have evolved to better withstand hail impacts, yet annual losses continue to grow as urban areas expand into hail-prone regions (International Code Council 2008; Kuronen 2022). European studies have revealed a complex pattern of vulnerability, where historical architecture in many cities remains particularly susceptible to hail damage, while modern building practices increasingly incorporate hail-resistant materials (Munich Re 2018). In developing nations, where insurance coverage is often limited, hail damage to crops can have devastating effects on local economies and food security, creating long-lasting socioeconomic impacts that extend far beyond the immediate storm damage.

The impact extends beyond economic losses to include significant ecological consequences. In India, hail can decimate crops and fauna, as demonstrated by the 2014 Maharashtra storms that affected thirty-five species of birds and nine species of mammals (Narwade et al. 2014; Bal et al. 2014). These biological impacts highlight how hail events can disrupt entire ecosystems, affecting both immediate agricultural productivity and long-term biodiversity. Through a compilation of hail reports across Europe, Pucik et al. (2019) found that damage patterns correlate strongly with hailstone size, with crop and tree damage most frequently associated with hail sizes ranging from 2 to 3 cm, while damage to infrastructure typically occurred with larger hail between 4 to 6 cm.

The challenge of assessing and predicting hail impacts becomes particularly complex in regions with limited observational networks. Europe faces unique challenges in this regard due to the lack of temporal and spatial records of large hail (larger than 5 cm), as European weather stations typically do not record hail sizes (Punge and Kunz 2017; Pucik et al. 2019). This limitation in documentation significantly affects our ability to understand and predict hail threats in these regions. In South America, particularly the Córdoba Province in Argentina, some of the most intense storms in the world occur (Zipser et al. 2006), yet traditional ground-based monitoring networks remain sparse. The combination of intense storm systems and limited observational capabilities makes this region particularly vulnerable to hail impacts, while simultaneously offering unique opportunities for advancing our understanding of severe storm dynamics.

These varied impacts and challenges in documenting hail occurrence across different regions underscore the critical need to advance our understanding of hail formation, development, and the environmental conditions that anticipate hail threats. To address these challenges effectively, we

must first understand the fundamental processes governing hail formation and growth within storms, as well as the environmental conditions that support their development. This understanding becomes increasingly crucial as changing climate conditions may alter the frequency and intensity of severe storms worldwide, potentially affecting regions already vulnerable to hail impacts (Allen et al. 2020; Raupach et al. 2021a; Gensini et al. 2024).

The formation and growth of hailstones represent a complex interplay between microphysical processes and storm dynamics. Hail, defined as any regular or irregular piece of ice falling from a thunderstorm exceeding a maximum diameter of 5 mm (AMS Glossary), develops through a series of specific processes that require precise environmental conditions. These pellets of ice form inside convective storms (Rogers and Yau 1989), typically three to four miles above the surface during warm seasons, where air temperatures range from -10° to -25° C (Browning and Foote 1976; Nelson 1983; Miller et al. 1988; Knight and Knight 2001; Pilorz et al. 2022). Most hail growth occurs at these temperatures because this range is optimal for the presence of supercooled water droplets, which remain liquid at sub-freezing temperatures, although they can persist in liquid form until reaching the homogeneous freezing temperature of approximately -38° C.

Three fundamental ingredients are necessary for storms to produce hail. First, a small (1 cm or less) particle must be the nucleus for further growth. These particles, known as "embryos," can form through multiple pathways: either as frozen drops or as graupel/heavily rimed snow. Ice nucleating particles (INPs) facilitate the freezing process, which are crucial for initiating ice formation at temperatures warmer than homogeneous freezing (-38° C). These INPs include mineral dust from surface sediments, biological material (e.g., pollen, bacteria, fungal spores), and

volcanic ash, facilitating ice formation through heterogeneous freezing processes (Lamb and Verlinde 2011; Vali et al. 2015). The historical emphasis on ice-nucleating particles $\leq 10 \mu\text{m}$ primarily reflects technical limitations rather than theoretical constraints. Early detection methods, such as continuous flow diffusion chambers (CFDCs), employed size-selective impactors (e.g., removing particles $>2.4 \mu\text{m}$) to avoid optical misclassification of ice crystals and aerosols, systematically excluding super-micron particles from analysis (Cziczo et al. 2009; DeMott et al. 2010). This instrumental bias was compounded by practical modeling considerations: sub- $10 \mu\text{m}$ particles dominated atmospheric datasets due to their higher abundance and slower sedimentation rates, leading to parameterizations skewed toward smaller sizes (DeMott et al. 2016).

While classical nucleation theory (CNT) linked INP activity to surface area, a property more prevalent in smaller particles, this framework overlooked critical factors such as surface defects and compositional heterogeneity (Chen et al. 2021). Recent size-resolved studies challenge these historical assumptions, revealing that particles $>10 \mu\text{m}$ exhibit 2-5 times higher ice-nucleating efficiency per unit mass than smaller counterparts at warmer temperatures (-15°C). This enhanced activity often relates to biological materials adhering to their surfaces (Chen et al. 2021). Modern techniques using microfluidic arrays (devices used to manipulate and analyze very small volumes of fluids, within networks of channels and chambers) now enable the investigation of super micron INPs in processes like hail embryo formation, revealing their previously underestimated role (Tarn et al. 2018). The persistence of the $10 \mu\text{m}$ threshold in many studies reflects a legacy of instrumental constraints and sampling biases rather than a theoretical ceiling on INP efficacy. This understanding highlights the importance of methods capable of analyzing larger particles,

particularly in contexts of hail formation where their role may be more significant than previously recognized.

Second, an abundance of supercooled liquid water must be supplied by the convective storm's updraft through activation of cloud condensation nuclei (CCN), and subsequent condensational growth into droplets. Hail growth begins when the embryo collects supercooled water through riming, which can proceed through either dry growth (where droplets freeze immediately upon contact) or wet growth (where water spreads before freezing, creating clear ice layers). The rate of freezing during riming, determined by the amount of supercooled liquid water present, influences the hailstone's opacity and layered structure. Third, sufficient residence time is essential for creating large hailstones, determined by the path or trajectory a hailstone takes through both a storm's updraft and downdraft regions.

The formation of hailstones involves multiple pathways rather than a single, linear process of ice nucleation followed by riming. While traditional views often simplified hail formation to a single INP initiating the embryo, research has shown that multiple mechanisms can contribute to hailstone development (Pruppacher and Klett 1980; Murray et al. 2012). The embryonic stage involves interactions between various particles and water droplets in the dynamic thunderstorm environment, particularly within regions of strong updrafts where abundant supercooled water droplets exist at temperatures typically between 0°C and -15°C (Ludlam 1980). These conditions are common in various types of severe convective storms.

Initial ice particles can form through several mechanisms. Heterogeneous ice nucleation occurs when supercooled droplets contact INPs such as mineral dust, biological particles, or other aerosols, facilitating freezing at warmer subzero temperatures (Murray et al. 2012). Homogeneous freezing occurs at temperatures below approximately -38°C , where water droplets freeze spontaneously without an INP (Pruppacher and Klett 1980). Additionally, secondary ice production mechanisms like rime splintering can generate ice particles without requiring additional INPs (Field et al. 2017). Hailstone formation often involves multiple ice nucleation events and growth processes, rather than a single INP initiating the embryo. Initial ice particles can form through direct nucleation on various INPs, but hailstones also grow by aggregating with other ice particles, some of which may have nucleated separately.

Passive collection processes play a role in hail growth through aggregation of ice particles, accretion of supercooled water droplets (riming), and collection of rain droplets below the melting layer (Hoose and Möhler 2012). The efficiency of these processes depends on factors such as particle sizes, velocities, and ambient conditions (Pruppacher and Klett, 1997). Riming, where supercooled water droplets collide with and freeze onto existing ice particles, can significantly increase the mass of a developing hailstone beyond what would be possible through deposition of water vapor alone (Pruppacher and Klett, 1997).

Research examining hailstone embryos has revealed the presence of both biological, organic, and soil-derived ice nuclei, suggesting that multiple nucleation sources can contribute to a single hailstone's formation (Christner et al. 2005; Šantl-Temkiv et al. 2013; Michaud et al. 2014; Testa et al. 2021; Bernal Ayala et al. 2024a). This means that within a single hailstone, multiple distinct

INPs may have individually nucleated ice, as well as ice particles formed through secondary production mechanisms. The combination of these various ice particles through aggregation and riming processes contributes to hailstones' complex internal structure (Knight and Knight 2001).

Particles with complex surfaces are particularly effective at promoting ice nucleation due to their enhanced surface area and active sites for freezing (Rosinski and Kerrigan 1969). Atmospheric aging processes can modify particle properties and also enhance their ice nucleating capabilities. Chemical coating and surface modification alter the physical and chemical properties of aerosols, increasing their "stickiness" and hygroscopicity. For example, soot particles exposed to sulfuric acid vapor undergo morphological changes that enhance their ability to interact with other atmospheric constituents (Mokkapati 2009). Turbulence in convective systems enhances collision frequencies, with larger particles exhibiting higher agglomeration efficiency as their inertia allows them to overcome turbulent forces and maintain contact after collisions (Wang et al. 2024). Additionally, gravitational settling promotes agglomeration by causing larger particles to settle faster than smaller ones, increasing the likelihood of collisions between different-sized particles. These modifications can affect both the initial nucleation process and subsequent growth through water uptake and agglomeration processes, whereby large, agglomerated particles form from the physical coagulation of colliding particles (e.g., Wang et al. 2024), water-mediated binding of particles upon contact (e.g., Michaud et al. 2014), or attractive forces between charged particles (Lin et al. 2014). The efficiency of precipitation development depends strongly on the characteristics of INPs and their subsequent growth through agglomeration processes. However, excessive concentrations of INPs can inhibit precipitation efficiency by distributing available water vapor among too many growing ice crystals (Wang et al. 2023), thus emphasizing the

complex interplay between active nucleation and passive collection mechanisms, combined with the storm's dynamics, that ultimately determines the characteristics of the resulting hailstones.

The effectiveness of these fundamental processes depends heavily on specific atmospheric conditions that can either support or inhibit hail development. Previous studies (e.g., Foote and Knight 1977; Knight and Knight 2001; Cintineo et al. 2020; Zhou et al. 2021) have identified the most relevant parameters for understanding convective environments and their propensity for producing hail. Most Unstable Convective Available Potential Energy (MUCAPE) has emerged as a fundamental parameter, since it measures the maximum potential energy available for convection, calculated using the most unstable parcel in the lowest 300 hPa (approximately 3 km) of the atmosphere. This parameter directly relates to the updraft strength required for the first and third fundamental ingredients of hail formation, suspending embryos and providing sufficient residence time. Stronger updrafts associated with higher MUCAPE can lift water droplets to greater heights, where temperatures are well below freezing, increasing the supply of supercooled water droplets essential for hail growth. This relationship helps explain why supercells, with their characteristically strong, persistent rotating updrafts, are particularly efficient at producing large hail (Browning and Foote 1976; Nelson 1983; Dennis and Kumjian 2017). Higher MUCAPE often correlates with lower freezing levels, leading to a deeper atmospheric layer where hail can grow between the Freezing Level Height (FLH) and the top of the area of positive buoyancy (i.e., the equilibrium level).

The vertical distribution of moisture plays a critical role in providing the second fundamental ingredient, abundant supercooled liquid water. The amount of supercooled liquid water is directly

linked to updraft strength, which is why CAPE in the -10°C to -25°C layer (typically between 700-500 hPa) is particularly important for hail formation. High moisture content near the surface fuels convection and enhances instability, while the distribution of moisture at mid-levels plays a more nuanced role. Dry air entrainment reduces parcel temperature and moisture content through mixing, which can initially reduce CAPE. However, this entrainment process can enhance convective instability through evaporative cooling when mixing with lower-level moist air. Additionally, moisture distribution in the upper levels of the atmosphere affects the formation of anvil clouds and the overall structure of deep convective systems, impacting the longevity and organization of convective complexes.

Vertical wind shear, measured over different layers of the atmosphere, proves crucial for organizing storms and maintaining their structure, directly influencing the residence time of growing hailstones. Low-level shear (0-3 km) is critical for storm organization and longevity, playing a significant role in developing rotating updrafts characterizing supercells capable of producing large hail. Deep layer wind shear (0-6 km) indicates the overall storm environment and its potential for organization. Strong deep-layer shear helps maintain storm structure by preventing the updraft from being undercut by the cold pool and contributes to the development of wide, rotating updrafts. A study has shown that while strong deep-layer shear generally favors large hail production by supporting supercell development and maintenance, strong low-level shear may actually inhibit hail growth in supercells by disrupting critical growth regions within the storm (Dennis and Kumjian 2017). Recent work by Nixon et al. (2023) further emphasizes the complex interplay between CAPE and shear, showing that strong low-level storm-relative winds can inhibit hail growth unless the CAPE below the hail growth zone is weak. Their findings suggest that the

depth of CAPE, particularly above the freezing level, may be more critical for hail growth than absolute CAPE values alone. This highlights the importance of considering multiple parameters simultaneously when evaluating environments conducive to hail formation, as neither CAPE nor shear in isolation can fully characterize hail potential.

The journey of a hailstone through the storm and its survival to the surface has traditionally been associated with the Freezing Level Height (FLH), which marks where the temperature reaches 0 degrees Celsius. However, research has shown that the Wet Bulb Zero Height (WBZ) provides a more accurate measure of where hail actually begins to melt (Shanklin 1989). While the FLH indicates the altitude where the environmental temperature reaches freezing, the WBZ accounts for both temperature and moisture content, making it more relevant for understanding hail survival. As hailstones fall through unsaturated air, evaporative cooling of meltwater on their surface keeps them cooler than the ambient temperature. This process means that melting typically begins at the WBZ height where the wet-bulb temperature is 0°C, rather than at the environmental freezing level, making WBZ a more reliable indicator for predicting hail survival to the surface.

These environmental parameters, MUCAPE, wind shear, and WBZ, combine with other key factors like moisture content and mid-level lapse rates to influence not only individual hailstone growth but also the type of storms that can produce significant hail. These parameters are often combined into composite indices like the Significant Hail Parameter (SHIP), which was developed using U.S. proximity soundings to predict significant hail potential. SHIP incorporates moisture (through parcel mixing ratio), instability (MUCAPE), mid-level lapse rates (700-500 mb), temperature (-500 mb), and deep-layer shear to assess hail potential. The mode of convection

(discrete versus multicellular) has been shown to directly affect the production of severe weather (Dial et al. 2010). In U.S., most hail reports are associated with supercellular convection (Smith et al. 2012). More specifically, Blair et al. (2017) suggest that supercell thunderstorms frequently produce the largest hail compared with other convective morphologies. However, research indicates that atmospheric conditions and storm modes in other regions may differ significantly from this U.S. centric understanding. Zhou et al. (2021) demonstrated that Argentina's hail environments typically feature lower deep-layer shear but comparable or higher MUCAPE values compared to U.S. environments. This is particularly evident in regions like Córdoba Province in Argentina, where significant hail can occur in various storm modes, including organized multicellular systems that frequently occur during nocturnal hours (Mulholland et al. 2018; Bruick et al. 2019).

The complexity of these interactions between environmental parameters and storm dynamics highlights both our current understanding and the significant gaps that remain in our knowledge (Kumjian et al. 2019b; Allen et al. 2020; Dennis and Kumjian 2017). While laboratory studies (e.g., Knight and Knight 1970; Levi and Aufdermaur 1970) field observations (Browning and Foote 1976), and numerical modeling (e.g., Kumjian et al. 2020) have revealed much about the basic processes of hail formation, many questions remain about how these processes vary across different regions and storm modes (Blair et al. 2017; Bruick et al. 2019). These limitations in our understanding become particularly evident when studying hail-producing storms in regions with varying environmental conditions (Mulholland et al. 2018; Zipser et al. 2006). In particular, significant challenges remain in documenting and predicting hail occurrence, particularly outside U.S. (Martius et al. 2018; Giordani et al. 2024). While studies have revealed relationships between

hail growth and environmental parameters, many of these relationships are inferred from observations in the U.S. and Europe (e.g., Allen et al. 2020). Furthermore, proxy soundings used in these studies are unable to represent the variations in microphysical processes that exist within different storm modes (e.g., Smith et al. 2012; II et al. 2019). These limitations have spurred the development of new observational techniques and campaigns to better understand hail-producing storms globally, including areas where ground-based remote sensing platforms are sparse.

Recent technological advances have opened new pathways for addressing these knowledge gaps. The Bang and Cecil (2019) database has become widely referenced for studying hail climatologies. Their approach utilizes a multifrequency passive microwave hail retrieval method, based on brightness temperature thresholds from various microwave channels, specifically 10, 19, 37, and 85 GHz, onboard weather satellites like the Tropical Rainfall Measuring Mission (TRMM) and the Global Precipitation Measurement (GPM). By pairing brightness temperature-derived precipitation features with surface hail reports in the U.S., they developed a hail retrieval algorithm that estimates hail probabilities using logistic curves fitted to the microwave data. Their results indicated the highest hail frequencies in regions such as northern Argentina, southern Brazil, and the central U.S. However, they identified biases in their dataset, particularly in northeastern Argentina, where the reported hail frequencies did not align with ground observations, suggesting an overestimation of hail events in this region (Bang and Cecil 2019). Galligani et al. (2024) further investigated this discrepancy by utilizing polarimetric weather radar data and hydrometeor identification algorithms, which indicated that the actual hail occurrences were more concentrated in the southwestern regions of Argentina, such as Mendoza and Córdoba.

More recent advances in satellite-based hail detection have emerged to potentially address these limitations. Le and Chandrasekar (2021) developed a new hail identification algorithm using the GPM satellite's Dual-frequency Precipitation Radar (DPR). Their algorithm utilizes a statistically based precipitation-type index (PTI) threshold derived from DPR radar parameters that identifies hail along each vertical profile. This approach outputs binary indicators of hail existence along the profile and has demonstrated promising results, particularly in providing a more accurate representation of hail-producing storms near the Sierras de Córdoba. The algorithm's success in this region is particularly significant given the previously identified challenges in satellite-based hail detection over Argentina.

While the GPM-DPR approach focuses on detection of hail through radar measurements, other satellite-based methods have explored the use of storm-top features as proxies for severe weather. The Satellite Mapping & Analysis of Severe Hailstorms (SMASH) dataset, developed by Bedka et al. (2010), employs geostationary satellite observations from the GOES series, particularly Overshooting Top (OT) detections, to identify where and when strong thunderstorms capable of producing severe hail most often occur. The SMASH dataset, available for South America and South Africa, has proven valuable in relating hail-producing storms to specific environmental conditions, as demonstrated by Punge et al. (2023) in their analysis of South African storms.

These satellite observations have been complemented by targeted field campaigns that provide crucial ground validation and detailed storm environment measurements. The 2018-19 Remote sensing of Electrification, Lightning, and Mesoscale/microscale Processes with Adaptive Ground Observations (RELAMPAGO; Nesbitt et al. 2021) campaign, along with the concurrent Cloud,

Aerosol, and Complex Terrain Interactions (CACTI; Varble et al. 2021) project, marked a significant advance in our observational capabilities in central Argentina. These campaigns provided detailed measurements of storm environments and hail occurrence, offering unique opportunities to study how different storm modes produce severe hail in this region. Additionally, citizen science initiatives like the "COSECHEROS" program in Argentina have attempted to bridge the gap between satellite observations and ground truth, providing crucial validation data for remote sensing algorithms (Arena and Crespo 2019, Cos 2022).

While satellite observations and field campaigns have advanced our understanding of storm-scale processes, detailed analysis of individual hailstones provides crucial information about microphysical processes that cannot be obtained through remote sensing alone. The analysis of collected hailstone samples has emerged as a crucial avenue for understanding formation processes at the microscopic scale, with each hailstone serving as a miniature chronicle of its growth history preserved within its crystalline structure. Laboratory studies have revealed that atmospheric particles play a fundamental role in hail formation by serving as CCN or INP. The efficiency of these particles in nucleating ice depends on various factors, including their size, surface topography, and composition, including any coating present on their surfaces (Holden et al. 2021; Gao et al. 2022).

Traditional analysis of hailstone composition required melting the samples, which removed crucial information about particle distribution and spatial relationships within the hailstone structure. Previous studies have investigated hailstone composition using various techniques to determine their chemical constituents. For example, Šantl-Temkiv et al. (2013) analyzed hailstones from a

thunderstorm in Slovenia, focusing on dissolved organic carbon and total dissolved nitrogen, while Li et al. (2018) examined constituents in melted hailstones from China. A significant contribution came from Michaud et al. (2014), who took an approach that constrained their analysis to the hailstone's embryo, focusing on multiple hail-producing storms in the Rocky Mountains of the U.S. Their study utilized stable isotope analysis to estimate in situ temperatures during freezing and examined particle elemental compositions collected from hailstone embryos through scanning electron microscopy. They found that their hailstone embryos contained biological ice nuclei that can freeze water at relatively warm subzero temperatures, suggesting that biological particles have the potential to serve as nucleation sites for hailstone formation. However, these approaches still relied on melting the hailstones, which obscured the spatial distribution of non-soluble particles within the sample.

Understanding the role of these particles in hail formation has been significantly advanced through modern microscopy techniques. Confocal Laser Scanning Microscopy (CLSM) provides high-resolution optical imaging using a diffraction-limited spot to produce a point source of light and reject out-of-focus light, allowing for imaging of deep tissues and 3D reconstructions of imaged samples. This technique offers several advantages over conventional widefield optical microscopy, including the ability to control depth of field, elimination or reduction of background signal away from the focal plane, and the capacity to collect serial optical sections from thick specimens (Mercer 2005; Turner et al. 2001). Complementing CLSM, Scanning Electron Microscopy (SEM) with Energy-Dispersive X-ray Spectroscopy (EDS) provides detailed information about particle surface morphology and elemental composition. These techniques, when combined, offer

unprecedented insights into the physical and chemical characteristics of particles involved in hail formation.

These advances in observational capabilities, from satellite-based detection to microscopic analysis, combined with our evolving understanding of environmental controls on hail formation, provide new opportunities to address fundamental questions about hail development across different regions and storm modes. Regional variations in particle sources that can serve as INP or CCN are particularly important in Argentina, where multiple sources exist: extensive agricultural regions, mountain ranges like the Sierras de Córdoba, salt lakes, and varied geological features (Steinke et al. 2016; Iturri et al. 2017; Borda et al. 2022). These diverse particle sources, combined with the distinct environmental conditions across Argentina's complex terrain, may influence both storm development and hail formation processes in ways that differ from other regions. This dissertation aims to improve our understanding of hail formation through analyses spanning from particle-scale characteristics to the environments in which hail storms form, with a focus on Central Argentina, a region that challenges our U.S. centric understanding of severe storms. This work addresses fundamental questions about hail formation while simultaneously developing new tools and frameworks for studying severe storms in traditionally under-observed regions.

The dissertation is structured in three complementary chapters, each addressing specific aspects of hail formation and development. Chapter 2 introduces an innovative microscopy analysis methodology to preserve in situ non-soluble particles within hailstones using a protective porous plastic coating, overcoming previous limitations related to melting the hailstone sample. This method combines two powerful techniques: trapping non-soluble particles beneath a plastic coat

using the adapted sublimation technique and analyzing the particles individually with both CLSM and SEM-EDS. This methodological advancement provides the capability to study hailstone composition and properties while maintaining the spatial distribution of particles within the hailstone structure (Bernal Ayala et al. 2024b).

Building on this methodological foundation, Chapter 3 applies these techniques to examine hailstones collected from two different storm modes in Central Argentina. This analysis provides the first detailed characterization of non-soluble particles in hailstones from this region, offering insights into which non-soluble particles were likely involved in the initial stages of ice nucleation and subsequent hail formation and growth. The study characterizes the distribution and size of non-soluble particles, identifies their elemental composition distribution, and examines how varying environmental conditions may influence particle source regions (Bernal Ayala et al. 2024a).

Chapter 4 scales up to examine these environmental conditions and storm-scale characteristics associated with hail production in Argentina through analysis of OTs and their environmental context. By uniquely combining the SMASH and GPM-DPR hail detection databases, this chapter investigates how OT characteristics relate to their environment, examining the range of environmental conditions associated with hail-producing storms, their diurnal variations, and the relationships between OT characteristics and specific environmental parameters. This analysis reveals important differences from U.S. storm environments and helps explain why significant hail can form in apparently less favorable conditions. Chapter 5 synthesizes the key findings from these

studies, discusses their broader implications, and provides suggestions for future research directions.

Chapter 2

Exploring non-soluble particles in hailstones through innovative confocal laser and scanning electron microscopy techniques

2.1 Preface

The analysis of hailstone samples has been a subject of increasing interest owing to its potential to provide valuable insights into microphysics and the development of hailstorms (Jeong et al. 2020; Soderholm and Kumjian 2023; Wang et al. 2023). Consider a hailstone a miniature chronicle of time that preserves a rich history of its formation and growth within its crystalline structure. Understanding hailstones' microphysics and developmental processes is crucial for improving weather forecasting, mitigation strategies, and climate change modeling (Cintineo et al. 2020; Malečić et al. 2022; Wu et al. 2022; Jiang et al. 2023). Atmospheric particles play a crucial role in hailstone microphysics. Particles may be ingested into convective-cloud updrafts, serving as cloud condensation nuclei (CCN) or ice-nucleating particles (INPs), which are necessary to form hydrometeors like cloud droplets and ice crystals that are essential for hail formation. Furthermore, hailstones can accumulate particles from the surrounding environment in the cloud during their growth, which could have sizes larger than those that serve as CCN and INPs and would provide information about the source environments involved in hail formation. Particle size and chemical composition are essential to quantify because they influence the nucleation efficiency and growth rate within hailstones. Characterizing these particles allows us to reconstruct their potential influence on hailstone properties, such as fall speed rates and growth regimes, furthering our understanding of hail formation and its complex interplay with atmospheric conditions.

Previous studies have investigated hailstone composition and properties using various techniques to determine their chemical constituents. For example, Šantl-Temkiv et al. (2013) analyzed hailstones from a thunderstorm in Slovenia, focusing on determining dissolved organic carbon and

total dissolved nitrogen in hailstones with a total nitrogen module. They also characterized dissolved organic matter through ultrahigh-resolution mass spectrometry that looked into the molecular complexity of hailstones. Overall, they noted a strong link to the local environment, particularly the hailstones' bacterial content, emphasizing a soil-driven origin for aerosol particles. More recently, Kozjek et al. (2023) expanded the analysis of hail in Slovenia by identifying fibrous and abiotic particles within melted hailstones.

Similarly, Li et al. (2018) examined constituents in melted hailstones. In their study, concentrations of 10 ions and 6 environmental pollutants were compared with the aerosol optical depth retrieved from the Moderate Resolution Imaging Spectroradiometer (MODIS) for 15 hailstorm events in China. They found that particulate matter with an aerodynamic diameter $<10 \mu\text{m}$ (PM10) was the most likely source of the water-soluble ions, although with considerable variability between hailstones. These PM10 particles are usually condensed below the cloud base and lifted higher through the updraft, highlighting a link to a terrestrial source. The concentration of water-soluble ions, metals, and metalloids in hailstones was investigated for the first time in South America by Beal et al. (2021), who analyzed hailstone samples from the triple border of Paraná, Brazil, and Argentina using ion chromatography and inductively coupled plasma mass spectrometry. That study's cleaning procedure efficiently removed potential chemical contaminants from hailstones by following procedures defined by Christner et al. (2005). They found that Ca^{2+} was the most abundant ion in their samples and interpreted it to be related to agricultural activities of non-local regions through long-distance transport. However, in their work, as in the aforementioned studies, these approaches rely on the melting of the hailstones, which obscures the spatial distribution of non-soluble particles within the hailstone.

Michaud et al. (2014) took an approach that constrained their analysis to the hailstone's embryo, focusing on three hail-producing storms in the Rocky Mountains of the USA. They utilized stable-isotope analysis to estimate in situ temperatures during freezing and examined particle elemental compositions collected from hailstone embryos through scanning electron microscopy. Similar to Beal et al. (2021), their study followed hailstone cleaning procedures defined by Christner et al. (2005), scraping the outermost layer with a sterile razor blade rinse with 95 % ethanol and then melting it so that it could be filtered onto a 13 mm diameter 0.2 μm polytetrafluorethylene membrane filter for elemental analysis. Their study focused on melting and filtering hailstone particles larger than 0.2 μm because of their interest in studying ice nucleation by immersion. They found that their hailstone embryos contained biological INPs that can freeze water at relatively warm subzero temperatures, suggesting that biological particles have the potential to serve as nucleation sites for hailstone formation.

In the literature discussed previously, hailstones were melted to study soluble compounds or particles, and in the case of Michaud et al. (2014), they used filters to separate the particles. A new method, derived from particle separation by adapted sublimation (Arena 2020), is described here to remove the need to melt the hailstone for microscopy analysis while retaining the particle's position within the hailstone. This new method, therefore, allows the analysis of non soluble particles within the hailstone sample, preserving all biological and non-biological particles without a maximum size restriction to provide a representative particle distribution in the hailstone. This approach allows microscopy techniques to be employed, as detailed below, enabling the characterization of non-soluble particles physically (particle size and surface topography) and chemically (inferred from elements within the individual particles). This information can be used

to improve our understanding of the distribution of particles within hailstones as a factor that influences the growth during the cloud droplets' initial stages of ice nucleation and subsequent hail growth.

2.1.1 Principles of scanning microscopy techniques as applied to particle analysis

2.1.1.1 Confocal laser scanning microscope (CLSM)

Confocal microscopy is a high-resolution optical imaging technique that uses a diffraction limited spot to produce a point source of light and reject out-of-focus light, allowing for imaging of deep tissues and 3-D reconstructions of imaged samples (Mercer 2005; Turner et al. 2001; Liu et al. 2011; Anderson 2014; Wang and Larina 2017; Elliott 2020; Claxton et al. 2006). A modern confocal microscope includes pinholes, objective lenses, low-noise detectors, fast scanning mirrors, filters for wavelength selection, and laser illumination (Elliott, 2020). Confocal microscopy has been extensively utilized in various disciplines, including supramolecular chemistry (e.g., Kubota et al. 2020), biology (e.g., Claxton et al., 2006), and materials science (e.g., Schnell et al. 2019), due to its high-resolution imaging capabilities. In particular, it is extensively used for studying the intricate structures and functions of biological specimens (O'Connor 1996; Kaye et al. 2015; Fu et al. 2021). This technique offers several advantages over conventional widefield optical microscopy, including the ability to control the depth of field, elimination of or reduction in the background signal away from the focal plane, and the capacity to collect serial optical sections from thick specimens (Mercer 2005; Turner et al. 2001; Liu et al. 2011; Anderson 2014; Wang and Larina 2017; Elliott 2020; Claxton et al. 2006). CLSM is, therefore, a powerful

tool for analyzing non-soluble particles due to its capacity to acquire three-dimensional images to determine the particle size distribution and particle surface information.

2.1.1.2 Scanning electron microscopy (SEM) and energy-dispersive X-ray spectroscopy (EDS)

Scanning electron microscopy (SEM) and energy-dispersive X-ray spectroscopy (EDS) are techniques often used together to analyze the surface of a sample. Both techniques and principles are based on the interaction of electrons with different types of matter. SEM works by scanning a focused beam of electrons onto a sample, inducing the emission of secondary electrons and backscattered electrons. These electrons can be detected and used to create a high-resolution image of a surface. SEM has extensive applications across various scientific disciplines, such as materials science (e.g., Zhang et al. 2020), geology and planetary science (e.g., Gu et al. 2020), and biology (e.g., Koga et al. 2021). Renowned for its capability to provide high-resolution imaging (e.g., Figure 2.1) at scales as fine as 50 nm (e.g., Vander Wood 2017), SEM has proven invaluable in diverse fields, including hailstone analysis (Michaud et al., 2014). Its imaging capabilities make SEM particularly well suited for investigating the morphology and texture of solid materials, allowing for a detailed analysis of surface features. EDS, on the other hand, is a technique that allows the analysis of the elemental composition of a sample. It works by detecting characteristic X-ray's emitted from the sample when bombarded with a beam of electrons. Each element has a unique set of peaks on its electromagnetic emission spectrum, which allows the identification of the chemical elements present in the sample (Goldstein et al. 2017; Raja and Barron 2016). Both techniques have been widely used in materials science, particle analysis (e.g., ice-nucleating, in-snow, and dust particles), and other fields to study the surface of samples and analyze their

chemical composition (e.g., Krueger et al. 2004; Bern et al. 2009; Ketterer 2010; Nam and Lee 2013; Farber 2019; Raval et al. 2019; Wagner et al. 2019; Brostrøm et al. 2020; Sanchez-Marroquin et al. 2020; Rausch et al. 2022).

2.1.1.3 Protected particle deposit in hailstone samples for CLSM and SEM–EDS analysis

CLSM and SEM–EDS microscopes were not designed for analyzing hailstone composition in subzero conditions. While it is common to find cryogenic stages on SEMs that facilitate subzero investigations and heating and/or cooling stages on optical scopes for handling frozen samples, issues especially arise when trying to preserve the location of particles within the stone. A specific relevant example of such limitations is that the vacuum in the SEM chamber used to remove air to prevent electron scattering and produce a clear image would result in the sublimation of the hailstone and the movement of particles from their original location within the stone. Prior hail-focused studies (e.g., Mandrioli et al. 1973; Michaud et al. 2014) have avoided these obstacles by melting and filtering the hailstone’s liquid water to determine the distribution of viable microorganisms within the hailstone, which limited the analysis to a specific subset of particles. Therefore, a new technique must be applied to hailstones to preserve their in situ particle distribution, including non-soluble particles, before taking advantage of these powerful microscopy techniques

Ice exhibits a sublimation point close to its melting point, making it feasible to separate out particles via sublimation. A particularly effective sublimation procedure, as described in Arena (2024), involves placing a thin section of an ice sample on a substrate within a dry environment,

allowing the ice to sublime gradually while ensuring minimal contamination during and after the sublimation process. Over time, the particles remain deposited on the substrate, facilitating their examination through microscopy techniques. By first coating the ice with an ultrathin layer of porous plastic, thus slowing the sublimation process, any potential drag or contamination of the trapped particles while handling the sample is prevented.

This coating technique was pioneered by Schaefer (1941) and subsequently refined by Higuchi (see Higuchi 1958; Higuchi and Muguruma 1958) for the creation of plastic replicas of ice surfaces. Both Higuchi and Muguruma applied thin layers of a coating made of polyvinyl formal (Formvar) dissolved in ethylene dichloride to the sample surface to facilitate ice sublimation through the formation of small pores in the plastic. Relatively shorter sublimation times within these pores led to the formation of thermal attack imprints (pits), enabling the examination of the sample's texture. This approach eliminates all water molecules while preserving the original spatial distribution of all particles, regardless of their size or composition. Consequently, the particles separated and trapped by the plastic coating can be examined using microscopic techniques such as CLSM or SEM–EDS at room temperature. This coating and sublimation technique serves as the basis for this present study. The following sections describe the novel application and expansion of this approach from hail collection to microscopy analysis and toward investigating the particle's (now including non-soluble) physicochemical characteristics and distributions within hailstones

2.2 Materials and methods

2.2.1 Hailstone collection

The hail collection procedure was an effort between the Universidad Nacional de Córdoba (UNC) and Argentinian citizens around the Córdoba Province. When Argentinian citizens collected hail, they took pictures with their hands or some other object as a scale reference and stored them in their fridges (commonly at $-13\text{ }^{\circ}\text{C}$). Argentinian citizens then contacted the Facultad de Matemática, Astronomía, Física y Computación (FAMAF) at UNC or Lucia E. Arena directly through the Cosecheros application or via telephone or WhatsApp to report the hail they collected. Once the hail report was made, a visit was scheduled with the person who collected the hailstone. During the visit, the location coordinates, the time of collection, the home freezer temperature, and information on whether it rained before, during, or after the hail is noted. The name of the person who collected the sample is recorded, and a document is signed that states that the individual is transferring the hail sample ownership to FAMAF for analysis.

The hailstone sample was transferred and kept in a nylon bag in a thermally reinforced cooler in which the temperature was controlled at $-15\text{ }^{\circ}\text{C}$. This temperature is chosen because the crystallographic structure changes are prolonged (significant changes in the crystallographic structure at this temperature may not start to happen after a year or more). This timeline, however, is not important for the type of analysis described in this paper because it is focused on particle composition, which is neither affected by the storage time nor the crystallographic properties of

the hailstone. Each sample was designated an alphanumeric identifier that included the name of the person who collected the sample. Once it reaches the laboratory, the hailstone surface is brushed (to remove contamination) and transferred to a cold chamber with a controlled temperature of $-15\text{ }^{\circ}\text{C}$. No additional cleaning procedure is considered since the hailstone has not melted, and the risk of further contamination is minimal. This hail collection and conservation procedure became the Argentine provincial citizen science program, Cosecheros de Granizo, which started in October 2018 (Arena and Crespo 2019; Crespo 2020).

2.2.2 Hailstone preparation with an adapted sublimation method

After cleaning the subzero facilities (refer to Appendix A), hail samples were processed in the subzero facility, the Laura Levi Atmospheric Physics Laboratory of FAMAFUNC, which is one of the few facilities in the world with the equipment to process hail. Upon the chamber reaching a temperature of $-12 \pm 2\text{ }^{\circ}\text{C}$, the chamber should be quickly entered to minimize heat exchange and maintain this required operating temperature for hailstone processing. After entering the chamber, the following hailstone measurements should be made first before the cutting of the hailstone (if needed) for additional physical analysis of the stone with respect to the lengths of the lobes, the height and width, the symmetry, and the weight.

The overall objective of the hailstone preparation process is to expose the embryo by cutting the hailstone. However, due to the coating machine's limited size, smaller thin section glasses are needed to fit the coating chamber. This strategic preparation ultimately serves the larger goal of entrapping the hailstone particles within a Formvar layer, a crucial step for subsequent microscopic

analysis. For this reason, a glass substrate is needed to affix the hailstone before cutting it into sections for analysis. Towards this goal, several thin glass sections, assembled in a mosaic pattern (Figure 2.2), were affixed to a larger piece of glass using ultrapure liquid water. Glass was selected as the substrate for particle deposition due to its transparency to visible light, enabling the examination of particles using transmitted light microscopes (i.e., CLSM). The hailstone was then attached to the glass by applying heat to the bottom of the hailstone to slightly melt the bottom surface, positioning it on the glass, and then allowing it to freeze once more (within minutes) until it firmly bonded to the glass surface. The glass is too thin to firmly grab when cutting the stone, so the hailstone, now firmly attached to the glass, is further affixed to a thick metal section plate using the same ultrapure liquid water (Figure 2.3a). The hailstone sample was then cut over the equatorial symmetric plane using a diamond-encrusted cutting disk with 12 cm diameter and a cutting width of 2 mm to expose the embryo (Figure 2.3b). While alternatives to the abovementioned disk are plausible (different sizes and cutting widths), they must adhere to specific criteria to achieve the best hailstone cutting performance: (1) the blade has to be as thin as possible to minimize removing hailstone mass during cutting, and (2) its edge must be adequately broad to facilitate cutting larger hailstones. After cutting, the sample is evenly polished with a microtome (Figure 2.4a) to provide a thin, even ice layer over the embryo (Figure 2.4b).

At this stage, pictures were taken to record the location of the growth rings relative to the embryo. Hence, we know where particles will be located relative to the embryo, allowing for future crystallographic and ice growth analysis. After taking pictures of the polished hailstone sample, a layer of 1 % Formvar solution diluted in ethylene dichloride (refer to Appendix B) is applied to the sample's flat polished surface using a clean glass rod. This application is done in two ways,

either (1) by dipping one side of the rod into the Formvar solution and spreading a small amount over the surface or (2) by pouring small amounts of the solution onto the surface and evenly spreading it across the polished hailstone. Once the entire surface is covered with the Formvar solution, the sample is left to cure for a few minutes, and then it is ready for sublimation. The hailstone is left in a sealed low-humidity container with silica gel (Figure 2.4c) at the $-12\text{ }^{\circ}\text{C}$ operating temperature to sublime it. This process enabled the gradual sublimation of ice over a 24 to 48 h period, with daily sample monitoring, while also capturing non-soluble particles beneath the layer of the Formvar solution. During sublimation, dissolved components may undergo precipitation. For instance, in cases where the original hailstone possessed a brine-like composition, the sublimation process could result in the precipitation of once-soluble salt particles. However, in convective systems, the behavior of soluble components such as sodium chloride and other crystalline inorganic salts is influenced by multiple factors, such as solution properties and convective transport processes (e.g., updraft speed). When these get injected into an updraft, they have the potential to remain undissolved, acting as INPs under certain conditions (Patnaude et al. 2021). Consequently, discerning between particles that were initially non soluble and those that became non-soluble post-sublimation poses a challenge and is not the primary focus of this paper. However, it is known to a certain degree that some particles were not originally precipitated from the sublimation process, owing to their specific composition determined by the SEM-EDS technique described in the next section.

2.1.3 Microscopy analysis

2.3.3.1 CLSM analysis

Once the sample is completely sublimated, and once particles are trapped in Formvar, it is ready for microscopy analysis. An Olympus LEXT OLS4000 confocal laser scanning microscope (CLSM) is used to create a 2-D cross section of the sublimated hailstone (centered on the embryo location) along an axis in the equatorial plane using the lowest available magnification (108x) to locate the non-soluble particles trapped in Formvar. Within this cross section (Figure 2.5a), subsectors are selected with respect to the embryo center for higher magnification (Figure 2.5b), with the color image (Figure 2.5c) providing high-resolution 3-D particle surface topography and, therefore, the size (Figure 2.5e) of individual particles within all subsectors of the scanned 2-D cross section. The magnification is dependent on the size of the particle to be analyzed. It is estimated that using the modified sublimation technique, particles trapped in Formvar can be observed using the CLSM as small as 1 μm , thus requiring magnification of 2132x. Each particle is individually labeled for further analysis. CLSM files undergo processing using ProfilmOnline software (e.g., as displayed in Figure 2.5e; Filmetrics 2017), facilitating the extraction of essential particle information. During this stage, the particle size is determined by assessing the maximum length along the x and y axes. The obtained data on particle size, coupled with the spatial distribution of each particle, lay the foundation for the subsequent SEM–EDS analysis, as detailed in the following section.

2.3.3.2 SEM–EDS analysis

The 2-D cross section created with the CLSM (Figure 2.5a) is used as a reference point to investigate the elemental composition of the individual particles. Elemental analysis with SEM–EDS was conducted on electrically conductive samples under high-vacuum conditions to enhance the imaging quality and the accuracy of chemical measurements. This decision was influenced by the absence of a variable pressure mode (50 Pa) in the SEM instrument used in the development of this method. Even if such an instrument were available, a high-vacuum environment would still be preferred. SEMs equipped for low-vacuum analysis introduce a controlled gas, such as nitrogen, or allow some oxygen from the surrounding air to enter the chamber, potentially leading to aerial contamination. Without a dedicated oxygen source or air filtration system, SEM chambers risk contamination from atmospheric impurities. This is because SEMs do not have built-in air filtration systems. These impurities can settle on the Formvar coat. Without proper references from CLSM or SEM, they could be mistakenly included in the particulate selection analyzed with this method.

Moreover, under low-vacuum conditions, beam-skirting can occur (Goldstein et al. 2017), wherein the gaseous environment alters the profile of the primary electron beam. This alteration typically divides the electron beam into two fractions: an unscattered beam with the original distribution profile and diameter and a scattered beam forming a “beam-skirting” around it. This modification occurs prior to reaching the particle surface, affecting the resolution of high-resolution imaging and spectral analysis through EDS. Consequently, a high-vacuum environment is recommended due to concerns regarding contamination, the lack of beam trajectory control, and the impact on resolution and spectral analysis.

To produce a fully conductive surface for the most accurate X-ray chemical analysis, the glass slides with hailstone particles were coated with 25 nm Au and analyzed at 10^{-4} Pa chamber pressure. Gold coating was selected over other common coating materials (Au, Au–Pd alloy, Pd, Pt, Ir, C, and Ag) to enable the characterization of C-bearing non-soluble particles without X-ray interferences at the C–K α position or with other elements that may exist in hailstone particles. The sample was analyzed with a Zeiss Sigma field emission gun (FEG) SEM with an EDS X Max 80 mm² detector at the Laboratorio de Análisis de Materiales por Espectrometría de Rayos X (Lamarx) facilities at UNC.

Analysis of micron-scale non-soluble particles involves optimizing both the spatial resolution of the electron imaging and the activation volume of X-ray analysis. Selecting the accelerating voltage is critical to the determination of the ultimate resolution of the imaging and X-ray analysis. The accelerating voltage of the primary beam determines the wavelength of the electrons, and higher voltages are generally advised for enhanced spatial resolution in electron imaging (Goldstein et al. 2017). However, it is important to consider that this principle may not universally apply to all materials. In some cases, excessively high voltages could result in electron expansion or penetration into the materials, potentially diminishing resolution. Therefore, it is essential to determine the optimal voltage, potentially opting for a lower one, when analyzing specific samples to ensure an optimal imaging resolution. By balancing the energy of the incident beam, it is possible to excite all of the X-ray lines of interest from the smallest possible volume. Additionally, depending on the object being analyzed, increasing the voltage increases the risk of beam damage to the particle (e.g., Figure 2.6), thereby jeopardizing the sample's integrity and subsequently influencing the conclusive outcomes of this method. On the other hand, the working distance can

affect the depth of the field and beam diameter, which will also affect the clarity and resolution of the image of an object. Optimizing the accelerating voltage and working distance will define the clarity, detail, and accuracy of the imagery obtained from an SEM.

The working conditions of the accelerating voltage of 15 kV and working distance of 8.5 mm were set for creating the secondary electron image (also referred to as a micrograph) shown in Figure 2.7a. For these conditions, at a magnification of 1.14 kx, particles as small as 1 μm trapped in the Formvar solution are observed in the SEM. These SEM identified particles are then compared to CLSM image locations to ensure that the same particle from the CLSM imagery is the one being targeted in the SEM (e.g., Figures. 2.6c and 2.7a) for EDS spectrum analysis.

EDS analysis is conducted for every particle identified in the SEM imagery to determine the major and minor element composition of the non-soluble particles trapped in the hailstone sample (Figure 2.7b) using the same voltage defined for electron imaging. The choice of 15 kV ensures that heavier elements are included in the EDS analysis by exciting the K lines of elements such as Fe. However, owing to attaching the hailstone to a glass substrate, a lower voltage may reduce background noise. Specific to soda–lime glass, elements such as Si, Na, Ca, Mg, K, and Al may be introduced into the EDS spectral analysis from the glass. To evaluate this effect, Monte Carlo simulations of electron trajectories in solids (CASINO; Drouin et al. 2007) were conducted for 15 and 8 kV with 0.25 μm beam (Figure 2.8). Results indicate that for a small grain of biotite particle with a 7 nm layer of Formvar, some X-rays are emitted from the glass substrate for particles smaller than 1.5 μm at 15 kV that can be minimized using the 8 kV accelerating voltage. While this suggests that the soda–lime glass can exert minimal impact on the

spectral readings for particles down to 1 μm minimum size at 8 kV, a single-point analysis approach can further reduce the potential spectral contamination.

An example of the single-point technique is highlighted in Figure 2.7a, where the EDS measurement is first taken at a point within the red circle where no glass substrate is present (i.e., focused entirely on a section of the particle). Multiple single-point measurements made at least 10 μm apart prevent overlap and capture the composition variability through the particle. Multiple EDS point measurements are essential for assuring the representative particle composition for particles showing varying optical properties in the CLSM color imagery (e.g., Figure 2.5d). Figure 7b shows the corresponding output from the SEM–EDS analysis of the particle in Figure 2.7a. Micrographs of individual particles (e.g., Figure 2.7a) and EDS data are crucial in particle classification (e.g., carbonaceous [biological, organic, or inorganic], silicates) based on elemental composition. Additionally, the high-resolution geometry information of each individual particle can be compared to universally known standards to increase the confidence of the particle classification. Micrographs are also complementary in ensuring that EDS spectra are accurately attributed to the same particle analyzed using the CLSM.

2.3 Application of the microscopy technique to hailstones

The outcomes of the methodology are first applied to a 4 cm hailstone (Figure 2.9) and are introduced here to gain insights into the physicochemical properties of non-soluble particles. This hailstone originated from a supercell storm in Villa Carlos Paz, Argentina, on 8 February 2018 (Kumjian et al. 2020; Bernal Ayala et al. 2022). Using our method, we uniquely determine the non-

soluble particles' sizes and elemental composition relative to their location in the hailstone. For this methodology, randomly selected particles with a diameter larger than 1 μm were analyzed. As shown in Figure 2.9, different cross sections of the same hailstone were selected to measure the particle size distribution, using CLSM and elemental composition via SEM-EDS, preserving the in-situ location relative to the embryo.

As seen in Figure 2.10a–b, the CLSM particle size distribution for V-7 reveals that particles range from 2 to 150 μm . In the V-7V cross section (Figure 2.10a), most particles have major axis lengths between 2 and 60 μm , whereas in the V-7H cross section (Figure 2.10b), most particles are relatively smaller, falling between 2 and 45 μm . Two additional hailstones of 8 cm each (V-16 and V-17), collected from the same storm, were also analyzed and compared to V-7. The different axis ranges in this figure represent the varying number of particles analyzed and differences in the size range from these differently sized hailstones and, consequently, their analyzed cross sections. Particles in both V-16 (Figure 2.10c) and V-17 (Figure 2.10d) tend to be larger compared to those in V-7. However, particles larger than 100 μm were identified in all three hailstones collected from the same supercell.

CLSM also provides topographical and shape information about the analyzed particles, as shown in Figure 2.11, which is crucial for understanding ice nucleation processes in clouds; however, a detailed analysis of the topography and shape of the particles is reserved for a future publication focusing on the applications of this method. Surface topography is an active site for ice nucleation, influencing nucleation modes and the energy barrier for ice formation. This aligns with findings from Holden et al. (2021), suggesting that surface topography plays a significant role in ice

nucleation. Additionally, other laboratory studies (e.g., Gao et al. 2022) have demonstrated that the particle shape, size, and coating can impact the ice nucleation ability of particles, including soot. The paper by Gao et al. (2022) shows that coatings or internal mixing have resulted in different ice nucleation abilities compared to bare particles. Importantly, these studies emphasize that the particle size is not the sole determinant, highlighting the critical role of surface topography and particle shape in influencing atmospheric ice nucleation.

To characterize the elemental composition of the non-soluble particles from the SEM–EDS analysis (e.g., Figure 2.7b), a statistically based clustering method was applied based on elemental weight percentages (e.g., Laskin et al. 2012). Prior to the analysis, the types of particles present in the hailstone were unknown, motivating the use of cluster analysis to identify the dominant element within each particle. The Orange k-means clustering algorithm (Demšar et al. 2013) was used, providing silhouette scores of clustering results for various k values, where higher scores indicate better clustering. This approach enabled the identification of particle similarities based on statistical clustering. Subsequently, the predominant element within each category was determined, based on the knowledge of each particle's cluster. This approach resulted in five unique categories: carbon-based (C-based), carbon-based with heavier metals (C-heavy), silicon-based (Si-based), silicon-based with heavier metals (Si-heavy), and chloride-based (Cl-based), as illustrated in Figure 2.11 for the three most common categories.

Particles included in the C-based group had a C abundance greater than 10 % weight, with this abundance being higher than that of Cl and Si. Those categorized in the C-heavy group met the same criteria as the C-based group but also had an abundance greater than 1 % weight of heavier

metals such as Ti, Cr, Fe, Ni, Zn, Br, and Mo. Particles categorized in the Si-based group had a Si abundance greater than 10 % weight, with this abundance being higher than that of C and Cl. The Si-heavy group met the same criteria but had an abundance greater than 1 % weight of heavier metals such as Ti, Cr, Fe, Ni, Zn, Br, and Mo. Finally, particles with a Cl abundance greater than 10 % weight, with this abundance being higher than that of C or Si, were categorized in the Cl-based group. Using this characterization framework, it was found that most particles in both cross sections of V-7 were carbonaceous (C-based and C-heavy), followed by silicates (Si-based and Si-heavy) and salts (Cl-based), as shown in Figure 2.12.

A benefit of this method is the ability to isolate particles within the embryo compared to the outer layers. This allows the description of both the sizes and elemental compositions of particles that may have served in the nucleation process of the hailstone, similar to Michaud et al. (2014). Figure 13 isolates particles in the embryo regions of the V-7 cross sections, as V-7V and V-7H cross through the embryo (see Figure 2.9 for reference). In the embryo region, salts were not identified in the initial analysis of V-7V (as seen in Figure 2.13a). However, they were present in the additional horizontal cross section (Figure 2.13b; V-7H), along with heavier metals. Different particles were selected within the embryo sample to better elucidate the range of particle characteristics observed within this hailstone's embryo.

In summary, these findings highlight the robustness of our approach, revealing consistent overall messages while emphasizing the benefits of examining multiple cross sections in a single stone. This method is particularly valuable for identifying a diverse range of elemental components. Within hailstones from the same storm, there appears to be a noticeable shift in the particle size

corresponding to the hailstone's increasing size, which is an interesting result to explore further. This unique method preserves the particle size and elemental composition relative to the embryo, offering insights into the correlation between the particle size, elemental distribution, and their origins in different cloud regions during hail formation. Such insights will contribute to a deeper understanding of nucleation properties and the source regions influencing hail formation and growth with the application of this technique to additional hailstones from various storm types and environments.

2.4 Limitations and Recommendations

This section discusses some limitations of the microscopy analysis technique, offering suggestions to mitigate these constraints and enhance the analysis by incorporating complementary techniques. A unique aspect of this work is the characterization of individual particles. While beneficial, it is also a time-consuming process. For instance, the analysis examined 176 particles using 9 h of CLSM and 20 h of SEM-EDS. There are pathways to consider when optimizing SEM-EDS analysis. Studies like those conducted by Lata et al. (2021) and Diep et al. (2022) have utilized a computer-controlled SEM-EDS (CCSEM) microscope for elemental chemical composition analyses, enabling the analysis of a larger number of particles, while emphasizing interpretation. A computer-controlled (CC) SEM-EDS system incorporates additional software facilitating automated analysis, including automated sample loading, stage movement, focusing, imaging, and elemental analysis. CCSEM-EDS software can be programmed to autonomously analyze multiple particles consecutively without human intervention (Vander Wood 1994). Utilizing CCSEM-EDS streamlines the analysis process and optimizes the funds allocated for this instrumentation.

Second, Sect. 3.3.2 noted the potential introduction of elements into the EDS spectral analysis from the substrate, which is glass in this case. As previously mentioned, higher voltages provide a more accurate analysis of heavier elements but can introduce more contamination from the glass. The single-point measurement technique described in Sect. 3.3.2 provides a solution, while introducing more labor intensive steps to the process. Two recommendations, therefore, emerge: (1) measuring particle-free areas of the glass using the EDS to obtain a control elemental spectrum from the glass or (2) decreasing the accelerating voltage to 8 kV to reduce the background interference and then rerunning the EDS analysis with a higher (e.g., 15 kV) voltage only on those particles showing the presence of heavier elements to increase accuracy in those composition measurements. Varying the voltages in the EDS analysis in the context of this type of particle analysis is uncommon in the literature and may provide more confidence when characterizing non-soluble particles. Furthermore, to validate an individual particle's EDS spectrum result, spectrum mathematical operations were performed using the National Institute of Standards and Technology (NIST) DTSA-II program (Ritchie 2010) to mitigate potential contamination originating from the glass substrate associated with a specific particle, as illustrated in Figure 2.14. The analysis revealed that it is possible to eliminate potential glass-related spectrum contaminants from the particle's spectral results (Figure 2.14c) by subtracting the glass-related spectrum (Figure 2.14b) from the particle-related spectrum (Figure 2.14a). Spectral subtraction of particles from the underlying substrate enables more confident interpretations of element identity and abundance from non-soluble particles mounted on a glass substrate.

Due to the chemical composition of Formvar, the decision was made to quantify the contribution of C to the EDS spectral results when analyzing C-based particles using this technique. Potential

C signals were compared in clear glass sections (i.e., not containing visible particles) with and without Formvar. Additionally, C signals associated with particles categorized as carbonaceous were examined to discern any significant differences in the presence of C. Results confirm minor contributions of C from Formvar, as illustrated in Figure 2.15. Due to its minimal thickness, the impact of the Formvar layer on the C signal is deemed negligible.

Further analysis using different microscopy techniques should be explored to more precisely categorize carbon-based particles into biological, organic, and inorganic categories. For example, Raman spectroscopy could aid the particle characterization by complementing the SEM–EDS analysis, which does not provide enough information to discriminate different forms of Carbon in the sample. Raman spectroscopy is a non-destructive chemical analysis technique that provides insights into a material’s chemical structure, phase, polymorphy, crystallinity, and molecular interactions (Orlando et al. 2021). This technique yields unique chemical fingerprints, enabling swift identification and differentiation from other substances (Dahal 2022). By combining Raman spectroscopy with complementary imaging methods, like the SEM–EDS analysis used in this study, researchers could compare Raman distribution maps with topographical or morphological images, correlating Raman spectra with complementary SEM–EDS elemental information.

Additionally, scanning transmission X-ray microscopy (STXM) coupled with near-edge X-ray absorption finestructure (NEXAFS) spectroscopy can be explored to distinguish between organic and inorganic carbon (Lehmann et al. 2005; Moffet et al. 2011; Fallica et al. 2018; Lata et al. 2021). NEXAFS spectroscopy exploits the photoexcitation of electrons from a core level to unoccupied molecular orbitals to probe the specific chemical environment of a given element (Fallica et al.,

2018). Mapping the distribution of organic carbon at the K-absorption edge of carbon could aid in further distinguishing between organic and inorganic carbon, since STXM and/or NEXAFS applications have been used in atmospheric aerosol research (Moffet et al., 2011; Lata et al., 2021) and soil mapping research (Lehmann et al., 2005) to improve organic and inorganic carbon characterization.

2.5 Conclusions

Analyzing hailstone samples through the proposed methodology offers a promising avenue for gaining deeper insights into hailstones' composition, structure, and properties. This method has addressed and resolved several limitations observed in previous studies of collected hailstones by shifting the focus from melting to sublimating the hailstone, thus preserving the in situ particle distribution of all non-soluble particles within hailstones. This approach enables the identification of individual particles across each layer of the hailstone, including the embryo and air bubble rings. This approach, therefore, provides a precise representation of the particle distribution and allows for the correlation of these data with the corresponding rings associated with specific growth zones within the cloud.

The integration of CLSM and SEM–EDS combines two powerful analytical techniques contributing to a comprehensive understanding of hailstones' microphysics and developmental processes. CLSM enables the characterization of non soluble particles, revealing insights into particle size, surface topography, and early-ice-nucleation stages. SEM–EDS complements this by providing detailed elemental compositions, facilitating particle classification based on

composition. Using a protective porous plastic coating preserves the sample integrity, ensuring comprehensive analysis of particle spectra. These findings underscore the method's robustness in identifying diverse elements and revealing correlations between particle size, elemental distribution, and their origins in different cloud regions during hail formation. Applying these methods to hailstones from the same storm allowed us to isolate the particle characteristics within the embryo, highlighting a noticeable shift in particle size with increasing hailstone size and providing opportunities for new insights into our understanding of nucleation properties and factors influencing hail growth.

While this proposed method offers significant advantages in providing more comprehensive data on the individual non-soluble particles trapped in a hailstone, it has some limitations. The optimization of human resources could be achieved by incorporating a CCSEM–EDS microscope, allowing for a more efficient allocation of time toward the interpretation of each individual particle's species. Additionally, while efforts have been made to minimize the impact of the glass substrate background noise on EDS spectral analysis, caution should still be exercised when interpreting spectral results, especially for particles near the lower particle size limit.

The innovative approach outlined in this paper presents a valuable contribution to the field of hailstone analysis. By combining powerful and high-resolution microscopy techniques and meticulous sample preparation, researchers can better uncover the intricate details of hailstone composition and properties, which can give insights into hail developmental processes. When applied to additional hailstones from different storm types and environments, this method

will enhance our understanding of atmospheric particles' role in hailstone microphysics and contribute to advancements in weather forecasting, mitigation strategies, and climate change modeling.

2.6 Appendix A: Cleaning protocol for quasi-clean subzero facilities

There are risks involved throughout the acquisition process and subsequent handling, leading to potential contamination and particle loss. Possible contamination sources during the processing of a hailstone may include the ultrapure water used, laboratory air, air from the dry container (silica gel dish), and the Formvar solution. The adapted sublimation particle separation procedure (described in Sect. 2.4) reduces these contamination sources compared to traditional methods that melt hailstones because the hailstone never transitions to the liquid phase; the diffusion coefficients of contaminants in the liquid phase (at 0 °C; $4 \times 10^{-9} \text{ m}^2\text{s}^{-1}$; Pruppacher 1972) are at least 1 order of magnitude higher than in the solid phase (ice; $4 \times 10^{-15} \text{ m}^2\text{s}^{-1}$; Petrenko and Whitworth 1999). Nevertheless, a systematic approach is needed to identify and manage potential contamination sources, including the operator, the working environment, and the materials and tools employed in processing the sample until the particle deposit is completed and the sample is ready for further microscopy analyses.

The subzero facility used for the development of the microscopy method is composed of two rooms, namely a prechamber (entry chamber) and a working chamber; this approach is to minimize the introduction of possible contaminants when processing samples. Metal walls and floors were first cleaned with a detergent solution, rinsed with tap water, and disinfected with sodium hypochlorite

(commonly used as a disinfectant and bleaching agent); this was done using water with low-lint mops without typical cleaning chemicals, rinsing for a second time with clean water, and later rinsing for the last time with ultrapure water. The rooms do not have an air-filter system. Due to the absence of a filtration system, given that the hailstone consists of ultrapure water, it is particularly susceptible to absorbing airborne impurities, which could compromise sample integrity. However, due to the objectives of this method, this was not a concern at this time, since this procedure is only meant to prevent contamination as much as possible without having to spend significant funds on chemical decontamination services – hence only achieving a quasi-clean room for hailstone preparation. All the equipment used to process thin sheets of ice was also washed with ultrapure water. The glass slides were degreased with a non-ionic detergent and then rinsed multiple times with ultrapure water. The slides were then dried in a clean, quasi-closed container at room temperature without a paper towel. Every operator used protective suits for the cold with an external waterproof fabric. The suits were washed using traditional detergent and rinsed multiple times using water alone. Each operator wore two gloves: the base was made of wool for protection from the cold, and a second latex glove was on top. Common plastic glasses for eye protection were used.

2.7 Appendix B: Optimum thickness of the porous plastic coating layer

Beyond the risk of introducing contaminants into the substrate, certain particles might move from their original location during handling or in coating procedures affected by vacuum pressures needed for SEM–EDS analyses. As previously mentioned, a way to address this limitation is to apply a Formvar solution film over the sample. Determining the ideal plastic coating layer

thickness is essential to using the adapted sublimation method effectively described in Sect. 2.3. Achieving the right mixture of Formvar and ethylene dichloride is essential; the layer must be sufficiently thick to trap particles in the hailstone, while remaining thin enough to reduce the sublimation duration (24 to 48 h and not weeks). Additionally, it must be thin enough to allow the SEM electron beam to penetrate the plastic coating to analyze particles, as seen in Figure 2.1.

Because Formvar is transparent, the plastic layer thickness presents no major limitations to analyzing particles in a sublimated hailstone sample with the CLSM. However, the thickness limitation is of greater concern when preparing the sample for SEM–EDS analysis to determine the elemental chemical composition of particles. For samples to be analyzed using the SEM, they must be coated with a layer of electrically conductive material, typically with a layer of a metal coating, with thickness of the order of 25 nm, in a vacuum environment of 5×10^{-2} mbar. Additionally, after coating, the sample is inserted into a chamber in the SEM instrumentation that undergoes a vacuum of 5×10^{-5} mbar or greater. If no plastic coating was applied to the sublimated hailstone sample, then the vacuum process in both previously described scenarios could remove particles, which makes it essential that the sample is covered with a protective film that keeps the particles trapped.

Multiple lab-grown ice samples were prepared and coated with one to three layers of the Formvar solution at 1 % and 3 % concentrations to address the thickness considerations and minimize particle displacement. This procedure consists of sweeping the polished surface of the ice sample with a rod dipped in the Formvar solution. The sample is then analyzed with CLSM, where an area exhibiting a distinct Formvar relief pattern is identified within the sample, as seen

in Figure 2.16 (top). Then, a transect across this pattern is used to measure the height of the relief (Figure 2.16, bottom) and thus determine the thickness of the Formvar layer. Thicknesses measured for multiple Formvar coatings are shown in Table 1. This approach determined that one layer of coating at 1 % Formvar thickness optimally addressed the aforementioned tradeoffs of the plastic coating, i.e., preserving particles while being able to see particles with the SEM (e.g., Figure 2.1).

2.8 Figures

Table 1: Formvar coating thicknesses measured with CLSM.

FORMVAR concentration	Number of FORMVAR layers		
	1	2	3
	Layer thickness in [μm]		
1%	0.007	0.031	0.100
3%	0.7	2.5	5.5

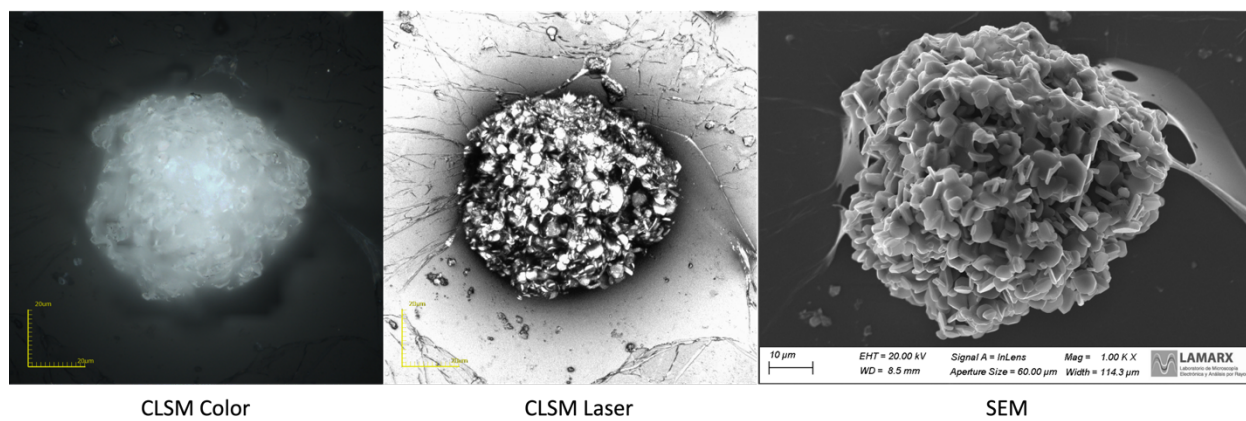


Figure 2.1: A particle trapped in a hailstone as observed by CLSM and SEM for the 1 % Formvar coating.

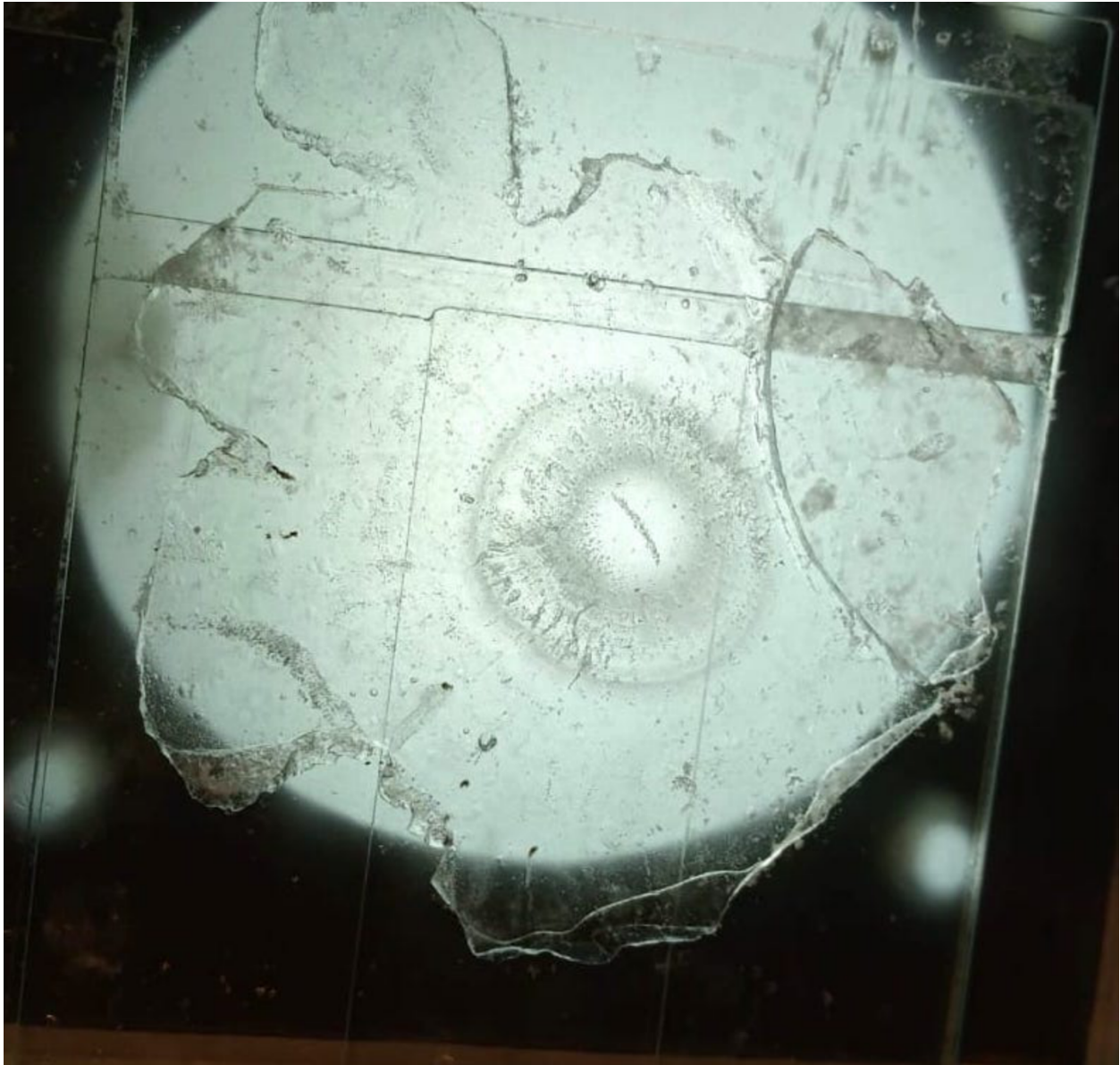


Figure 2.2: An example of a thin cross section of a hailstone sectioned through its equatorial plane. It is affixed to several thin glass sections arranged in a mosaic pattern on a thin glass slide with dimensions of 25×75 mm

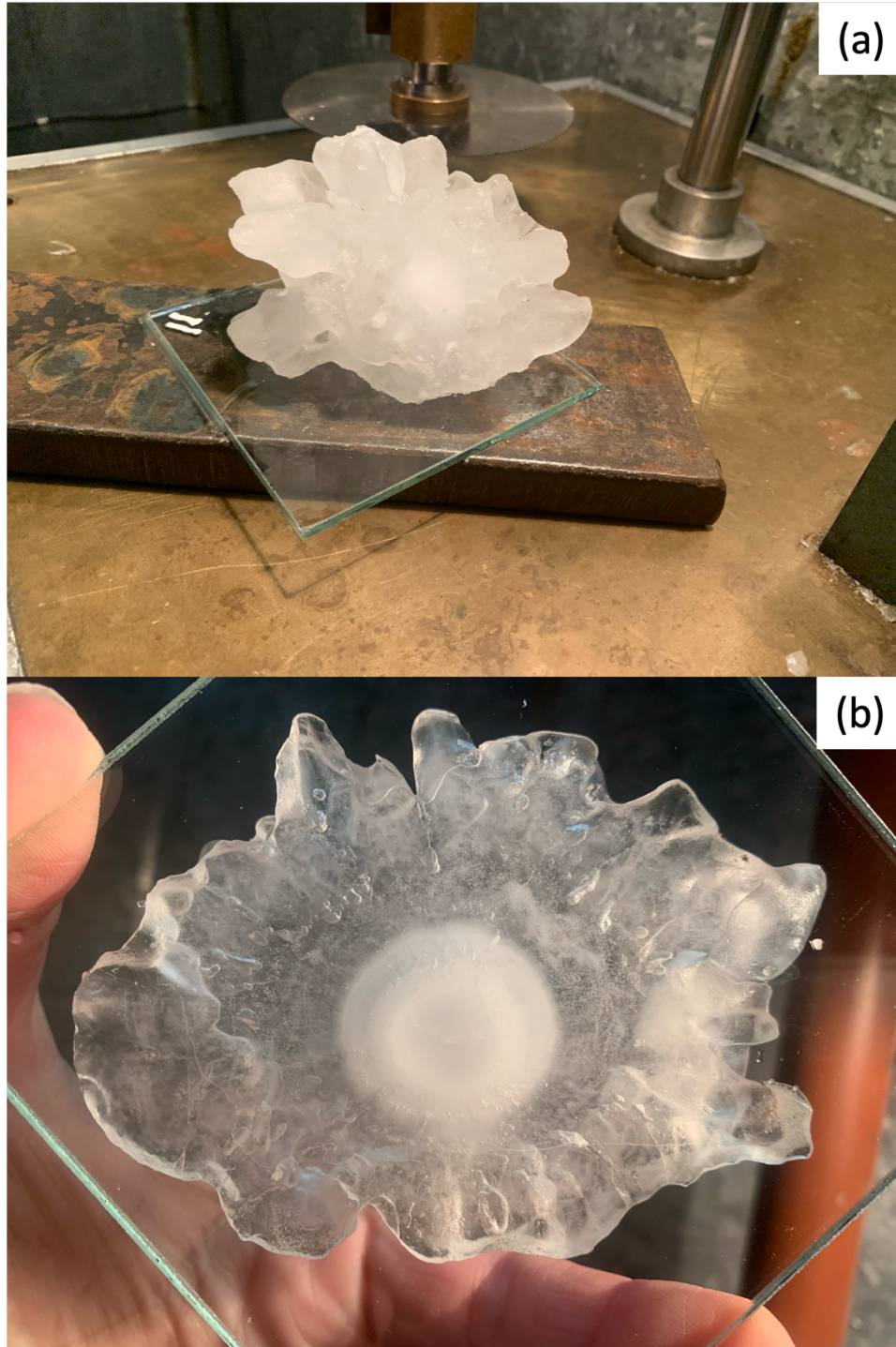


Figure 2.3: The figure shows the preparation stages of a hailstone. (a) The hailstone is attached to a glass section and then to a metal section plate with ultrapure liquid water. (b) The hailstone is cut in the equatorial symmetric plane to provide a view of the hailstone's embryo.

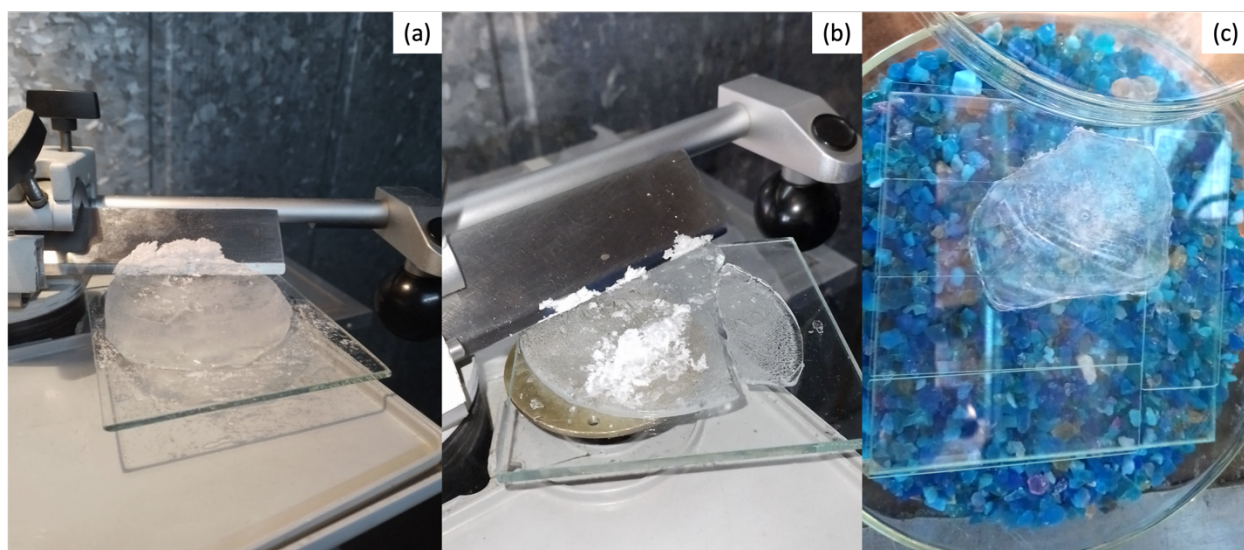


Figure 2.4: Images showing before (a) and after (b) a hailstone is evenly polished to the desired thickness with a microtome to obtain a top view of the embryo. (c) The hailstone is then left to sublimate in a humidity-controlled container with silica gel.

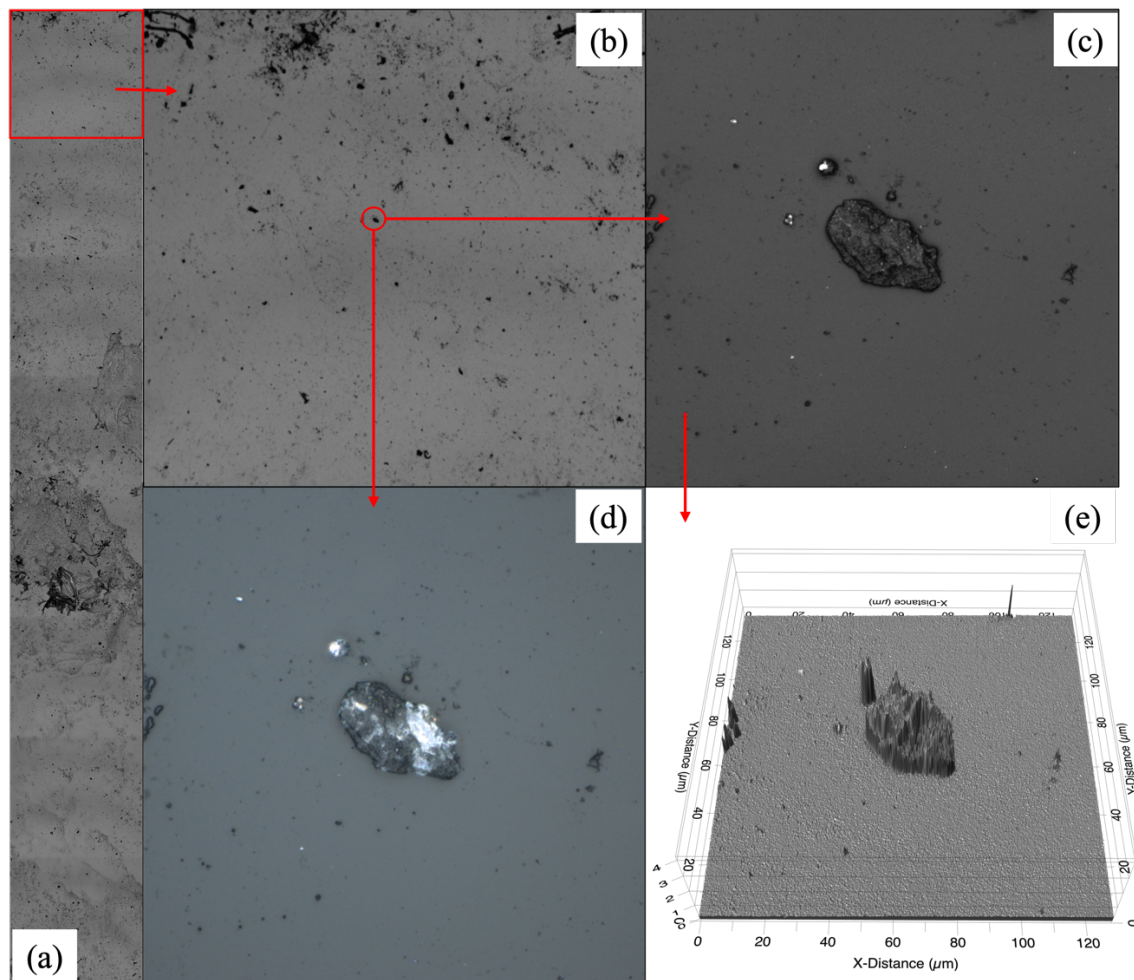


Figure 2.5: Example CLSM imagery from the coated, sublimated hailstone shows (a) a 2-D cross section along an axis in the equatorial plane at $108\times$ magnification and (b) a subsector scanned at higher magnification for creating (c) visible and (d) laser images for individual particles. (e) 3-D particle surface topography from the visible imagery is analyzed with ProfilmOnline software.

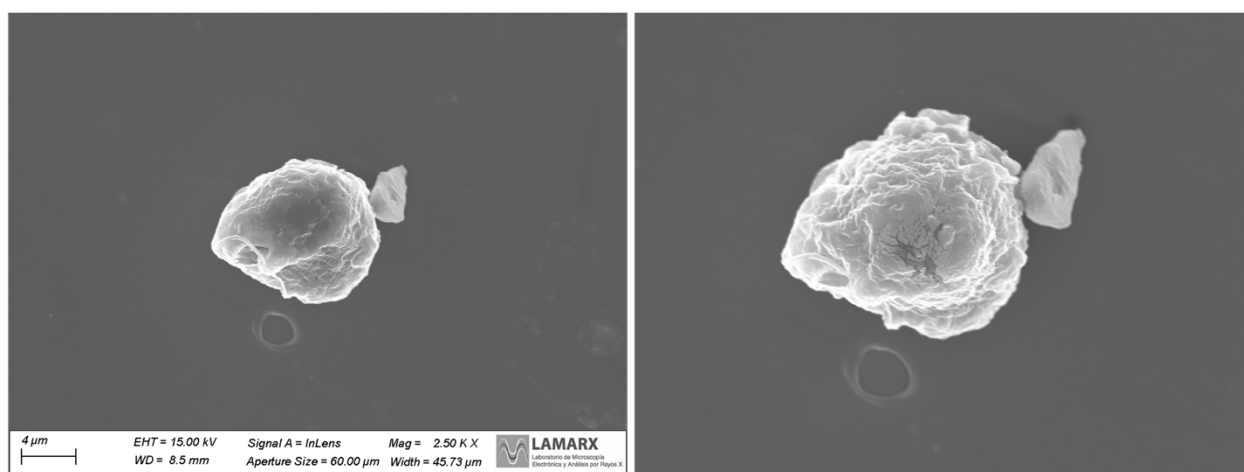


Figure 2.6: Panel (a) displays the particle prior to undergoing EDS analysis, while panel (b) illustrates the particle's post-EDS analysis, revealing subtle breakage and disintegration concentrated at the center of the particle where the SEM laser was centered.

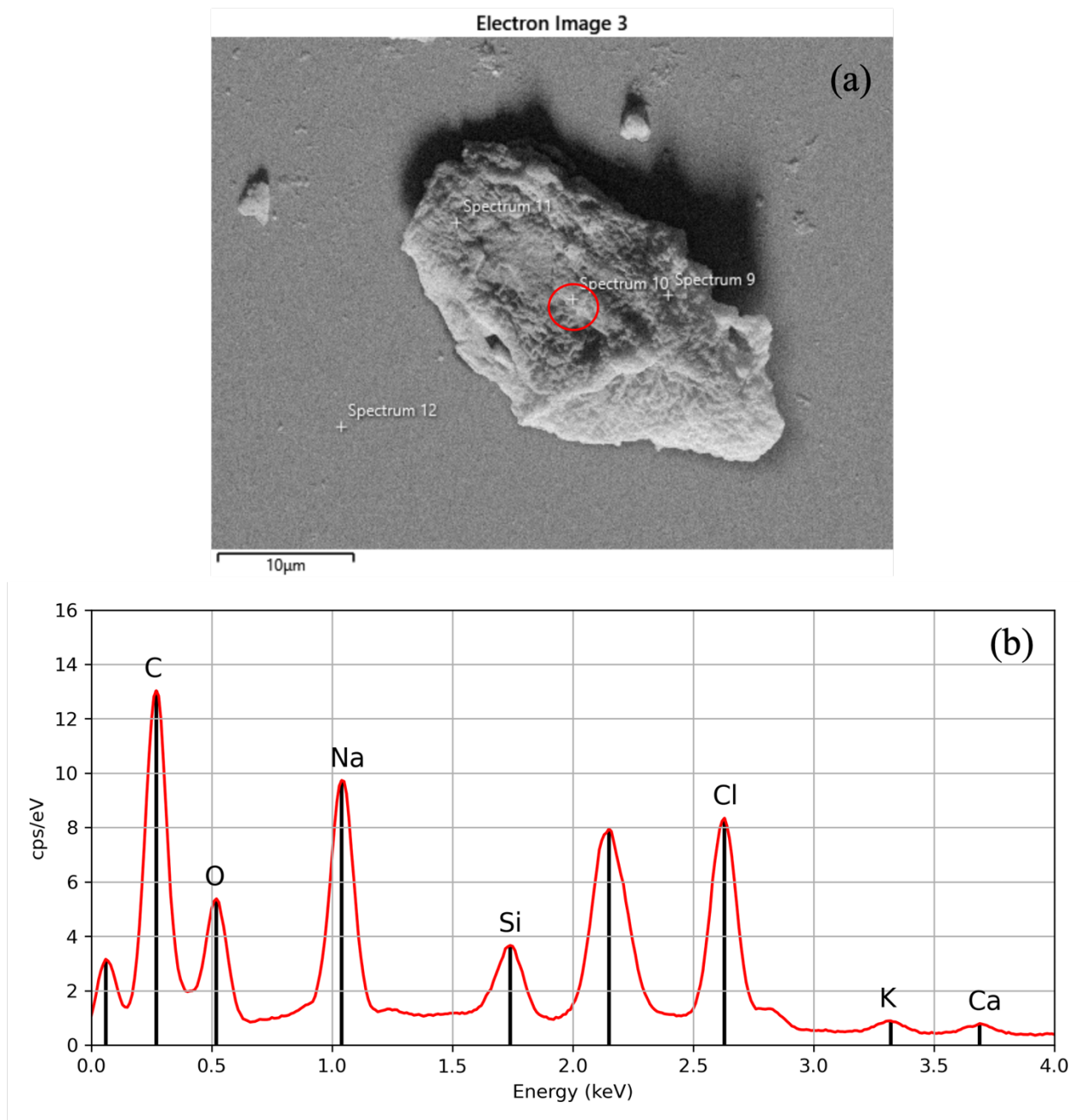


Figure 2.7: (a) A SEM backscattered-electron image for an individual particle categorized as carbon-based with (b) the corresponding EDS elemental composition for that particle. The first peak, closest to 0 keV, is caused by noise from the EDS detector and can be ignored when analyzing the elemental composition of a particle, as it does not represent any actual element. The second spectral peak corresponds to gold (2.12 keV) and was excluded from the analysis since it was used for coating the sample.

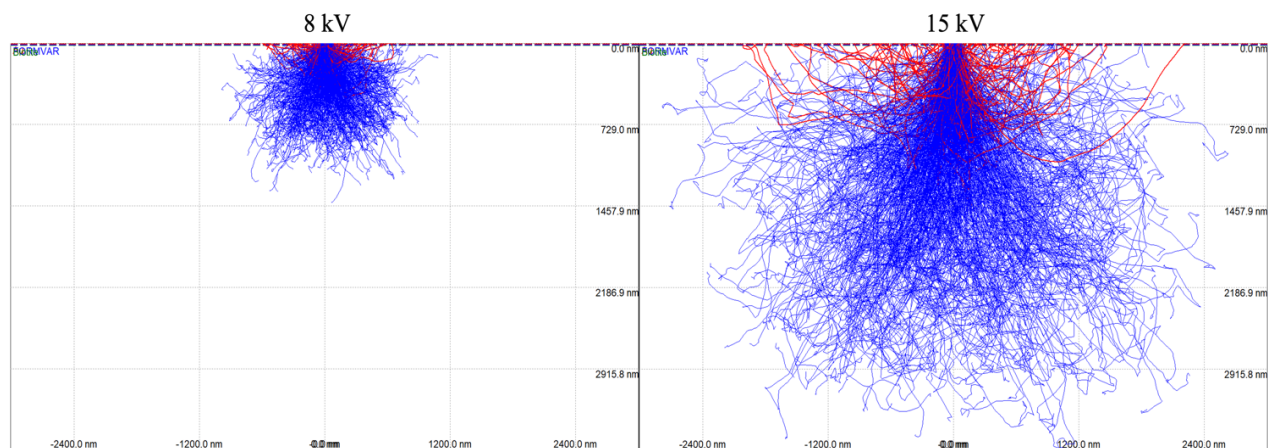


Figure 2.8: Activation volume producing Fe X-rays within the soda-lime glass for 8 kV (a) and 15 kV (b) accelerating voltage from the Monte Carlo simulations. Lines indicate the pathways of individual electrons backscattered from within the sample (blue) and from the sample surface (red) as a function of the particle size (in nm).

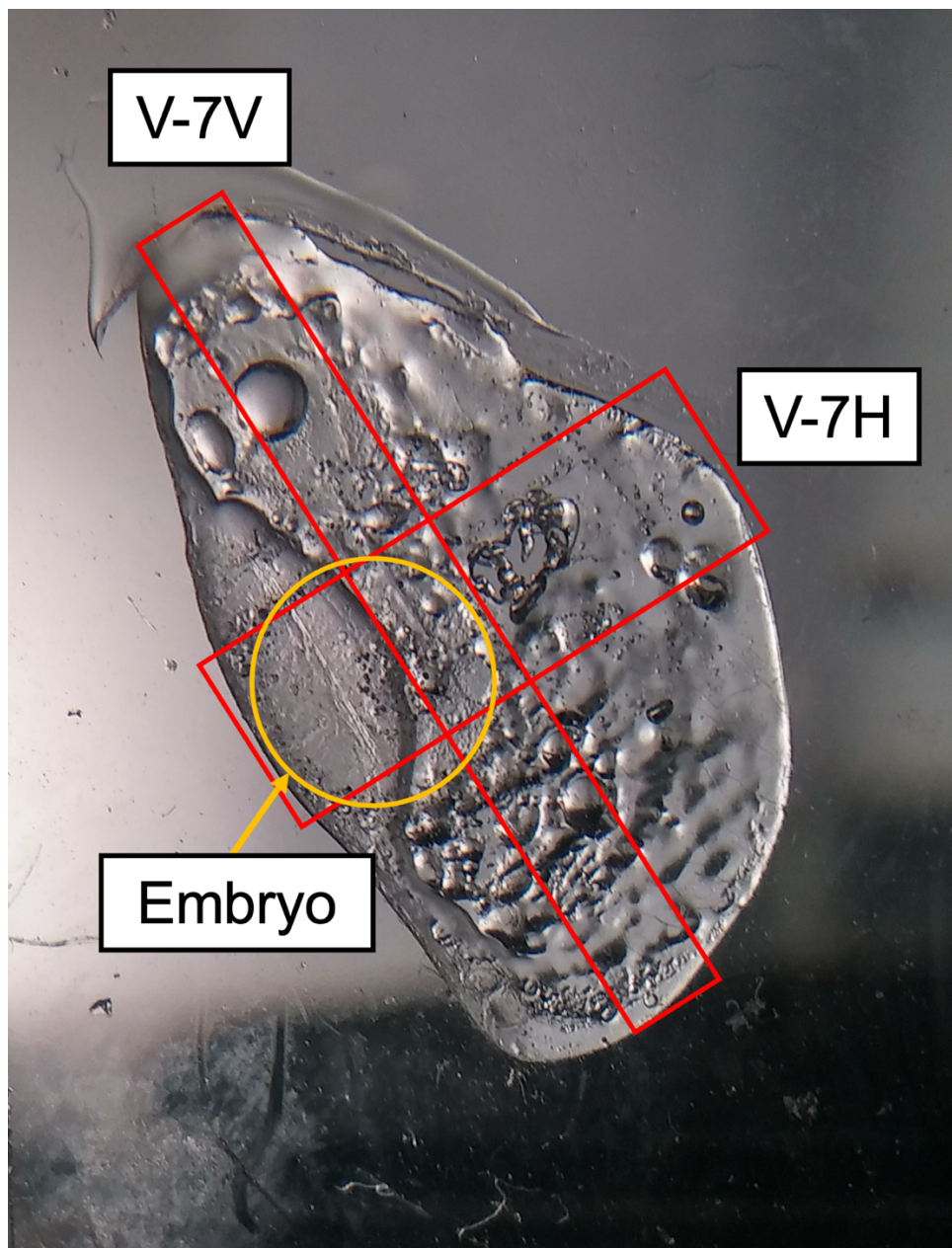


Figure 2.9: An example of an analyzed hailstone (V-7) for which the areas highlighted by red rectangles indicate where particles were randomly selected to measure the particle size distribution, using CLSM and elemental composition via SEM-EDS. The orange circle marks the location of the embryo.

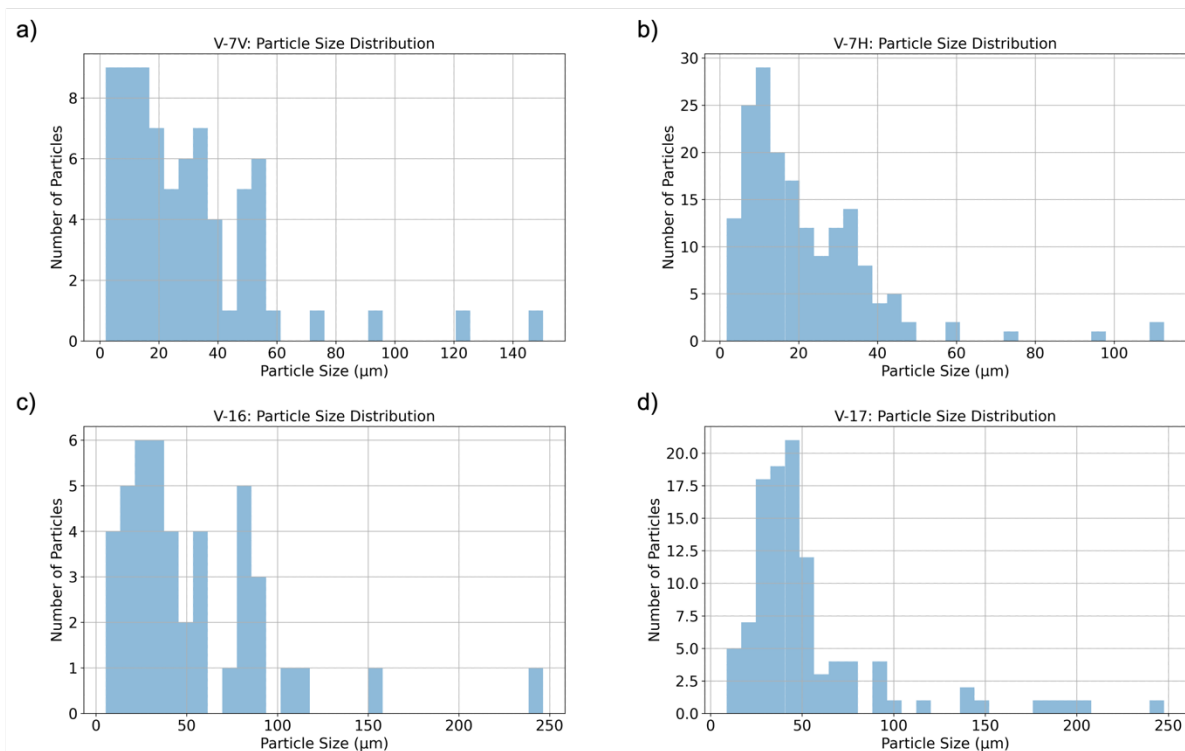


Figure 2.10: Particle size distributions for hailstone samples collected during the event on 8 February 2018. Panels (a) and (b) display particle sizes for two different cross sections from sample V-7, while panels (c) and (d) show particle sizes for samples V-16 and V-17, respectively.

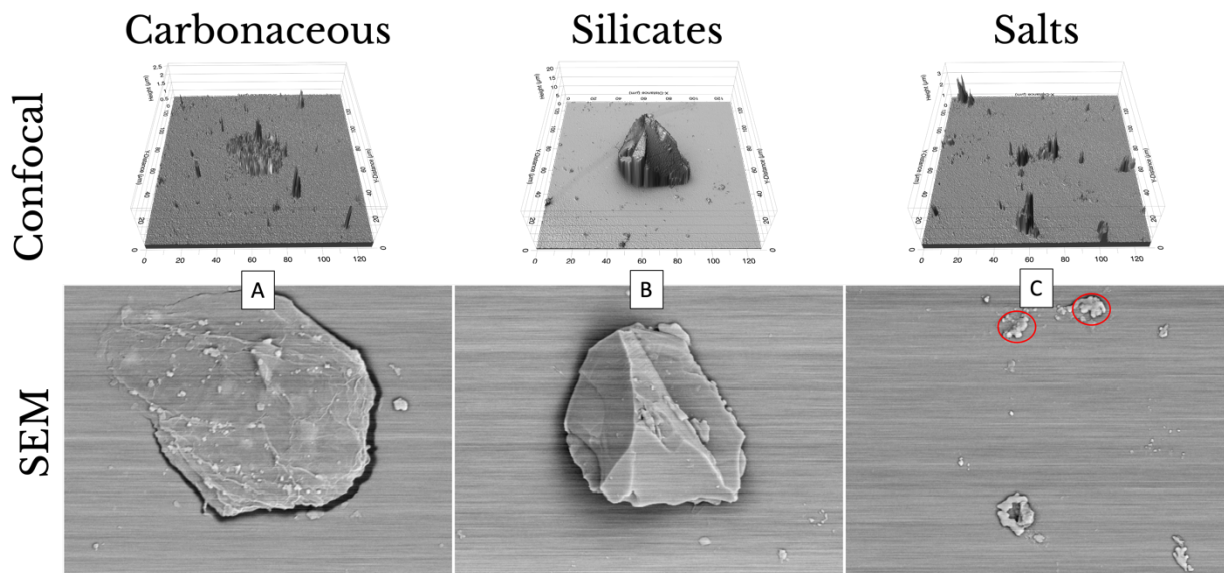


Figure 2.11: Examples from each of the primary particle categories are presented, along with their ProfilmOnline topographical output obtained through a confocal laser scanning microscope (CLSM; top), and accompanied by their corresponding scanning electron microscopy (SEM; bottom) image.

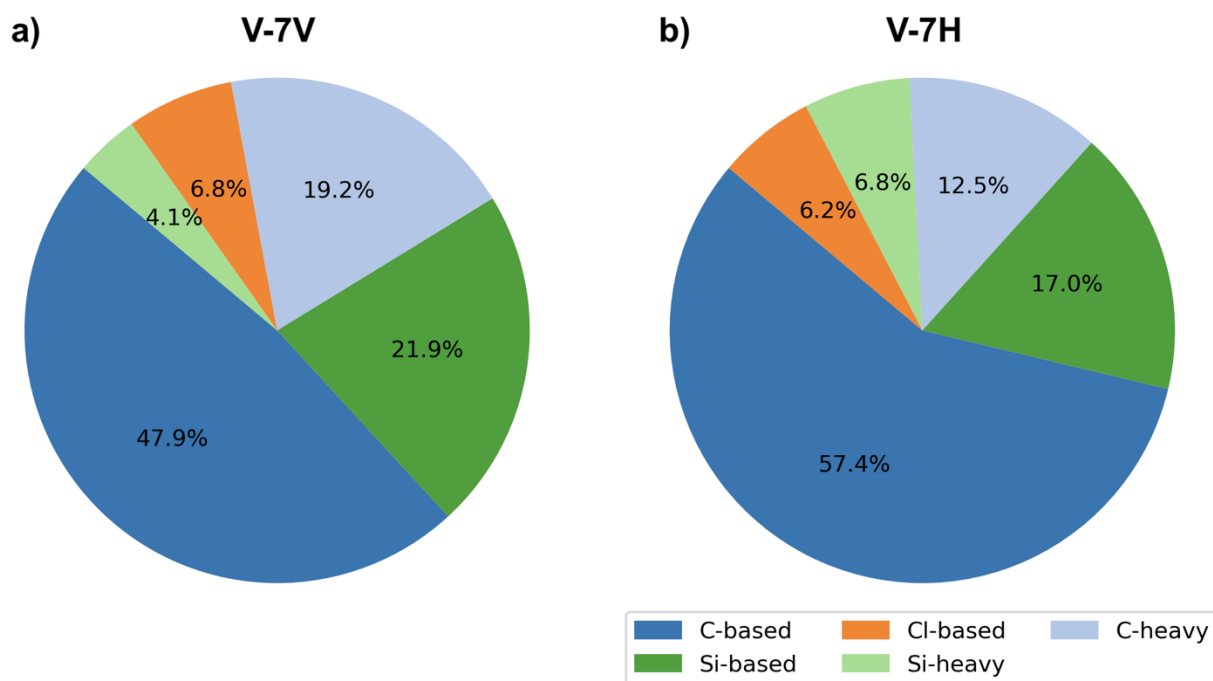


Figure 2.12: EDS-based elemental composition distribution of particles for (a) V-7V and (b) V-7H cross sections, as seen in Fig. 9.

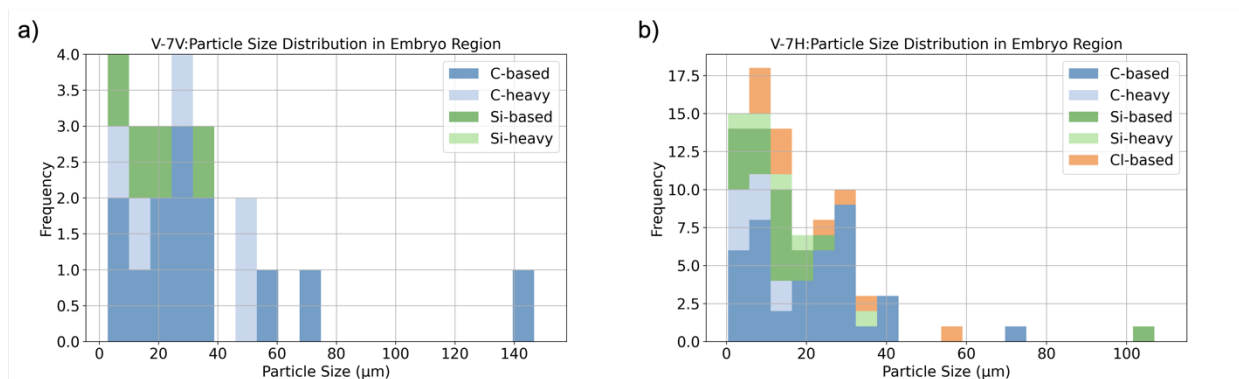


Figure 2.13: EDS-based elemental composition distribution of particles found in the embryo for sample V-7 for (a) V-7V and (b) V-7H.

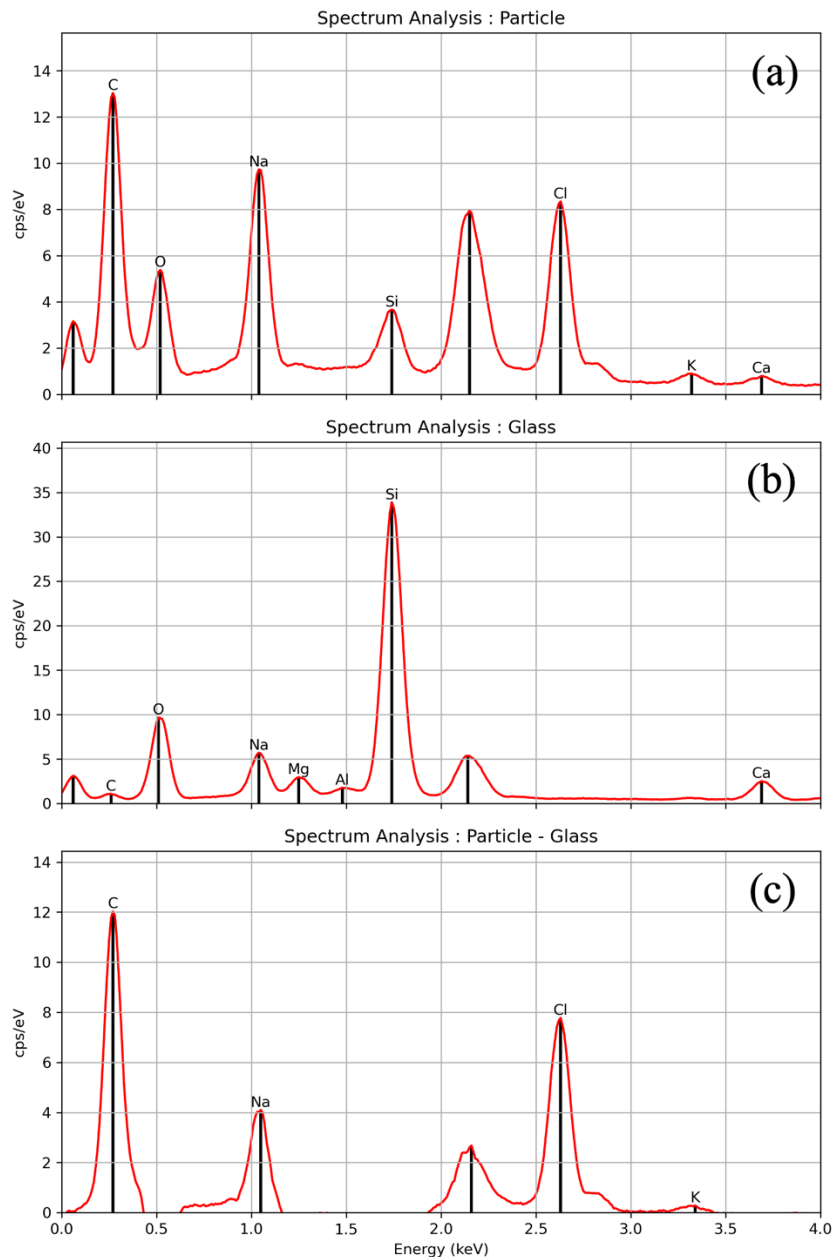


Figure 2.14: Mathematical operations on the spectrum using DTSAll were done to analyze the EDS spectrum data and differentiate a particle's spectrum from the glass substrate. Panel (a) depicts the spectrum of the particle presented in Fig. 7b. Panel (b) illustrates the spectrum of the glass. Panel (c) demonstrates the outcome of the subtraction, revealing the presence of elements C, Na, Cl, and K in the particle. The first peak, closest to 0 keV, is caused by noise from the EDS detector and can be ignored when analyzing the elemental composition of a particle, as it does not represent any actual element. The second spectral peak corresponds to gold (2.12 keV) and was excluded from the analysis since it was used for coating the sample.

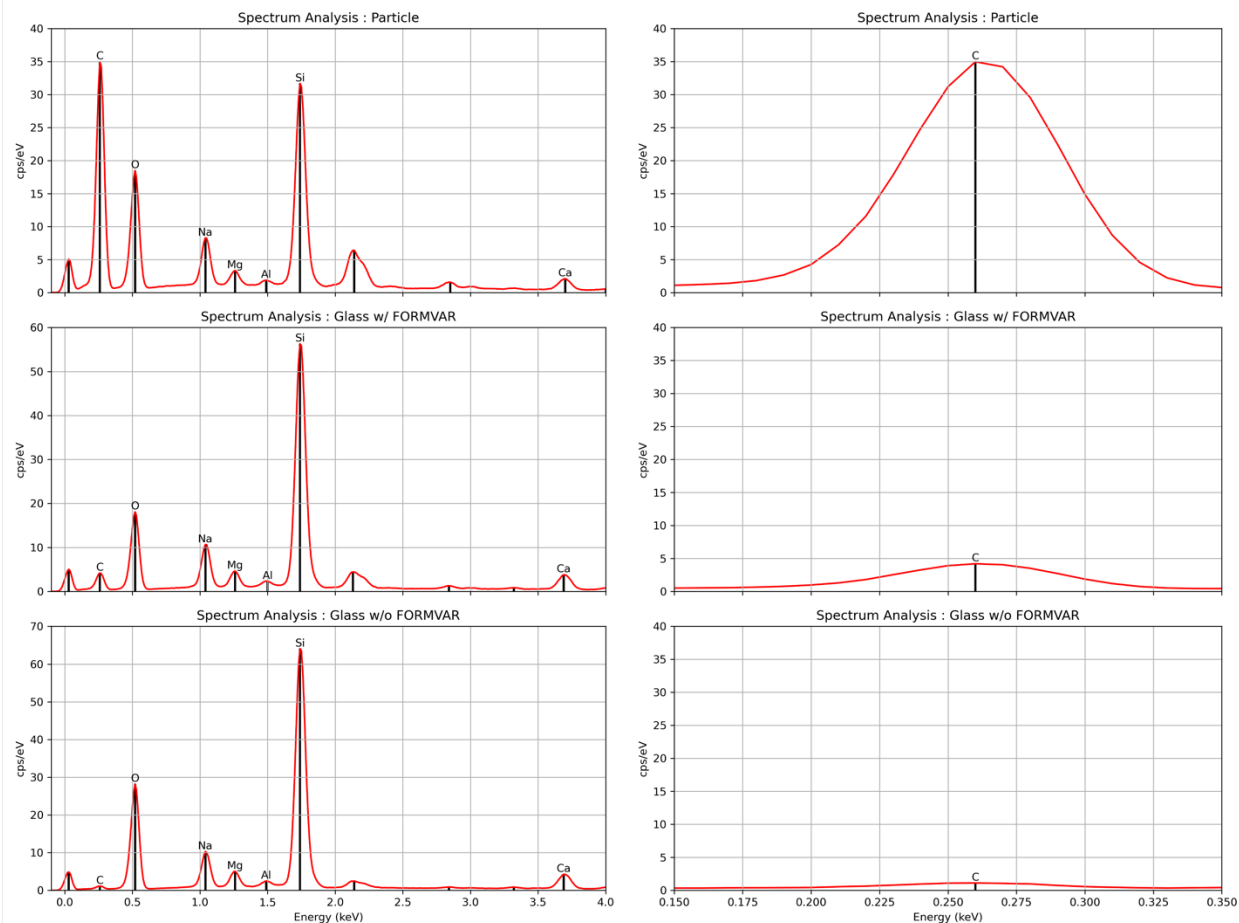


Figure 2.15: Panels (a), (c), and (e) display a single-point spectral analysis of a C-based particle with Formvar (a), a clear area with Formvar (c), and a clear area without Formvar (e). Each panel in the figure to the right (b, d, f) is the corresponding panel providing a closer view of the C peak. Due to Formvar's thickness and the results in this figure, the Formvar layer's impact on the C peak is considered negligible. The first peak, closest to 0 keV, is caused by noise from the EDS detector and can be ignored when analyzing the elemental composition of a particle, as it does not represent any actual element. The second spectral peak corresponds to gold (2.12 keV) and was excluded from the analysis since it was used for coating the sample.

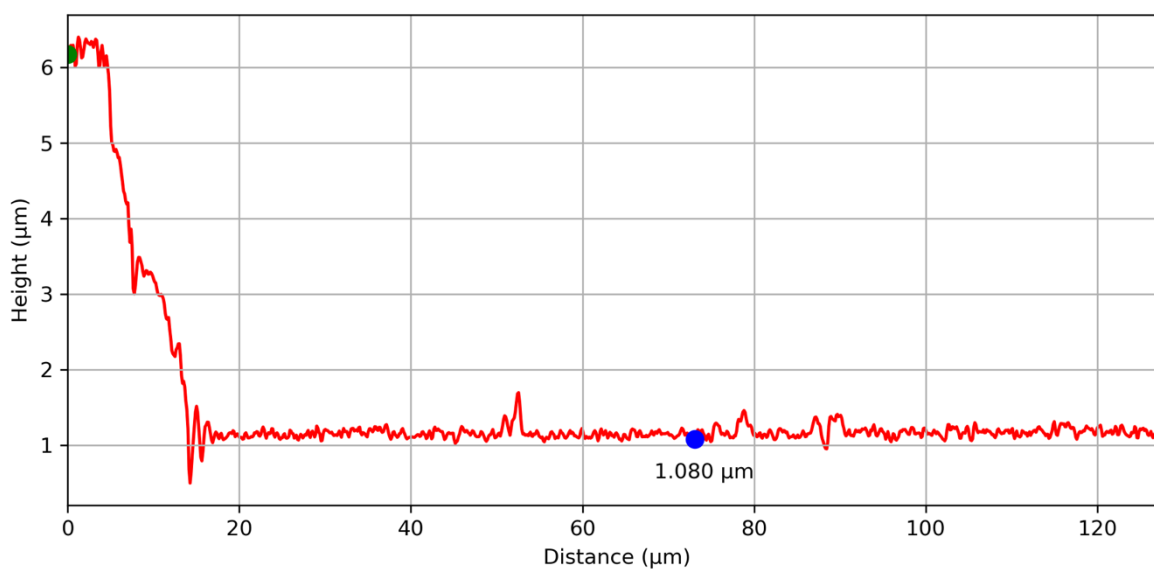
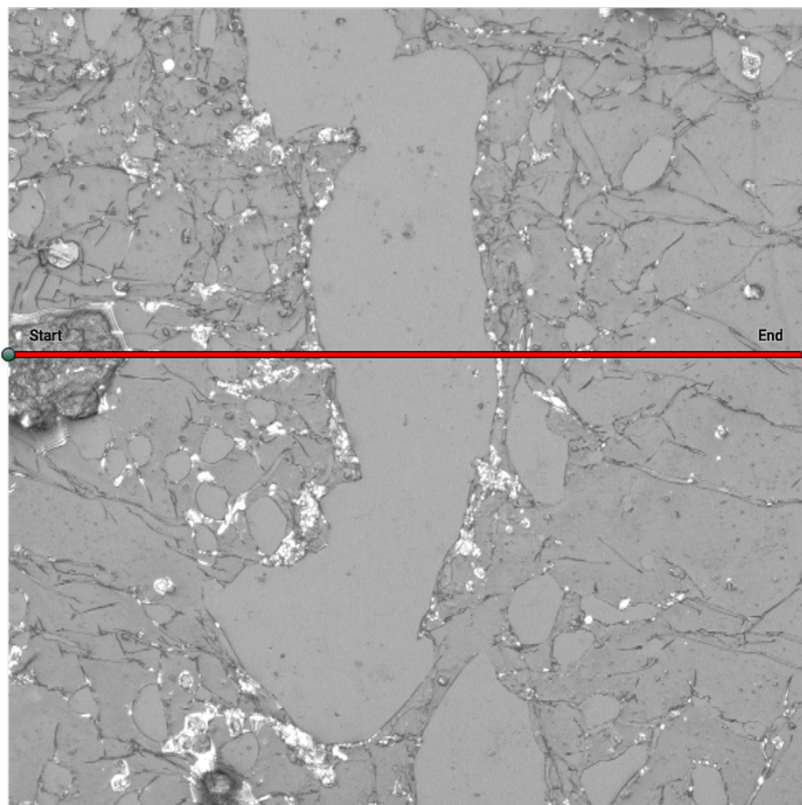


Figure 16A snapshot from the Olympus LEXT Analysis software of a sublimated ice sample with a Formvar coating. Panel (a) shows the 2-D CLSM laser imagery, with the red line indicating the transect through an area with and without the coating. Panel (b) shows the height (y axis in μm) across that transect (x axis in μm) for calculating the Formvar thickness (as seen along the blue segment), plotting the height used for Formvar's thickness calculation shown with the blue dot.

Chapter 3

Physical-chemical properties of
particles in hailstones from Central
Argentina

3.1 Preface

Falling hailstones are some of the most destructive natural phenomena in convectively active regions of the world, with significant global impacts on agriculture, infrastructure, and local economies. In the U.S. alone, hailstorm damage has exceeded \$1 billion annually since 1949 (Changnon 2008; Sander et al. 2013; Allen et al. 2017; Kumjian et al. 2019a), with three billion-dollar hailstorm events recorded in 2018 (Mahoney 2020). Climate change is expected to exacerbate these impacts by increasing hailstone size despite a potential reduction in hailstorm frequency, leading to greater severity and economic consequences (Raupach et al. 2021b). Furthermore, spatial variability in trends, such as increases in hail severity in Europe and Australia versus decreases in North America and East Asia, highlights the need for region-specific studies to better understand these dynamics (Raupach et al., 2021).

Studies have explored how environmental factors affect hail production in deep convective storms through high-resolution modeling (e.g., Kumjian and Lombardo 2020) and using global inferences of hail occurrence through satellite-based proxies (Cecil and Blankenship 2012; Ni et al. 2017; Bang and Cecil 2019; Bruick et al. 2019); however, they often are not verified against hail observations. Even when operational radar data is available with accompanying hail reports, accurately estimating hail sizes from these observations remains challenging (e.g., Murillo and Homeyer 2019). Much remains unknown about the processes leading to hail growth and environmental controls on hail occurrence and size, particularly outside of the United States (Allen et al. 2020). Furthermore, as climate variability and a warming Earth system influence hail

occurrence and intensity, understanding these microphysical processes becomes vital for accurate climate modeling and assessing future hydrological cycles (Allen et al., 2020).

Ice nucleating particles (INP) are a subset of environmental aerosols that facilitate ice formation through heterogeneous freezing owing to the assistance of a non-soluble particle such as mineral dust derived from surface sediments, biological material (e.g., pollen, bacteria, fungal spores, and plankton), and volcanic ash (e.g., Lamb and Verlinde 2011; Vali et al. 2015). While a range of aerosol types can serve as INP (Lamb and Verlinde 2011; Zhao et al. 2019; Burrows et al. 2022), various factors affect particles' ice-nucleating capabilities, including their size, surface topography, and composition including coating (e.g., Holden et al. 2021; Gao et al. 2022). The relationship between particle size and its ability to serve as an INP is complex and depends on multiple factors, including temperature, composition, and surface properties. Larger particles ($>10 \mu\text{m}$) generally exhibit higher ice-nucleating efficiency per unit mass because they provide greater surface area and can host diverse mineral or organic phases that promote ice formation (Kiselev et al. 2017). However, smaller particles ($<1 \mu\text{m}$) can dominate ice nucleation at colder temperatures or in environments rich in biological materials. Submicron INPs, such as bacterial fragments or fungal spores, are highly effective ice nucleators even at relatively warm temperatures (-10°C to -15°C), while fine mineral fragments like K-feldspar or quartz nanoparticles are efficient at colder temperatures (-20°C to -30°C) (DeMott et al. 2016; Chen et al. 2021; Beal et al. 2021). Even less is known about the types and concentrations of aerosols involved in hail formation, as the complexity of deep convective storm microphysics, limited observations, and the shortcomings of current models contribute to the inconclusive understanding of the effects of INP on hail formation and growth.

Studies of collected hailstones around the world have provided some insight into potential INPs involved in hail formation. Michaud et al. (2014) found biological ice nuclei in hailstone embryos in the U.S. Rocky Mountains, while hailstones collected in Slovenia (Šantl-Temkiv et al. 2013) and the triple border region of Paraná, Brazil, and Argentina (Beal et al. 2021) noted signatures of the respective regions' soil. Other studies point to anthropogenic markers through the presence of microplastics (Kozjek et al. 2023), highlighting the implications of human activity on hail formation. In studying INPs, the historical focus on particles $\leq 10 \mu\text{m}$ primarily reflects technical limitations rather than theoretical constraints. Early detection methods, such as continuous flow diffusion chambers, employed size-selective impactors to avoid optical misclassification of ice crystals and aerosols, systematically excluding super-micron particles from analysis (Cziczo et al. 2009; DeMott et al. 2010). Practical modeling considerations compounded this instrumental bias, as sub-10 μm particles dominated atmospheric datasets due to their higher abundance and slower sedimentation rates, leading to parameterizations skewed toward smaller sizes (DeMott et al. 2016). Recent advancements in microfluidic arrays now enable the investigation of super-micron INPs, revealing their previously underestimated role in processes like hail embryo formation (Tarn et al. 2018). The analysis techniques in studies like (Šantl-Temkiv et al. (2013), Michaud et al. (2014), Beal et al. (2021), all required melting the hailstones, removing information on non-soluble particle size distribution or composition with respect to the hailstone embryo and neglecting soluble particles. This present work, using a novel hailstone particle analysis method (Bernal Ayala et al. 2024a), adds to the limited literature on hailstones' composition through analysis of individual non-soluble particles contained within hailstones collected in Central Argentina, a global hotspot for hail.

Córdoba Province in Argentina has some of the most intense storms in the world (Zipser et al. 2006) and experiences frequent hail (e.g., Cecil and Blankenship 2012; Rasmussen et al. 2014) that has destructive impacts on property and agriculture. As such, this region has been the focal point of recent field campaigns collecting data on these severe storms, including the 2018-19 Cloud, Aerosol, and Complex Terrain Interactions (CACTI; Varble et al. 2021) and 2018 Remote Sensing of Electrification, Lightning, and Mesoscale/Microscale Processes with Adaptive Ground Observations (RELAMPAGO; Nesbitt et al. 2021) near the Sierras de Córdoba (SDC; Figure 3.1), a mesoscale mountain range that runs parallel to the Andes in northwest Argentina. A 7-month (austral spring to mid-autumn) survey of CACTI INP measurements (Testa et al. 2021) found that diverse plant communities in nearby areas likely release high amounts of biological and organic particles. Additionally, intensively farmed plains are identified as a significant source of soil dust from post-harvest to late spring, with a combination of bio-particles released by plants and soil dust when crops start growing thus contributing to INP concentrations during this time of year. This CACTI study did not focus on hailstorms, although it is therefore reasonable to hypothesize that hailstones collected in this region would contain particles containing imprints of both biological and agricultural activity.

To explore the influence of particle identity and availability on hailstone formation, microscopy techniques can be applied to the individual non-soluble particles using the new method described in Bernal Ayala et al. (2024). Studies over the past two decades (e.g., Sokolik and Toon 1999; Tegen and Lacis 1996; Claquin et al. 1999; Sokolik and Toon 1996; Kandler et al. 2007; Nousiainen et al. 2009; Jeong et al. 2014; Kemppinen et al. 2015; Li and Sokolik 2018; Conny et al. 2019; Huang et al. 2020; Di Biagio et al. 2020) have used Scanning Electron Microscopy (SEM)

with Energy-Dispersive X-ray Spectroscopy (EDS) to identify and quantify the mineral phases present in dust aerosols. Much of this work has focused on dust samples from desert regions like Asia and the Sahara, identifying key mineral phases including quartz, calcite, halite, and hematite (Jeong and Nousiainen 2014; Schütz and Sebert 1987). The mineralogical complexity of dust particles is further compounded by amorphous silica, particularly in Saharan dust, often associated with clay minerals (Jeong et al. 2016). These findings provide a valuable reference framework for interpreting EDS spectra and identifying potential mineral phases in dust samples. However, to fully understand the role of these particles in ice nucleation, it is necessary to investigate their mineralogical composition, physical characteristics, and other factors, including agglomeration of multiple particle types. Previous studies suggest that organic-rich soil dust more efficiently serves as INP than mineral desert dust (Conen et al. 2011; Steinke et al. 2016; Cornwell et al. 2024), but how much of this enhancement is owing to the presence of organic coatings and biological material remains unclear. With agricultural soil dust and biological particles likely being primary aerosol sources available for hail formation in Central Argentina (e.g., Testa et al. 2021), it is crucial to explore the mineral composition of individual particles to understand potential INP sources for hailstone formation.

This study uniquely studies the physical and chemical properties of non-soluble particles retaining their position within each hailstone layer for two hailstorms of varying modes in Central Argentina. The overall motivation of this work is to provide insight into which non-soluble particles were likely involved in the initial stages of ice nucleation, and thus hail formation and subsequent growth, as well as their potential source regions. The specific objectives of this study are to (1) characterize the distribution and size of non-soluble particles trapped in both hailstone samples,

(2) identify the elemental composition distribution of individual non-soluble particles collected by each hailstone during its growth in the cloud, and (3) determine possible source regions of non-soluble particles identified in the hailstones. Section 2 describes the datasets and methods used to address these objectives. Section 3 describes the physicochemical characterization of non-soluble particles found in the hailstone sample. Section 4 discusses the results in the context of previous work and the implications of those results.

3.2 Data and Methods

3.2.1 Hailstone Collection and Preparation

The hailstones used for this analysis were collected during two hail events: 8 February 2018 and 13-14 December 2018; the later occurring during the RELAMPAGO-CACTI observation period. More specifically, the 4-cm hailstone from 8 February (hereafter referred to as V-7) was collected in Villa Carlos Paz, Córdoba, Argentina (lime-green star in Figure 3.1), and the 8-cm hailstone from 14 December (NG-1) was collected in Villa del Dique, Córdoba, Argentina (blue star in Figure 3.1). These collections were facilitated through Lucia E. Arena at the Facultad de Matemática, Astronomía, Física y Computación at the Universidad Nacional de Córdoba (FAMAF-UNC) and the citizen science Cosecheros Program (Arena and Crespo 2019; Arena 2022).

Following collection, each hailstone was immediately placed in a nylon bag within a thermally reinforced cooler maintained at -15°C and assigned a unique alphanumeric identifier incorporating the collector's name. Upon arrival at FAMAF-UNC's subzero facility (Laura Levi Atmospheric Physics Laboratory), the hailstone surface was carefully brushed to remove potential contamination before being transferred to a cold chamber at $-12 \pm 2^{\circ}\text{C}$ for processing. At this stage, a novel approach to preserve non-soluble particles within hail layers was implemented (Arena 2024; Bernal Ayala et al. 2024b). Hailstone samples were attached to a glass base and then cut over the equatorial symmetric plane using a diamond-embedded cutting disk. After cutting the hailstone to expose the embryo, the sample was evenly polished with a microtome to provide a thin, even ice layer over the embryo. At this stage, pictures were taken to record the location of growth rings relative to the embryo. Immediately after, 1% polyvinyl formal (Formvar) solution diluted in ethylene dichloride was applied with a glass rod over the flat polished surface and left to curate for a few minutes. Once covered with the Formvar solution, the hailstone was left in a sealed low-humidity container with silica gel at -12°C to sublimate. Once the ice sublimated, the particles trapped in the Formvar could be analyzed using light and electron microscopy at room temperature while preserving their location with respect to the hail embryo. Unlike traditional melting methods, which would dissolve soluble particles, our sublimation approach potentially preserves both soluble and non-soluble particles, though this study focuses on characterizing non-soluble particles. More details on these hailstone collection and preparation procedures are provided in Bernal Ayala et al. (2024).

3.2.2 Microscopy analysis

With particles and their locations with respect to the embryo preserved in Formvar, this method then allows for the application of microscopy techniques to provide information on the physical and chemical characteristics of non-soluble particles within hailstones. Using an OLYMPUS LEXT OLS4000 Confocal Laser Scanning Microscope (CLSM), a 2-D cross-section of each of the V-7 and NG-1 hail samples (Figure 3.2 and Figure 3.3, respectively) was created by identifying the embryo and using it as a reference point for scanning regions within and around it. For these two cases, the embryo is identified as the original nucleus through its uniform crystallographic structure under polarized light, contrasting with the radially aligned outer layers (Grenier and Sadok Zair 1983; Takahashi 1987). The core's small, equiaxed ice grains share nearly identical c-axis orientations, indicating it formed from a single frozen droplet or graupel particle (Takahashi 1987). This uniformity distinguishes it from the outer shells, where elongated grains align radially outward due to wet accretion (water freezing onto the surface; Takahashi 1987). The radial alignment of c-axes in these layers points to concentric growth around the embryo, while the embryo's central position and structural simplicity confirm it as the starting point (Soderholm and Kumjian 2023). The transition from a single-oriented core to layered shells reflects the hailstone's formation sequence, where the embryo acts as the nucleation site for subsequent accretion (Soderholm and Kumjian 2023; Takahashi 1987). In the case of the 4-cm V-7 sample, the 2-D cross-section (Figure 3.2) covers the embryo (Sector 4, Sector 5) and outer layers in both directions from the embryo to the outer-most layers of the stone (Sectors 1- 3, Sectors 6- 8). Within this 2-D cross-section, individual sectors of equal size (i.e., labeled Sectors 1- 8 in V-7, Figure 3.2) were selected for higher magnification to identify individual particles quasi-randomly within each sector

with respect to the embryo. A similar approach was implemented for NG-1 (3.3); however, owing to the larger size of this stone (8-cm compared to the 4-cm size of V-7), a second CLSM sweep was required to examine the entire area encompassing the embryo. This additional sweep resulted in horizontally adjacent sectors (e.g., Sector 1, Sector 2) in the same vertical section that were then grouped under a similar layer number for analysis (e.g., in Figure 3.3, Sector 1 and Sector 2 represented the same layer of the stone and thus identified as "1" when analyzing particles in that area). These numbered layers cover the larger embryo (1-5) and a cross-section toward one end of the stone identified as the outer layers (6-10).

This approach provided particle size distribution and surface topographical information for 73 and 223 identified particles within the V-7 and NG-1 hailstones, respectively, including particles down to the technique-limited minimum size of 1 μm (Bernal Ayala et al. 2024). This lower limit is achievable due to the CLSM optical sectioning capability, pinhole aperture design, and high-resolution imaging, which allow for clear visualization of structures approaching the diffraction limit of light without breaking it. It is worth noting that this resolution differs from the SEM, which can achieve resolutions down to 50 nm due to its use of electrons rather than light, offering even finer detail for nanoscale structures. ProfilmOnline software was used to calculate particle size, which is determined as the maximum length along the x- and y-axes (Filmetrics 2017). The increase in particle numbers analyzed between the samples is attributed to the increased efficiency in the analysis, allowing for more particles to be examined in a similar amount of time.

The sublimated hailstone samples were then coated with gold (V-7) and gold and palladium (NG-1), the difference owing to the availability of pure gold during lab analysis times and subsequently

analyzed using a Zeiss Sigma field emission gun (FEG) SEM with an EDS X-Max 80 mm² detector. Secondary electron images were acquired at 15 kV and a working distance of approximately 8.5 mm; settings that dictated the clarity and detail of the imagery and allowed for the identification of heavy metals without disintegrating the non-soluble particles (Bernal Ayala et al. 2024). The 2-D elemental cross-sectional maps (Figures 2, 3) were used to locate the same particles observed in the CLSM to investigate the elemental composition of the same identified individual particles. To minimize interference from the sample substrate, EDS spectra were acquired for 120 seconds from the center of each particle using a single-point analysis technique. Particle-free areas of the glass were also measured using EDS to obtain a control spectrum from the coated glass substrate. While this single-point approach was more labor-intensive, it increased our ability to reduce noise and minimize spectral contamination from the glass substrate. Monte Carlo simulations conducted at 15 kV accelerating voltage showed that for particles smaller than 1.5 microns, some x-rays are emitted from the glass substrate, though this impact is minimized for particles down to 1 micron. To further ensure reliable results, we classified particles based on element identification rather than quantifying with weight percentage values, which helps account for potential variations in signal intensity across different regions of particles. Additional details on this process and considerations when choosing coating material and EDS analysis techniques are available in Bernal Ayala et al. (2024).

3.2.3 Elemental characterization

A unique feature of this technique is its capacity to link the elemental composition along with the size of individual particles with their location and proximity to the hailstone embryo. Due to these

particles' small size and complexity, EDS spectra were primarily used for element identification, focusing on the presence and relative abundance of key indicator elements to interpret particle identity. This approach was chosen instead of calculating quantitative elemental abundances from EDS measurements for several reasons.

First, the particles were covered by a $\sim 1\text{-}\mu\text{m}$ thick slightly varying layer of Formvar (a carbon-based material) and further coated with a 10-nm layer of either gold (Au) or a gold-palladium (Au-Pd) conductive coating. Additionally, the particles rested on a soda-lime glass substrate containing elements like silicon (Si), aluminum (Al), sodium (Na), calcium (Ca), potassium (K), and oxygen (O), which contributed to the X-ray signals. While we aimed for spectrum deconvolution to account for signatures from both the coating materials and the substrate (Bernal Ayala et al., 2024), we recognize further complications introduced by slight spatial variations in Formvar thickness and thus relied on elemental presence and relative abundance rather than absolute quantitative abundances for our particle classification.

To further justify our classification approach, we note that analyzing particles with irregular geometries presents additional challenges in trying to quantify abundances (Fletcher 2011; Goldstein et al. 2017). EDS is fundamentally designed for flat, homogeneous materials when applied to small, polyphase, or irregularly shaped particles. Complications arise due to assumptions in the matrix correction and irregularities in X-ray production, emission, and take-off angles to the detector that impact quantifying elemental abundances from the EDS spectrum. Additionally, the EDS spectrum represents all X-rays produced within an approximate $2\text{-}4\ \mu\text{m}^3$ activation volume at the beam's impact location. Given that many aerosol dust particles (as an

example noted in Section 1) exhibit heterogeneity at the sub-micron scale, numerous EDS spectra will reflect polyphase materials.

For these reasons, we did not place high confidence in the absolute values of elemental weight percentages. Instead, EDS spectra were interpreted based on the presence of characteristic elements corresponding to specific mineral phases. More specifically, particles with high concentrations of carbon (C) and oxygen (O) were interpreted as organics, while others with a significant presence of nitrogen (N) were identified as nitrates. Lithic fragments were identified as pieces of eroded rock rich in Si, Al, Na, Ca, Mg, and Fe. Agglomerated carbon-lithic or carbon-lithic-clay fragments showed signatures rich in C, Si, Al, Na, Ca, Mg, and Fe, representing potential organic mixtures with dust and other particles in the region (referred to as agglomerated mineral/organics). An example of this agglomerated mineral/organics classification is shown in Figure 3.4a, characterized by strong Si, Al, Na, Ca, and Mg peaks in its EDS spectrum. The addition of CLSM, which provides information about particle color and general morphology, and SEM's high-resolution surface imaging with the EDS's elemental analysis allows for particle classification that considers both chemical composition and physical structure. Here (Figure 3.4a), the CLSM image reveals a bright, irregularly shaped particle against the dark background. In contrast, the corresponding SEM image shows its complex three-dimensional structure with multiple crystalline components, supporting its classification as an agglomerate.

The middle panel (Figure 3.4b) demonstrates a Fe-rich organic particle with dominant O and Fe signals. The CLSM image shows a reddish-brown coloration characteristic of Fe-rich particles, while the SEM reveals a smooth, folded surface with sharp-edge structures. This spectral and

morphological evidence combination supports its classification as a Fe-rich organic particle. The right panel (Figure 3.4c) reveals a salt particle with prominent Cl and Na peaks, characteristic of halite. The CLSM image shows a dark, well-defined particle. In contrast, the SEM image displays an irregular shape with uneven edges and lacks the symmetrical, straight-edge characteristics typically associated with cubic morphology, such as those found in halites. This elemental classification scheme also identified distinct minerals including quartz and calcite. We also detected particles containing unique indicator elements, such as groups of zinc chloride, copper zinc chloride, or copper chloride particles, with EDS spectra rich in Zn-Cl, Zn-Cu-Cl, or Cu-Cl, respectively.

3.2.4 Air Mass Trajectories

The NOAA Air Resources Laboratory's Hybrid Single-Particle Lagrangian Integrated Trajectory model (HYSPLIT; Stein et al. 2015) was first used to generate a 24-hour air mass back-trajectory using $0.28^\circ \times 0.28^\circ$ European Environment Agency Reanalysis datasets (ERA5; Hersbach et al. 2020) with a vertical resolution of 37 pressure levels: 25 hPa intervals from 1025 to 750 hPa, 50 hPa intervals from 750 to 300 hPa, and 25 hPa intervals from 275 to 100 hPa. Trajectories were initiated at 1700 UTC on 8 February and 2200 UTC on 13 December, with hourly intervals starting at heights of 100, 500, 1000, and 1500 m above ground level from convective core coordinates on 8 February (64.75°W , 31.59°S ; marked by a red star in Figure 3.1) and on 13-14 December (64.45°W , 32.20°S ; marked by a blue star in Figure 3.1). These initiation coordinates were identified using channel 11 ($8.4 \mu\text{m}$) from the geostationary satellite GOES-16 (Bernal Ayala et al. 2022).

These initiation height levels were chosen for the following reasons: 100 m is the lowest point to the surface and the first pressure level, 500 m and 1000 m provide boundary layer variability, and 1500 m focuses on possible particle transport influences from the low-level jet (Bernal Ayala et al. 2022; Sasaki et al. 2022). A trajectory matrix with a 7x5 grid and 0.30° spacing was also processed from the initial convective pixel coordinate at 1700 and 2200 UTC (on 8 February and 13-14 December, respectively) for five days to better understand which local and longer-range sources could have transported particles at the initiation location before hail-producing convection was observed. The area covered by all back-trajectories resulting from the matrix was divided into grid cells with dimensions of 0.28° longitude and 0.28° latitude (i.e., ERA-5 horizontal resolution). Each trajectory occurrence in each grid cell was then normalized based on the time spent over each grid cell and included trajectory endpoints for all the heights (e.g., Ashbaugh et al. 1985). Residence-time coefficient pixels were overlaid on the C3S Land Cover classification gridded map from 2023, as shown in Figure 3.1. This map provides a global description of the land surface divided into 22 classes, available through the C3S Climate Data Store and defined using the United Nations Food and Agriculture Organization's Land Cover Classification (Copernicus Climate Change Service 2019). This approach provides insight into the highest probability of specific land-use regions being possible source regions for the non-soluble particulates analyzed in this study.

3.3 Results

3.3.1 8 February 2018

On 8 February 2018, an isolated supercellular convective system developed east of the Sierras Grandes, located in the northern section of the SDC (lime green star; Figure 3.1). This convective system produced record-breaking gargantuan hail (Kumjian et al. 2020) in Villa Carlos Paz, in addition to the 4-cm hailstone collected and analyzed in this study (V-7). While a warm, humid, conditionally unstable airmass was present, supporting the initiation and growth of deep convection on this day (Kumjian et al. 2020), with a large-scale pattern similar to composites for supercell environments in this region (Mulholland et al. 2018), a northerly low-level jet, often linked to large-scale moisture transport (e.g., Sasaki et al. 2024) and deep, widespread convective systems in this region (e.g., Rasmussen and Houze 2016), was lacking during this case. This particular hail-producing storm, therefore, developed under more local influences, including strong upslope flow along the SDC (Bernal Ayala et al., 2022), that are likely to affect potential source regions of particles found within the V-7 hailstone from this case.

3.3.1.1 Particle Size and Elemental Composition of Individual Particles

This V-7 hailstone analyzed in this case included particles analyzed both in the embryo and outer layers through a vertical cross-section of the 4-cm stone (3.2). The CLSM analysis of V-7 revealed particle sizes ranging from 2 to 150 μm (Figure 3.5), with an average particle size of 30 μm . This

indicates that particle sizes vary, with many particles being much smaller or larger than the average particle size. The minimum size measured was 2 μm , close to the minimum observable particle size using this method (1 μm ; Bernal Ayala et al. 2024). When focusing on particles within the embryo (22 particles), sizes ranged from 6 to 150 μm . In contrast, the particles sampled in the outer layers (51 particles) were smaller over a narrower range, encompassing sizes from 2 to 122 μm . While the comparison between the embryo and outer layers in V-7 suggests that the embryo contained larger particles than the outer layers, a key point here is that both regions contained particles exceeding 100 μm .

With a large range of particle sizes identified in the hailstone, the elemental classification scheme described in Section 2.3 was applied to this hailstone sample to determine the compositions of these individual particles. Overall, the particles in V-7 were primarily characterized as agglomerated minerals/organics (~41%; Figure 3.6-A; Table 2) and distributed throughout the hailstone (Figure 3.7). The particle sizes in this category ranged from 6 to 75 μm in the embryo (9 particles) and 2 to 55 μm in the outer layers (21 particles).

The second most prevalent group was agglomerated salts (~16%; Figure 3.6-A; Table 2), characterized by strong Cl and Na signals in EDS analysis and distributed throughout the hailstone (Figure 3.7). The 10 particles in this category analyzed in the outer layers ranged from 5 to 122 μm in the outer layers. Of the 2 particles of this type sampled in the embryo, one was 13 μm while the other was the largest particle recorded in this group and in the entire V-7 sample at 150 μm . Interestingly, even though this large particle was identified as a salt, it did not support a large single crystal but an agglomeration of smaller crystals (not shown). Instead, this particle exhibited a

strong carbon peak, indicating a small salt particle atop a potential agglomerated mineral/organic particle.

At 8% frequency, Zn-Cl-rich particles (Figure 3.6-A; Table 2) consisted of Zn-Cl content greater than 1% by weight. A single particle of 33 μm was found in the embryo, while particles in the outer layers ranged from 7 to 25 μm (5 particles; Figure 3.7). Organic particles (~8%; Figure 3.6-A; Table 2), containing more than 60% weight of carbon and rich in oxygen, were found in both regions with sizes ranging from 22 to 33 μm in the embryo and 10 to 23 μm in the outer layers, with 3 particles in both regions (Figure 3.7). Similarly, at 8% frequency, clays (Figure 3.6-A; Table 2), characterized by high aluminum content and the presence of Si, K, Ca, Na, Mg, and Fe, were composed of two particles in the embryo of sizes 20 and 55 μm and 4 particles analyzed in the outer layers ranging from 4 to 47 μm .

Shifting to the larger-than-average particle sizes found in V-7 are quartz particles (~7%; Figure 3.6-A; Table 2), identified as silicon content greater than 30% by weight, with 2 particles analyzed in the embryo of sizes 16 and 22 μm , and 3 in the outer layers ranging 38 to 55 μm in size. Ammonia/nitrate particles (~7%; Figure 3.6-A; Table 2), which were nitrogen-rich with content greater than 7% by weight, included 3 particles in the embryo ranging in size from 37 to 58 μm and 2 in the outer layers (31 and 45 μm). Two Fe-oxides particles (~3%; Figure 3.6-A; Table 2), dominated by iron and oxygen with no carbon or silicon, were located in the outer layers of the hailstone with sizes of 33 and 92 μm (Figure 3.7). Although Fe-oxides were only detected in the outer layers in this particular swath, a second swath conducted in a different direction across the hailstone (not shown) identified Fe-oxide particles in the embryo as well. This trend for all particle

categories to be found throughout the whole sample extended to the final identified category, lithics (1%; Figure 3.6-A; Table 2), characterized by a silicon content of 20-40% weight, along with high concentrations of Na, Mg, and Ca, minor amounts of Al and K, and no detectable carbon from the Formvar. Only one particle, measuring 5 μm , was identified in this category and located in the hailstone sample's outer layer (Figure 3.7); however, the second swath (not shown) revealed additional lithic particles within the embryo.

By analyzing the elemental composition of individual particles within the hailstone, the dominance of large, agglomerated particles (including those with salt) in the sample suggests a link to local land use, including hypothesized agricultural and biological sources. While particles of up to 100 μm are likely to remain suspended in the atmosphere for up to 2 days (Jaenicke, 1978; Bakan et al., 1987), the largest of the particles observed within the V-7 hailstone (i.e., 150 μm agglomerated salt in the embryo) were likely ingested into the storm from local sources near the SDC. The HYSPLIT back trajectory analysis provides further insight into these links.

3.3.1.2: Possible Source Regions

The analysis of the 24-hour HYSPLIT back trajectory (3.8-A) provides information on the possible origins of the particles in the V-7 hailstone sample with distinct patterns at different altitude levels. Levels 100 and 500 m AGL show trajectories near the initiation point from the northwest but earlier in the 24-h period had curved over the northeastern part of the SDC, likely owing to the upslope flow of surface winds from the northeast (Bernal Ayala et al., 2022). This upslope flow is supported by the terrain and height change of the trajectory seen in Figure 3.8-A (bottom figure). The 1000

and 1500 m AGL trajectories came from the north and northwest near the initiation point but, moving back in time, showed a slight curvature north and northeast of the Cordoba Province at distances farther than the lower levels. Within this short time frame, the SDC will likely impact the particle sources found in the hailstone. However, longer range transport of particles prior to 24-h may also have deposited particles in the area that could have been ingested into the 8 February supercell.

To investigate potential source areas further back in time, the residence time coefficients calculated for the 5-day back-trajectory matrices (Figure 3.8-B) similarly highlight the regional influence indicated in the 24-h trajectories in that most trajectories lie within the Argentinean borders. More specifically, under the assumption that the particles arriving at the location where the hail-producing storm initiated are more likely emitted from regions where the air masses spent more time (Yadav et al. 2021; Ren et al. 2021; Testa et al. 2021) the grid cells showing the high residence-time coefficients (any grid that includes more than one HYSPLIT trajectory) are considered potentially principal sources for the particles found in the hailstone. The regions with the highest residence-time coefficients for 5-days leading up to the V-7 storm initiation (orange, yellow, and red in Figure 3.8-B) are generally located over the SDC, Córdoba City (white star in Figures 3.1, 3.8-B), Argentina's largest natural salt lake (Laguna Mar Chiquita; 30.71°S, 62.56°W), and Provinces such as Santiago del Estero, Chaco, Santa Fe, and Corrientes (see Figure 3.1 as a geographical reference). These results reveal that sources within Argentina's geographical limits account for possible non-soluble particle sources in the analyzed hailstone sample. More specifically, in comparing the high residence-time coefficient pixels from the 5-day back trajectory with the C3S Land Cover map (Figure 3.8-B), we find the most predominant land uses (Figure

3.8-C) corresponding to shrublands, croplands, mixed vegetation, urban areas (mostly Córdoba city), and areas with a body of water (including the aforementioned salt lake), consistent with the imprints of soil dust, organics, salt, and minerals found throughout the V-7 hailstone, including the embryo, and emphasizing the importance of local land use on INP sources of hail formation.

3.3.2 13-14 December 2018

It is not uncommon for hail-producing storms in Argentina to form from larger convective systems in environments characterized by air transport from non-local sources (e.g., Rasmussen and Houze 2016; Sasaki et al. 2022). Therefore, it is worthwhile to compare the V-7 hailstone with one collected in this type of environment to explore potential non-local sources on hail formation. The 8-cm NG-1 hailstone collected during the 13-14 December 2018 event was associated with a mesoscale convective system (MCS) that developed in the southern portion of the SDC (blue star; Figure 3.1). In contrast to the 8 February supercell case, this hail-producing MCS was associated with increased moisture from the South American Low-Level Jet (SALLJ), dry air subsidence east of the Andes capping the low-level moist layer, and lee cyclogenesis resulting from the passage of an upper-level trough (Bernal Ayala et al. 2022; Sasaki et al. 2022); all characteristics of environments favorable for MCSs in this region (Rasmussen and Houze 2016; Mulholland et al. 2018; Bruick et al. 2019; Sasaki et al. 2024). As such, particularly owing to the SALLJ's large-scale transport of air and likely associated particles from a farther distance, the hypothesis was that there would be different particle compositions in this stone compared to the 4-cm stone of 8 February (a supercell dominated by more local influences including strong upslope flow).

3.3.2.1 Particle Size and Elemental Composition of Individual Particles

For NG-1, particle size ranged from 1 to 256 μm (Figure 3.9), with an average particle size of 35 μm . The largest particle in NG-1 was ~ 100 μm larger than the largest in V-7, and the average particle size was also larger in NG-1 (35 μm) compared to V-7 (30 μm). This shows that both hailstone's particle sizes had large variations. When focusing on particles within the embryo (106 particles) and the outer layers (105 particles), large particles (i.e., > 100 μm) were found throughout the hailstone, with large size variability observed in both regions. Like V-7, the elemental classification scheme applied to NG-1 showed that the particles were primarily composed of agglomerated minerals/organics ($\sim 36\%$; 3.6-B; Table 2), with sizes ranging from 4 to 77 μm in the embryo (33 particles) and 9 to 109 μm in the outer layers (42 particles), and were similarly found throughout the NG-1 hailstone sample (Figure 3.10).

While one relatively small lithic particle was identified in V-7 (Table 2, Figure 3.6), lithics were the second most prevalent group in NG-1 ($\sim 22\%$; Figure 3.6-B; Table 2), with particle sizes ranging from 5 to 58 μm in the embryo (26 particles) and 8 to 181 μm in the outer layers (20 particles; Table 2), and were distributed throughout the hailstone (Figure 3.10). Organic particles were also more prevalent in NG-1 ($\sim 15\%$; Figure 3.6-B; Table 2) than in V-7 ($\sim 8\%$; Figure 3.6-A; Table 2). This category contained the largest particle size found in NG-1, ranging from 9 to 256 μm in the embryo (22 particles) and 13 to 216 μm in the outer layers, (10 particles), also distributed throughout the hailstone (Figure 3.10). Similar to V-7, quartz particles were found throughout the hailstone (Figure 3.10), with sizes ranging from 10 to 62 μm in the embryo (8 particles) and 3 to 69 μm in the outer layers (6 particles; Table 2) While less prevalent, ammonia/nitrate particles

were also detected in NG-1, ranging from 23 to 36 μm and found exclusively in the outer layers with 4 particles (Figure 3.10; Table 2).

Despite the consistency in particle elemental categories found within both hailstones, some categories were unique to NG-1. Cu-Zn-Cl-rich particles ($\sim 4\%$; Figure 3.6-B; Table 2), with particle sizes ranging from 6 to 78 μm , were exclusively located in the outer layers with 8 particles (Figure 3.10). A single Cu-Cl-rich particle ($\sim 1\%$; Figure 3.6-B; Table 2) measuring 32 μm was found in the outer layers (Figure 3.10). Two calcite particles ($\sim 2\%$; Figure 3.6-B; Table 2) showed size ranges of 12 and 24 μm in the embryo and 8 to 13 μm in the outer layers, with 2 particles in each region (Figure 3.10). Finally, a single brass particle ($\sim 1\%$; Figure 3.6-B; Table 2) measuring 1 μm , characterized by strong Cu and Zn signals in EDS analysis, was found in the outer layers (Figure 3.10).

Overall, while both hailstone samples showed similarities in certain categories such as quartz, nitrate particles, and Fe-oxides (with NG-1 showing particles of 21 μm in the embryo and 61 μm in the outer layers), there were notable differences in the presence and distribution of lithics, organics, Cu-Zn-Cl-rich, Cu-Cl-rich particles, brass, and calcite, as well as the presence of salts in V-7 but their absence in NG-1. Were these different particle compositions linked to different trajectories associated with these different storms, including more non-local sources on 13-14 December? To explore this question, the HYSPLIT trajectories are again analyzed for the 24-hour and 5-day time frames.

3.3.2.2: Possible Source Regions

The 24-hour HYSPLIT back trajectory analysis was applied to the 13-14 December case (Figure 3.11-A) to determine potential source regions of the particles found within the NG-1 hailstone sample. Nearest the initiation point, the trajectories originate from the west and northwest at all analyzed levels. In particular, trajectories curved around the northern section of the SDC, moving upslope along the western side of the southern section of SDC instead of the eastern side as on 8 February. The 1500 m AGL levels followed a similar path as the lower-level winds but started at regions farther north than the lower trajectories. This trajectory height and direction is likely linked to the SALLJ and thus could have led to more remote sources of particles over a longer time period.

Therefore, residence time coefficients for 5-day back-trajectories matrices were again calculated (Figure 3.11-B) to explore potential sources outside of Argentina's geographical limits. Unlike on 8 February, when the trajectories were primarily within Argentinian territories, on 13-14 December, air mass trajectories with high residence times also came from Paraguay and Brazil. Under the same aforementioned assumption that the particles arriving at the location where the hail-producing storm initiated are more likely emitted from regions where the air masses spent more time, the regions with the highest residence-time coefficients (orange, yellow, red and lighter shades of blue in Figure 3.11-B) were generally located northwest of the SDCs, in the boundary between Cordoba, the southwestern corner of La Rioja and San Luis Provinces (Figure 3.1) as well as in locations outside of Argentina. While the main land-use categories associated with the highest residence times are generally the same for both cases (i.e., Figures 3.7-C, 3.10-C), the distribution shifts on 13-14 December from pixels associated with shrublands to more pixels

associated with both cropland and mixed vegetation (Figure 3.11-B). The dominance of the cropland category again is consistent with the prevalence of agglomerated mineral/organics, but the trajectories from either the west side of the SDC or from regions north of Argentina could explain unique source regions to NG-1 resulting in particle elemental compositions not observed or more prevalent than in V-7 (e.g., lithics, Cu-Zn-Cl-rich, Cu-Cl-rich, brass, calcite). There were also low residence time pixels over the salt lake (Figure 3.11-B), potentially explaining why no salt was found in NG-1.

3.4 Discussion:

Our study presents the first analysis of the sizes, composition, and distribution of non-soluble particles in hailstones from storms in Argentina. Unlike previous studies that melted hailstones to evaluate their overall composition (Šantl-Temkiv et al. 2013; Michaud et al. 2014; Beal et al. 2021), our approach described in Bernal Ayala et al. 2024 preserves both the non-soluble particles and their in-situ locations within the hailstones. It uniquely allows for analysis of the elemental composition of individual particles, revealing elemental combinations that impact the ice nucleating ability of those particles.

Applying our method to two hailstone cases from different storm modes in Central Argentina revealed that the majority of particles in both hailstones are agglomerated minerals/organics, found both within the embryo and throughout the outer layers of the hailstones and exceeding 100 μm in size. The largest particle (256 μm in NG-1) was identified in the embryo with a relative abundance of carbon and oxygen. This relative composition abundance is consistent with the presence of

organic particles identified in hailstones in China (Wang et al. 2023), where they used SEM-EDS and machine learning to analyze non-soluble particles through a melting and filtering technique. However, our unique approach, which enables the analysis of individual particles, suggests that particle agglomeration in particular may have played a significant role in hail formation within our Central Argentina cases, whether through physical coagulation in turbulent updrafts, water-mediated agglomeration in mixed-phase regions, or surface modification through chemical coating (Wang et al. 2024; Michaud et al. 2014; Mokkaapati 2009). Indeed, with a link to cropland through our particle trajectory analysis and prior studies emphasizing the role of coated and aggregated mineral dust in ice nucleation (e.g., Steinke et al. 2016; Iturri et al. 2017; Cornwell et al. 2024), this work supports that agglomerated mineral dust particles, modified through atmospheric aging and coating processes, likely serve as efficient INP for hail formation.

The breakdown of particle sizes by type and location in Table 2 reveals several insights. First, while both hailstones contained agglomerated mineral/organic particles throughout, their size distributions differed between embryo and outer layers, with NG-1 showing larger sizes in outer layers (up to 109 μm) compared to V-7 (up to 55 μm). Second, certain particle types showed distinct location preferences; for instance, Cu-Zn-Cl rich and Cu-Cl rich particles were found in NG-1's outer layers, while agglomerated salts were present throughout V-7 but entirely absent in NG-1. These spatial patterns provide information about particle availability during different stages of hail formation. Third, while the largest particles in both hailstones were found in their respective embryos, their compositions differed markedly: an organic-rich particle (256 μm) in NG-1 versus an agglomerated salt particle (150 μm) in V-7. This compositional difference in the embryonic particles suggests distinct aerosol populations were available during initial ice formation in these

different storm types, potentially serving as INPs, and thus providing information about the types and sizes of particles available for ice nucleation in these storms (Pruppacher and Klett 1980; Heymsfield and Pflaum 1985). In contrast, particles found in the outer layers were likely collected during the hailstone's growth process, becoming trapped within each successive layer as the hailstone grew through various cloud regions (Rangno and Hobbs 1991). This distinction allows our study to characterize both the potential INP population present during hail initiation and the broader array of particles encountered during hailstone growth and development through the cloud.

Beyond the particle-specific characteristics revealed by our analysis method, our findings demonstrate broader connections to regional characteristics that align with previous studies. Similar relationships between hailstone composition and regional soil signatures have been observed in hailstones collected in Slovenia and the triple border region of Paraná, Brazil, and Argentina (Šantl-Temkiv et al. 2013; Beal et al. 2021), expanding beyond agricultural activities to other influences of local land cover. Their results are consistent with our findings that quartz, clays, and agglomerated mineral/organic particles were abundant in our hailstones, particularly associated with the highest residence times of trajectories over and near the SDC. These particle trajectories also showed a link to a nearby salt lake (Laguna Mar Chiquita) on 8 February, where the largest particle in V-7 was categorized as an agglomerate that contained salt. A recent modeling study of this lake emphasized that it is one of many that are shrinking, exposing dry lakebeds that present a source of Na-rich mineral dust (Borda et al. 2022). The presence of this large mineral-organic agglomerate with salt in the hailstone embryo and the potential link back to this shrinking salt lake emphasizes another anthropogenic source of potential INPs or non-soluble CCNs to consider in hail formation and growth.

This anthropogenic link is also suggested through elemental composition results from the NG-1 hailstone, particularly through the presence of Cu-Zn-Cl-rich (4%) and Cu-Cl-rich (1%) particles that were not observed in V-7. The trajectory analysis for NG-1 showed sources both within and outside Argentina under the general "croplands" category, suggesting these particles may originate from agricultural activities over a broader region. Specifically, the presence of Cu-Cl compounds suggests a potential link to agrochemicals like copper chloride, commonly used for pest control (Lewis et al. 2016). According to a market report, copper oxychloride is used globally as a fungicide for crop protection, including in Argentina (Manoj 2023). While natural sources cannot be ruled out, international databases (e.g., mindat.org) reveal several Cu-Cl evaporite minerals actively mined in the Chilean Atacama Desert, the correlation with cropland trajectories and agricultural regions supports an agrochemical origin for these particles.

Zinc-containing particles in both hailstones (Zn-Cl-rich in V-7 at 8% frequency; Cu-Zn-Cl-rich at 4% in NG-1) suggest consistent regional sources of zinc aerosols. While zinc is typically not found in significant atmospheric concentrations, several regional sources could explain its presence in our samples. Argentina's significant zinc production, particularly from the Aguilar Mine in Jujuy Province, which produced over 23,000 tons of zinc in 2017 (U.S. Geological Survey (USGS) 2019; International Trade Administration 2023), represents a potential source. Additionally, the agricultural sector's use of zinc-based fertilizers (e.g., ZINC 700 and Status ZN) for seed treatment in crops like fruit trees, vineyards, vegetables, rice, corn, and wheat (FMC Argentina; Rizobacter) aligns with our trajectory analysis over croplands. Natural sources may also contribute, as Ecanndrewsite (ZnTiO_3) and other ilmenite-group minerals have been identified in amphibolites from the SDC basement (Espeche and Lira 2022).

The Fe-oxide particles identified in both hailstones, while less prevalent (3% in V-7), likely originate from three potential sources in the region: natural processes, agricultural activities, and anthropogenic factors. The SDC range contributes through weathering and erosion of iron-rich formations, including metamorphosed iron ore in the Sierra de Comechingones containing magnetite, hematite, goethite, limonite, and siderite (Zaccarini et al. 2004). Agricultural areas around Córdoba may also contribute through naturally iron-rich soils and the use of iron-containing fertilizers (e.g., "Green Up"; Recuperar S.R.L.). These Fe-oxide particles throughout both hailstones, combined with their relatively large sizes (33-92 μm in V-7), suggest efficient transport and incorporation mechanisms during hail formation.

Understanding the origins of these minerals highlights the environmental impact of human activities, such as agricultural practices, and the natural contributions from surrounding geological features, like the SDC, on aerosol sources, including those involved in hail formation and growth. The presence of large agglomerated particles ($>100 \mu\text{m}$) in both hailstones, particularly in their embryos, suggests that these particles play a crucial role in hail initiation. Their composition, ranging from mineral-organic mixtures to metal-rich compounds, reflects the region's natural and anthropogenic sources. This study's findings emphasize the need to further explore aerosol sources' effects on hailstone growth and development with a global mindset to improve near- and long-term forecasting of these impacts.

3.5 Conclusion

Using a novel hailstone-analysis technique (Bernal Ayala et al. 2024), this study provides first-of-its-kind insights into the size distribution, composition, and potential sources of non-soluble particles within hailstones from South America. Unlike traditional melting methods, our approach uniquely preserves the spatial distribution of particles within hailstones, allowing us to analyze both potential INPs in the embryo and particles collected during growth in the outer layers. These hailstones were collected in central Argentina from different storm modes under various environmental conditions, offering an opportunity to investigate potential variability in particle source regions and characteristics within hailstones that could influence their formation and growth. Through this unique approach, we found:

- Analyzed particles ranged in size from 1 to 256 μm , with the largest particles in each hailstone found in its embryo and larger particle sizes for the larger of the two hailstones. While our method's minimum observable size of 1 μm means we cannot detect smaller particles that may serve as INPs, particularly at colder temperatures, our ability to analyze larger particles ($>10 \mu\text{m}$) provides crucial insights into a size range often excluded from traditional INP studies.
- Agglomerated mineral/organic particles dominated both hailstones' elemental composition, with an organic-rich particle being the largest (256 μm in NG-1 embryo), and were observed in all layers throughout the hailstones.

- Lithics and other particle types were found throughout both hailstones. The presence of similar particle characteristics in both embryos and outer layers provides valuable information about particle availability during both initiation and growth phases that would be lost in traditional melting methods.
- Contributions from agricultural practices and geological features were linked to hailstone formation. Both hailstones were associated with various regional land-use types, including shrublands, mixed vegetation, croplands, and urban areas. The particles found contained regional soil signatures, potentially influenced by agrochemicals used in pest control practices or crop fertilizers, as well as sodium-rich mineral dust from nearby dry lakebeds.

These findings enhance our understanding of the interplay between atmospheric particle sources, both natural and anthropogenic, and their role in hailstone formation by linking the composition of particles within the hailstone embryo to local and regional land use. The value of our method lies not just in comparing embryo and outer layer compositions but in providing unprecedented spatial resolution of particle distributions throughout the hailstone. This preservation of spatial relationships enables several key insights impossible with traditional melting techniques: (1) evidence that large particles ($>100\ \mu\text{m}$) are present in embryos, challenging assumptions about size limitations in hail initiation, (2) characterization of particle size spectra across different regions, and (3) detailed analysis of individual particle characteristics in their original context.

The relationship between particle size and its ability to serve as an INP is complex and depends on multiple factors, including temperature, composition, and surface properties. While smaller

particles ($<1 \mu\text{m}$) can dominate ice nucleation at colder temperatures, larger particles ($>10 \mu\text{m}$) generally exhibit higher ice-nucleating efficiency per unit mass because they provide greater surface area and can host diverse mineral or organic phases that promote ice formation (Kiselev et al. 2017). This aligns with our findings of large particles in hailstone embryos, representing the population of particles available during initial ice nucleation. In contrast, particles in outer layers were likely collected during subsequent growth phases.

The predominance of large particles in hailstone embryos has significant implications for understanding hail formation. These coarse particles likely remained suspended for extended periods in convective updrafts due to turbulent mixing, allowing them to aggregate with smaller aerosols and form composite INPs with enhanced nucleation activity (Testa et al., 2021). While our method suggests the role of large particles in hail embryo formation, integrating complementary techniques to detect submicron INPs would provide a more comprehensive understanding of the full spectrum of ice-nucleating processes. The similarities observed between the two hailstones studied suggest that the composition and size of aerosols, key inputs in hail formation and growth models, are crucial for accurate simulations. However, the larger NG-1 hailstone displayed a greater diversity and number of particles, indicating potential differences in particle accumulation and transport processes, likely influenced by varying storm modes.

This study contributes to ongoing hail research and highlights the potential impact of natural and human activities on hail growth. One technical limitation of our approach includes challenges in carbon characterization using EDS. Carbon contamination within the SEM chambers can result in low-level carbon detection across all EDS spectra. Moreover, EDS is less sensitive to light

elements such as C. Our analysis confirmed that the contribution of carbon from the 1 μm Formvar coating is minimal, as demonstrated through comparison of potential carbon signals in clear glass sections with and without Formvar (Bernal Ayala et al., 2024). Additionally, while the glass substrate elements (Si, Al, Na, Ca, K, O) contribute to X-ray signals, our spectrum deconvolution approach allows us to account for these contributions in our particle classification. However, the EDS detector cannot differentiate the bonding environment of the carbon, making it impossible to determine if the carbon originates from inorganic sources (e.g., graphite), organic matter (e.g., detritus or pollen), or industrial materials (e.g., soot).

Despite these limitations, the techniques used in our research provide valuable insights into hail formation processes that complement existing methods. Similar particle characteristics in both stones suggest that initial conditions for ice nucleation may persist throughout the growth process, a finding only possible through spatial preservation. Future studies can apply this technique to hailstone samples from different regions globally to investigate whether similar particle characteristics are observed elsewhere. Such research, particularly when combined with complementary analytical methods, will enhance our understanding of hail formation mechanisms and help refine predictive models. As we continue to improve modeling efforts, incorporating diverse aerosol compositions and sizes will be crucial for enhancing the accuracy of forecasts related to hail events.

3.6 Figures

Table 2: Particle size ranges for each elemental category identified in hailstone samples V-7 and NG-1.

Category	Particle size range (μm)			
	V-7		NG-1	
	Embryo	Outer Layer	Embryo	Outer Layer
Agglomerated Min/Org	6 - 75	2 - 55	4 - 77	9 - 109
Ammonia/ Nitrate	37 - 58	31, 45	No particles	23 - 36
Brass	No particles		No particles	1
Calcite	No particles		12, 24	8, 13
Clays	20, 55	4 - 47	No particles	
Cu-Cl rich	No particles		No particles	32
Cu-Zn-Cl rich	No particles		No particles	6 - 78
Fe-oxide	No particles	33, 92	21	61
Lithics		5	5 - 58	8 - 181
Organics	22 - 33	10 - 23	9 - 256	13 - 216
Quartz	16, 22	38 - 55	10 - 62	3 - 69
Agglomerated Salts	13, 150	5 - 122	No particles	
Zn-Cl rich	33	7 - 25	9 - 34	3
Cu-Zn-Fe rich	No particles		No particles	27

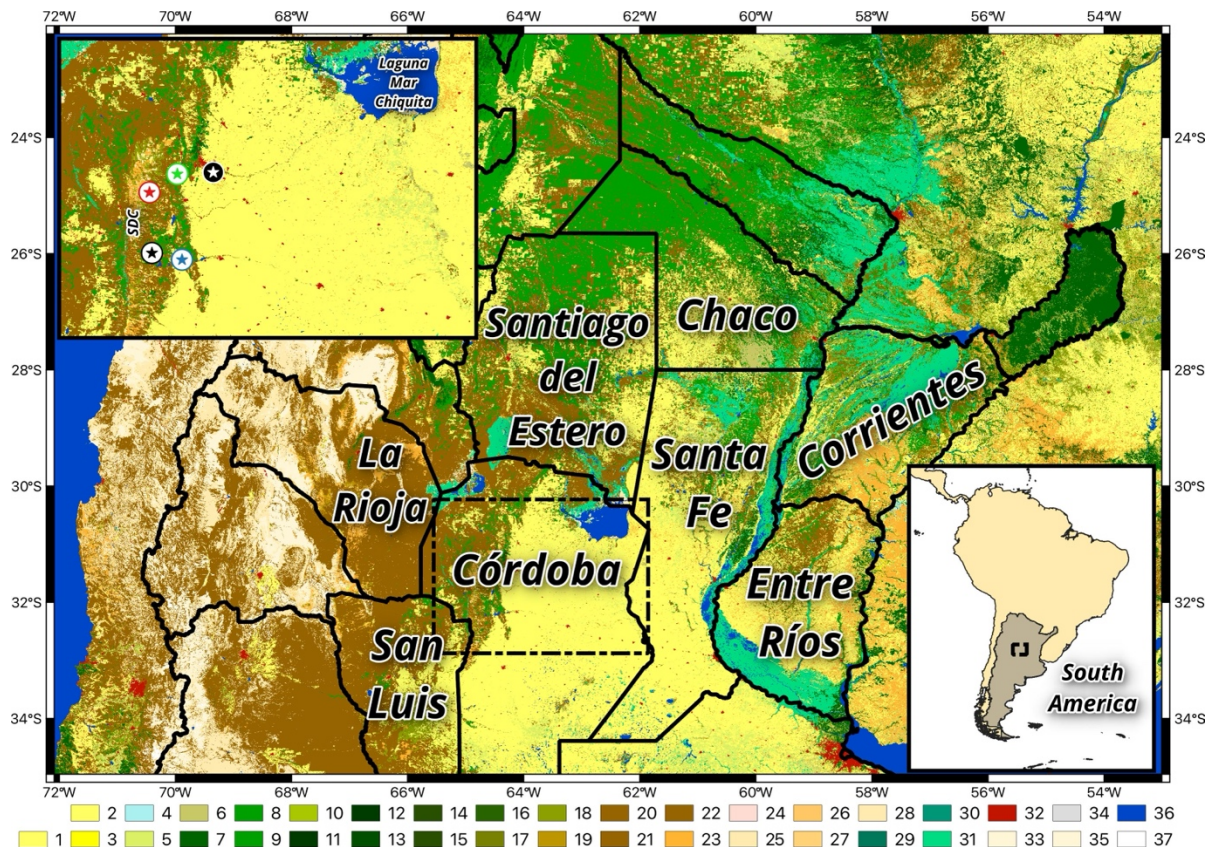


Figure 3.17: Map of northern Argentina covering an area shown in the black box in the lower right panel, including the Córdoba study area and nearby provinces. Within the dashed box covering northern Córdoba province is an inset (top left) highlighting Córdoba City to the east of the Sierras de Córdoba (SDC) and points of interest for this analysis: the site of the CACTI experiment observations in Villa Yacanto (black star), the hail collection locations: Villa Carlos Paz, Villa del Dique (lime green and blue stars, respectively), and the initiation point for air mass back trajectory run for 8 February and 13-14 December (red and blue star, respectively). Color fill represents the C3S Land Cover map available through the C3S Climate Data Store (CDS): 1-cropland rainfed, 2-cropland rainfed, 3-cropland rainfed tree or shrub cover, 4-cropland irrigated, 5-mosaic cropland, 6-mosaic natural vegetation, 6-tree broadleaved evergreen closed to open, 7-tree broadleaved deciduous closed to open, 8-tree broadleaved deciduous closed, 9-tree broadleaved deciduous open, 10-tree needleleaved evergreen closed to open, 11-tree needleleaved evergreen closed, 12-tree needleleaved evergreen open, 13-tree needleleaved deciduous closed to open, 14-tree needleleaved deciduous closed, 15-tree needleleaved deciduous open, 16-tree mixed, 17-mosaic tree and shrub, 18-mosaic herbaceous, 19-shrubland, 20-shrubland evergreen, 21-shrubland deciduous, 22-grassland, 23-lichens and mosses, 24-sparse vegetation, 25-sparse tree, 26-sparse shrub, 27-sparse herbaceous, 28-tree cover flooded fresh or brackish water, 29-tree cover flooded saline water, 30-shrub or herbaceous cover flooded, 31-urban, 32-bare areas, 33-bare areas consolidated, 34-bare areas unconsolidated, 35-water, 36-snow and ice.

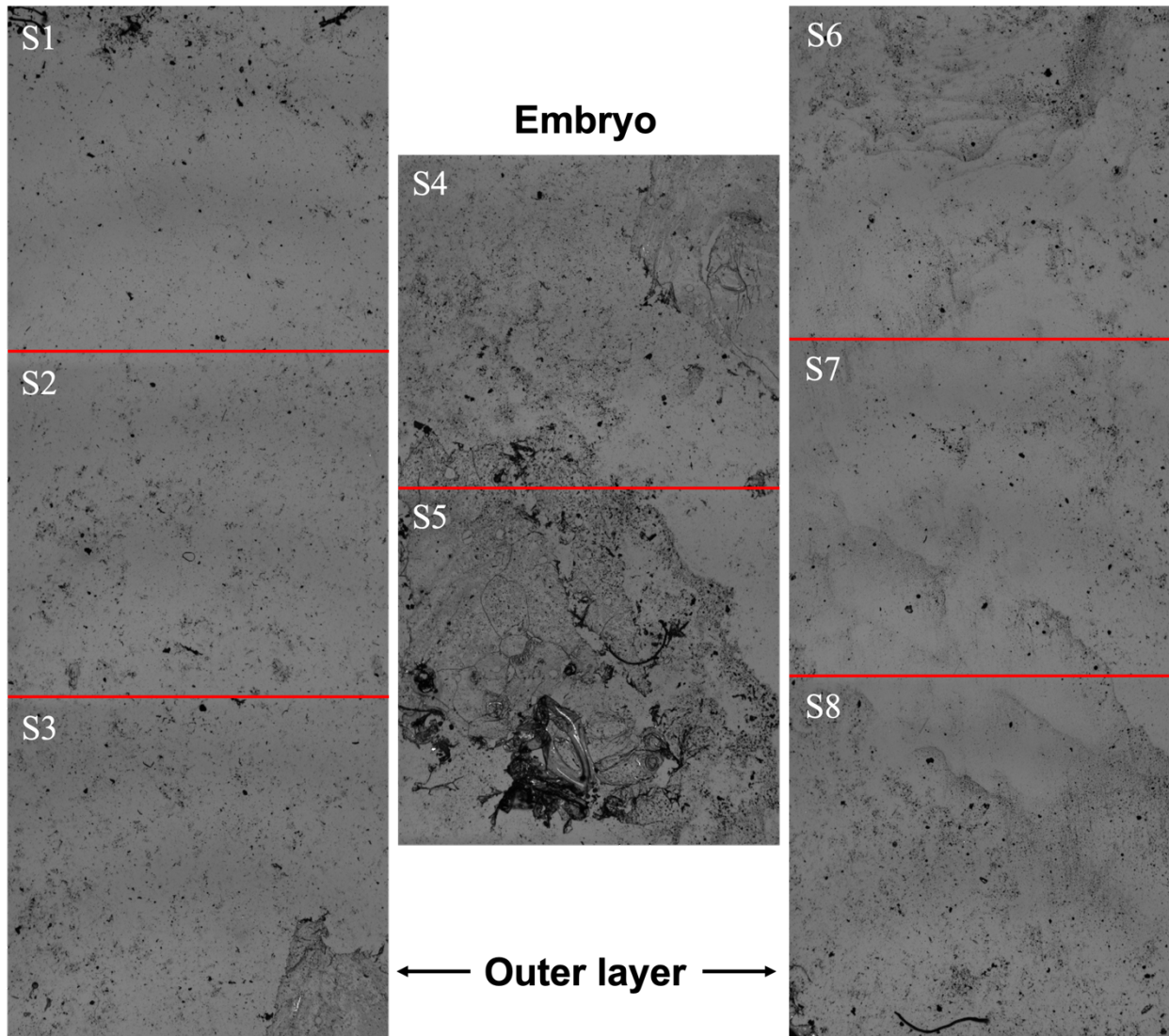


Figure 18: 2-D cross-section along an axis in the equatorial plane at 108x magnification for sample V-7 collected on 8 February 2018. Sectors (S) 4 and 5 indicate the embryo, while S1-S3, S6-S8 represent the outer layers.

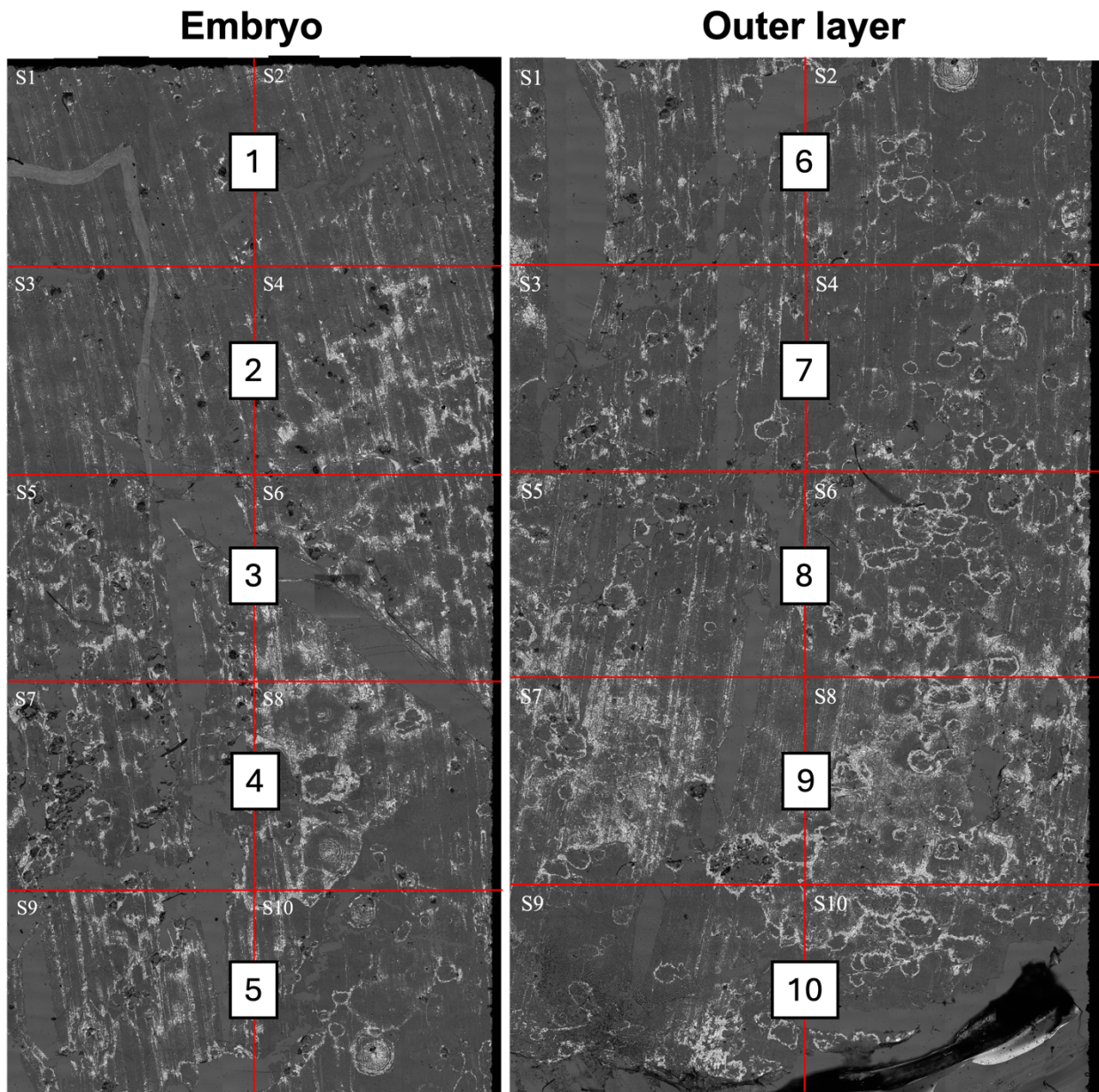


Figure 19: As in Figure 2, but for NG-1 collected on 13-14 December 2018. Sectors are grouped by layers relative to the embryo (layers 1-5) and outer layer (6-10).

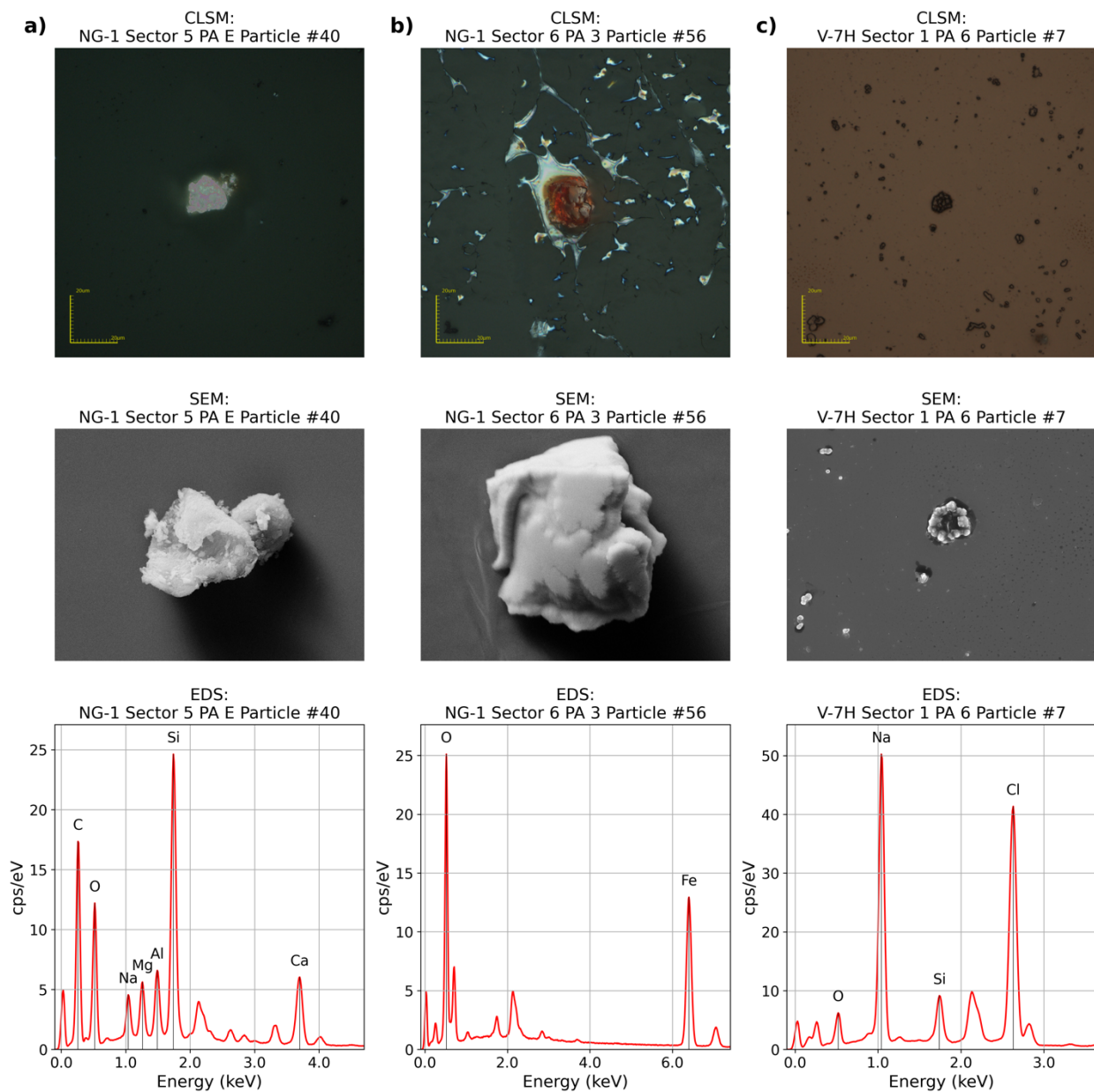


Figure 20: Examples of particles analyzed using three complementary techniques: Confocal Laser Scanning Microscopy (CLSM, top row), Scanning Electron Microscopy (SEM, middle row), and Energy-Dispersive X-ray Spectroscopy (EDS, bottom row). Left column shows an agglomerated mineral/organic particle. Middle column displays a Fe-rich organic particle. Right column shows a salt particle from V-7H Sector 1, with prominent Na and Cl peaks characteristic of halite. The CLSM images provide optical characteristics and context within the hailstone, while SEM reveals detailed surface morphology and EDS spectra confirm elemental composition. Scale bars in CLSM images represent 20 μm .

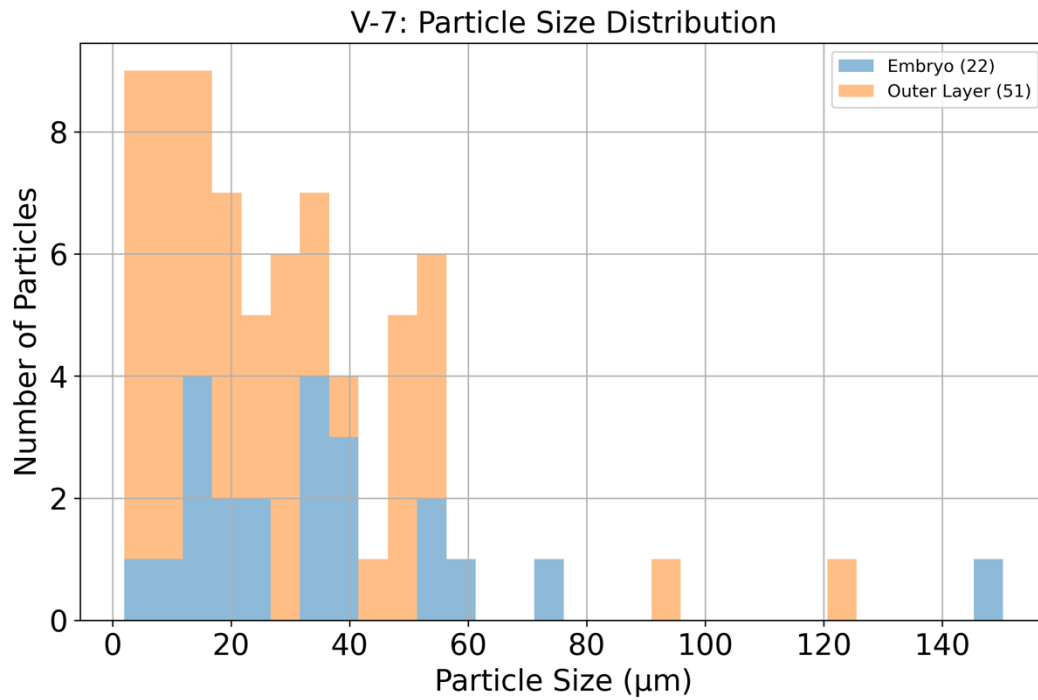


Figure 21: Particle size distribution in μm through the V-7 cross-section is shown in Figure 2, where the particle size distribution in the hailstone embryo region is represented by blue pastel bars, and the particle size distribution in the outer layers of the hailstone is shown by orange pastel bars.

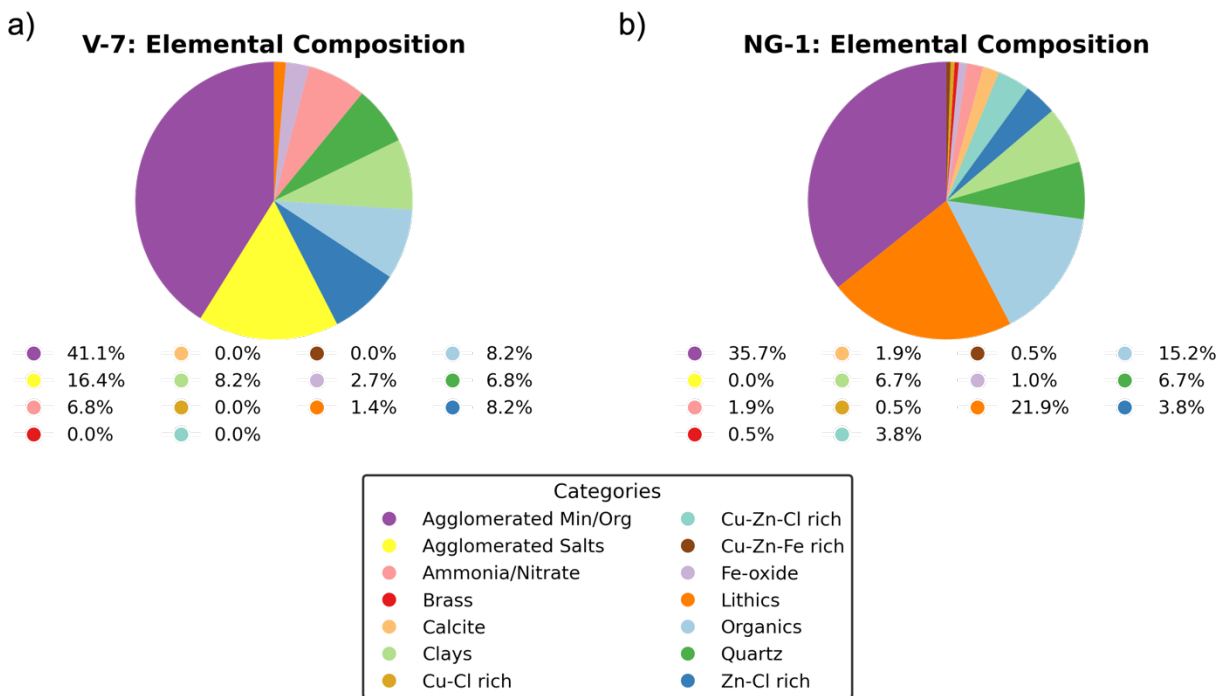


Figure 22: Elemental composition distributions for particles selected within the 2-D cross sections for a) V-7 and b) NG-1.

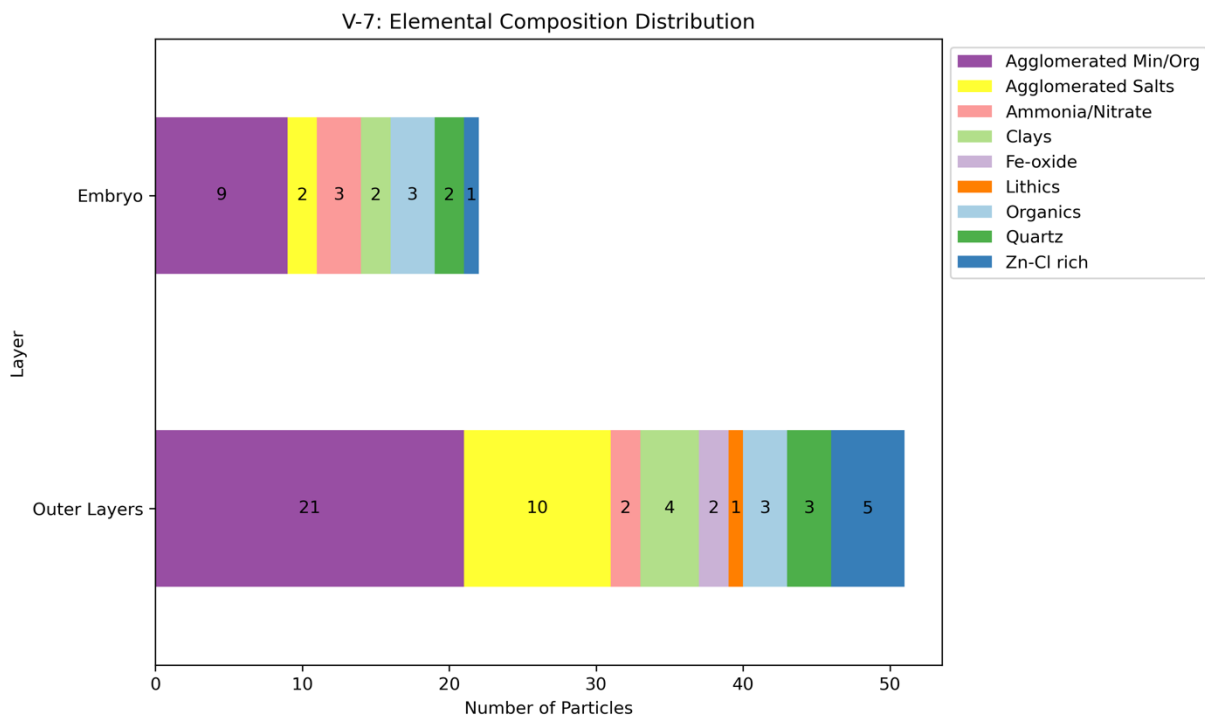


Figure 23: Elemental composition distribution for particles identified in the V-7 cross-section shown in Figure 2.

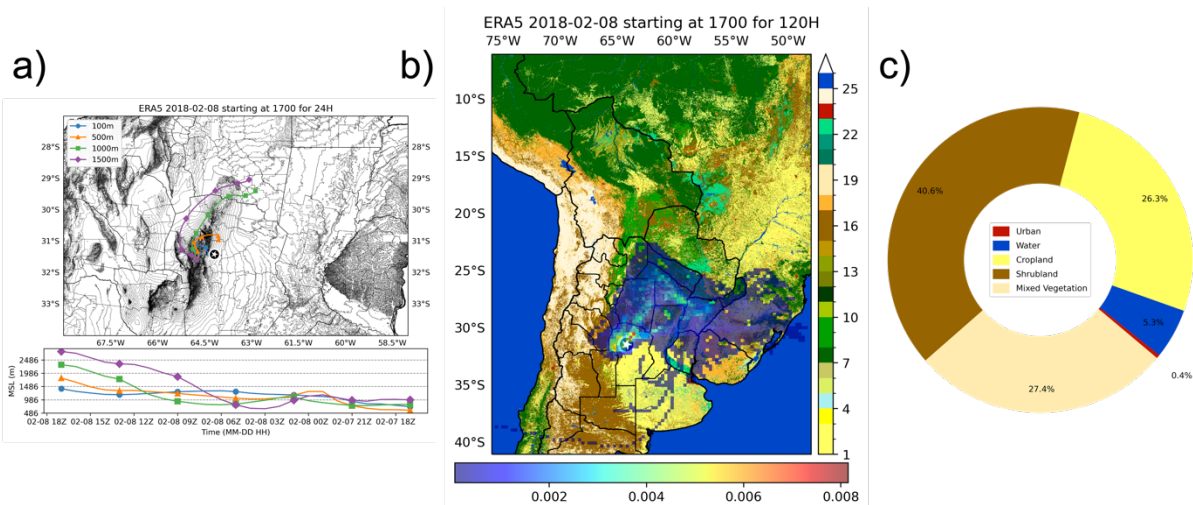


Figure 24.8: HYSPLIT analysis for 8 February 2018. (a) (top) shows 24-hour HYSPLIT back trajectories color-coded by height (in meters), with Córdoba City marked by a white star. The bottom of (a) displays terrain analysis in meters above sea level for the same time periods as the back trajectories. (b) shows residence time coefficients calculated for 5-day back trajectories overlaid on the C3S Land Cover map with Córdoba City marked by a white star. The land cover colors correspond to a subset of categories shown in Figure 1, specifically: 1/2/3-Cropland rain-fed, 4-Cropland irrigated, 5-Mosaic cropland, 6-Mosaic natural vegetation, 7-Evergreen broadleaved, 8/9/10-Deciduous broadleaved, 11-Evergreen needleleaved, 12-Mixed trees, 13-Mosaic tree/shrub, 14-Mosaic herbaceous, 15/16-Shrubland, 17-Grassland, 18-Sparse vegetation, 19-Sparse herbaceous, 20-Fresh water flooded tree cover, 21-Saline water flooded tree cover, 22-Flooded shrub/herbaceous cover, 23-Urban, 24-Bare areas, 25-Water, 26-Snow and ice. (c) displays the predominant land uses within the residence time coefficient pixels observed in b). Similar land uses were grouped into the following categories: Urban (23), Water (25,26), Cropland(1,2,3,4,5), Shrubland(15,16,17), Mixed Vegetation (6,7,8,9,10,11,12,13,14,18,19). Flooded Vegetation (20,21,22) and bare areas (24) were not included.

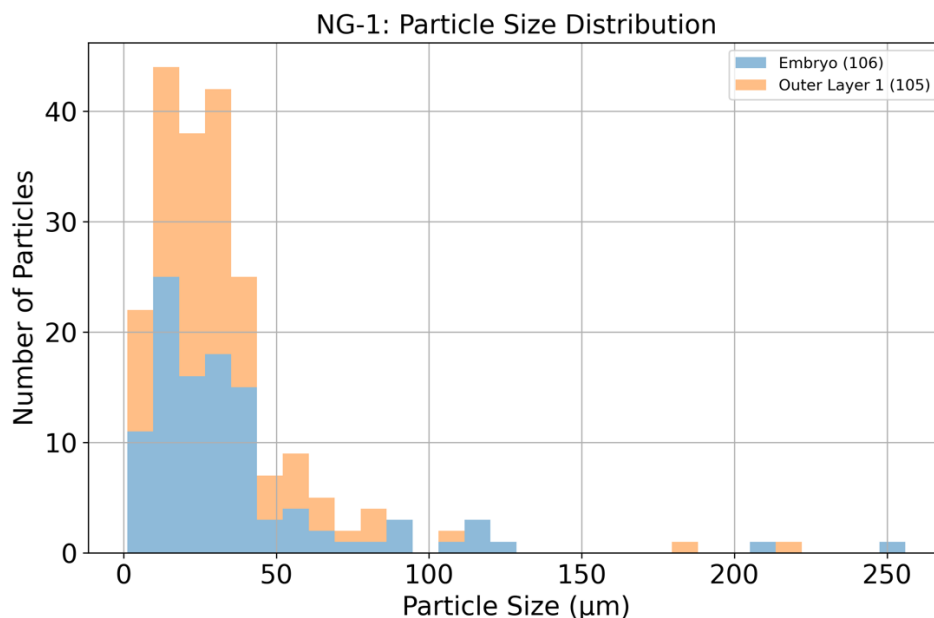


Figure 25: Particle size distribution in μm through the NG-1 cross-section is shown in Figure 3, where the particle size distribution in the hailstone embryo region is represented by blue pastel bars, and the particle size distribution in the outer layers of the hailstone is shown by orange pastel bars.

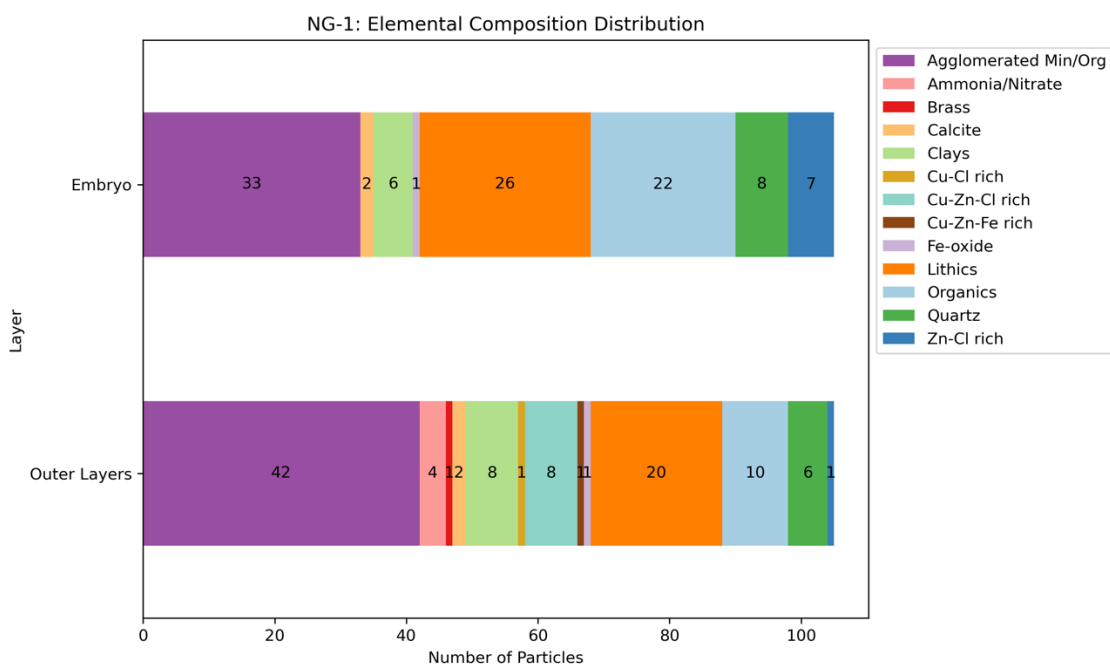


Figure 26: Elemental composition distribution for particles identified in the NG-1 cross-section shown in Figure 3.

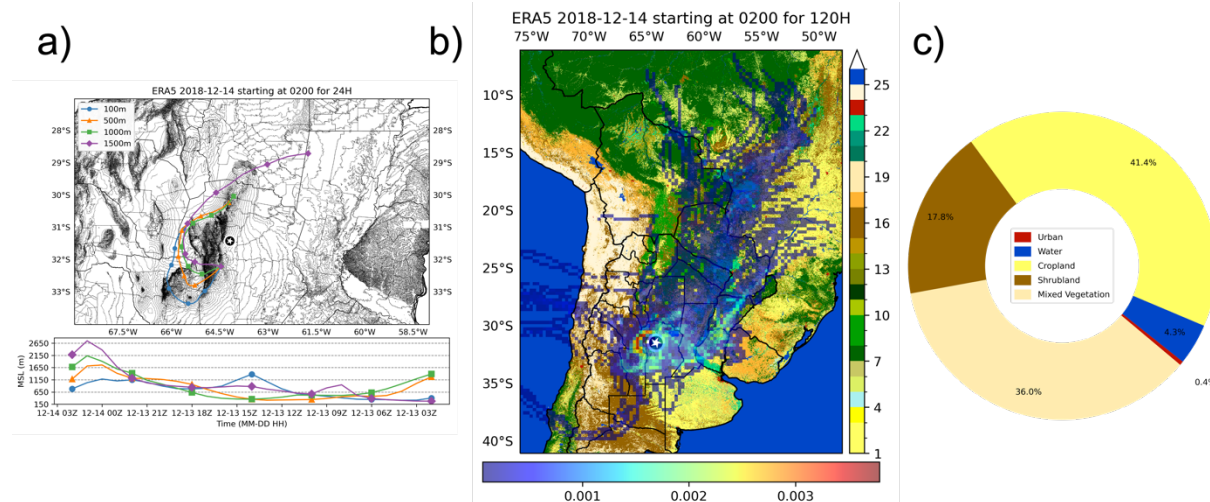


Figure 27: HYSPLIT analysis for 13-14 December 2018. (a) (top) shows 24-hour HYSPLIT back trajectories color-coded by height (in meters), with Córdoba City marked by a white star. The bottom of (a) displays terrain analysis in meters above sea level for the same time periods as the back trajectories. (b) shows residence time coefficients calculated for 5-day back trajectories overlaid on the C3S Land Cover map with Córdoba City marked by a white star. The land cover colors correspond to a subset of categories shown in Figure 1, specifically: 1/2/3-Cropland rain-fed, 4-Cropland irrigated, 5-Mosaic cropland, 6-Mosaic natural vegetation, 7-Evergreen broadleaved, 8/9/10-Deciduous broadleaved, 11-Evergreen needleleaved, 12-Mixed trees, 13-Mosaic tree/shrub, 14-Mosaic herbaceous, 15/16-Shrubland, 17-Grassland, 18-Sparse vegetation, 19-Sparse herbaceous, 20-Fresh water flooded tree cover, 21-Saline water flooded tree cover, 22-Flooded shrub/herbaceous cover, 23-Urban, 24-Bare areas, 25-Water; 26-Snow and ice. (c) displays the predominant land uses within the residence time coefficient pixels observed in b). Similar land uses were grouped into the following categories: Urban (23), Water (25,26), Cropland(1,2,3,4,5), Shrubland(15,16,17), Mixed Vegetation (6,7,8,9,10,11,12,13,14,18,19). Flooded Vegetation (20,21,22) and bare areas (24) were not included.

Chapter 4

Characterizing Overshooting Tops and Their Environments in Hail-Producing Convective Systems in Argentina

4.1 Preface

Hailstorms are one of the costliest natural hazards globally (Pucik et al. 2019). In the U.S. alone, hail-related insured losses have exceeded \$10 billion annually in recent years, while regions like Argentina, South Africa, and parts of Europe experience similarly devastating impacts on their agricultural sectors and urban infrastructure (Changnon 2008; Sander et al. 2013; Allen et al. 2017; Gunturi and Tippett 2017; Munich RE 2017; Kumjian et al. 2019b). Understanding the key atmospheric parameters and conditions contributing to the development, intensification, and dissipation of hail-producing convective storms is therefore crucial for predicting and mitigating these significant societal impacts.

Decades of research have identified several environmental parameters consistently linked to hail-producing storms (e.g., Allen et al. 2020). Most Unstable Convective Available Potential Energy (MUCAPE) and vertical wind shear have been identified as primary indicators of environments favorable for hail production (e.g., Das 1962; Gutierrez and Kumjian 2021; Zhou et al. 2021; Lin and Kumjian 2022). Studies have shown that the combination of MUCAPE, which supports strong updrafts, and vertical wind shear, which promotes storm organization, creates environments conducive to sustained hail growth. Additionally, environmental temperature profiles, particularly steep mid-level lapse rates in the hail growth zone, influence updraft strength and hail growth potential, while the wet-bulb zero height helps determine whether hailstones will melt before reaching the ground (Craven and Brooks 2004; Donavon and Jungbluth 2007). The relative importance of these parameters, however, varies significantly by region and storm mode (e.g., Zhou et al 2021).

While most foundational research on hail environments focused on the U.S., where discrete supercell storms dominate hail production, more recent studies have revealed important regional variations. Dennis and Kumjian (2017) demonstrated that the relationship between wind shear and hail production is complex, with deep-layer shear generally favoring large hail but strong low-level shear potentially inhibiting growth in some cases. This finding has particular relevance for regions where different storm modes predominate, such as Argentina, where multicellular systems frequently produce significant hail (Mullholand et al. 2018; Bruick et al. 2019; Bernal Ayala et al. 2022, 2024).

Argentina is a global hail hotspot with distinctly different characteristics from the well-studied U.S. environments. The Córdoba region, characterized by the Sierras de Córdoba (SDC) mountain range reaching heights up to 2,882 m, is known for its intense storms and frequent hail during warm convective seasons (October through February). The SDC's complex terrain plays a crucial role in storm initiation and evolution, creating unique conditions for hail formation not typically observed in U.S. environments. Bruick et al. (2019), using a 16-year Tropical Rainfall Measuring Mission (TRMM) dataset and ERA-Interim reanalysis data, highlighted several key differences between hailstorms in subtropical South America and the U.S. One notable distinction is the diurnal cycle of hailstorms. In subtropical South America, hailstorm activity near the SDC extends into the nocturnal hours more than in the U.S., with a secondary peak occurring between 0400 and 0600 local time, contrasting with the U.S. pattern of afternoon and early evening maxima. Furthermore, while U.S. hail production is dominated by discrete supercell storms, most nocturnal hailstorms in Argentina are organized multicellular systems.

Further studies by Mulholland et al. (2018), using ground-based operational radar data, found that most storms in the Córdoba region of Argentina during austral summers were multicellular, displaying rapid upscale growth near the Sierras de Córdoba compared to central U.S. storms. The ERA-Interim composites from this study showed that all convective modes were associated with strong upper-level westerly flow, large-amplitude upper-level troughs, and moisture provided by warm air from the Amazon rainforest region. Compared to the U.S., these convective systems displayed larger magnitudes of Mixed Layer Convective Available Potential Energy and Mixed Layer Convective Inhibition, weaker low-level shear, and higher Mixed Layer Lifting Condensation Level heights. However, this study was limited by its focus on all convective storms rather than specifically severe storms, its reliance on lower-resolution ERA-Interim data, and its analysis of only two seasons, highlighting the need for longer-term studies using higher-resolution data to better characterize severe storm environments in this region.

The role of the South American Low-Level Jet (SALLJ) appears particularly important in modulating these environments. Sasaki et al. (2024) demonstrated how the SALLJ enhances low-level directional shear and aligns cloud-layer wind shear parallel to the terrain, promoting organized convection. While their study focused on general convective development, our recent work (Bernal Ayala et al. 2022, 2024) found that one of their analyzed cases (December 13-14, 2018) produced severe hail, suggesting that SALLJ-modified environments may be particularly conducive to hail production when combined with other favorable parameters. The interaction between the SALLJ's enhanced low-level moisture transport and directional shear with upslope flow along the SDC may help explain the prevalence of hail-producing systems in this region.

While previous studies have established key differences in convective environments in Argentina compared to the U.S., details on hail environments remain underexplored. The complex interactions between terrain, the SALLJ, and varying storm modes suggest unique combinations of environmental parameters supporting hail production, but traditional ground-based observations are limited by sparse radar coverage and the challenging terrain of the SDC region. These limitations, combined with the nocturnal nature of many hail events in Argentina and the prevalence of rapidly evolving multicellular systems, need alternative approaches to studying hail-producing environments.

Satellite observations, particularly through the analysis of Overshooting Tops (OTs), offer a promising solution for studying hail environments in regions with limited ground-based coverage. OTs, which are cloud protrusions extending above the anvil cloud into the lower stratosphere, indicate strong updrafts capable of supporting hail formation. Grover (2021), using ground-based data from the 2018-2019 Remote sensing of Electrification, Lightning, and Mesoscale/microscale Processes with Adaptive Ground Observations (RELAMPAGO) field campaign, conducted an initial investigation of OT characteristics in Argentina. Through detailed analysis of three cases during the austral spring-summer transition (two in November and one in December 2018), Grover (2021) found preliminary evidence suggesting relationships between OT characteristics and storm modes: the supercell case exhibited large ($>100 \text{ km}^2$), long-lived OTs, while the multicellular case showed smaller, shorter-lived (approximately 4-minute duration) OTs, and the MCS case featured short-lived but large OTs. While these case studies provided valuable initial insights through combined satellite and ground-based observations, the limited sample size and seasonal coverage

highlighted the need for a more comprehensive analysis using a larger database of cases across different seasons and years.

Building on these findings, the Satellite Mapping & Analysis of Severe Hailstorms (SMASH) dataset (Bedka et al. 2010) offers several advantages for studying hail environments in Argentina. While Grover's 2021 analysis relied on intensive but temporally limited RELAMPAGO campaign data, which combined ground-based observations and dual-Doppler wind retrievals to study OT-updraft relationships, SMASH provides continuous, long-term monitoring using an objective infrared-window (IRW)-texture detection method. This approach, which identifies OTs using infrared brightness temperature gradients and 6-hour Global Forecast System (GFS) tropopause temperature forecasts, has been validated across hundreds of thunderstorm events in the eastern United States, achieving false-alarm rates as low as 4.2%. The dataset's proven utility in relating OT characteristics to environmental conditions in other hail-prone regions, demonstrated by Punge et al. (2023) in South Africa, suggests it could help extend Grover's detailed but temporally limited findings to a broader spatiotemporal scale in Argentina.

The need for reliable hail identification in satellite data has led to various approaches beyond OT detection. One widely referenced database is Bang and Cecil's (2019) climatology, which utilizes a multifrequency passive microwave hail retrieval approach. Their method analyzes brightness temperature thresholds from various microwave channels (10, 19, 37, and 85 GHz) onboard satellites like the Tropical Rainfall Measuring Mission (TRMM) and the Global Precipitation Measurement (GPM). By pairing brightness temperature-derived precipitation features with U.S. surface hail reports, they developed a hail retrieval algorithm using logistic curves fitted to the

microwave data. While their results identified several global hail hotspots, including northern Argentina, southern Brazil, and the central United States, subsequent analysis revealed important limitations. The authors identified biases in their dataset, particularly in northeastern Argentina, where their algorithm significantly overestimated hail occurrence. [Galligani et al. \(2024\)](#) confirmed these biases using polarimetric weather radar data and hydrometeor identification algorithms, demonstrating that actual hail occurrences were more concentrated in the southwestern regions of Argentina, particularly near Mendoza and Córdoba. These limitations of passive microwave approaches motivated the exploration of alternative satellite-based methods for inferring hail, particularly the three-dimensional radar capabilities of GPM's Dual-frequency Precipitation Radar (DPR). [Le and Chandrasekar \(2021\)](#) leveraged these DPR capabilities to develop a new hail identification algorithm that shows particular promise for studying hailstorms in Argentina. Their climatology successfully captured the expected concentration of hail events near the SDC, aligning with ground-based observations and previous studies of severe storm occurrence in the region.

By uniquely combining the SMASH and DPR-based hail identification databases, this study investigates how OT characteristics relate to their environmental conditions in Argentina's hail-producing storms. Specifically, we address the following research questions: What environmental conditions are associated with hail-producing storms, and how do these conditions manifest in satellite-observable storm characteristics? We hypothesize that: (1) environmental conditions associated with hail-producing OTs span a distinct range compared to non-hail-producing OTs, (2) environmental conditions supporting hail production show predictable patterns throughout the day, with distinct differences between afternoon, evening, and nocturnal periods, (3) OT characteristics

(i.e., area and depth) can help distinguish between hail-producing and non-hail-producing storms, and (4) specific combinations of environmental parameters correlate with OT characteristics in hail-producing storms.

To test these hypotheses, we pursue four specific objectives: (1) analyze the range of environmental conditions associated with all OTs during convective seasons, (2) examine the diurnal cycle of environmental conditions for OTs matched with GPM-DPR hail detections, (3) identify differences in temperature and OT area between all OTs and those matched with hail occurrences, and (4) investigate how OT area and depth covary with specific environmental parameters. Section 2 describes the datasets and methods used in this analysis. Section 3 presents the relationships between OT characteristics and their corresponding environmental parameters. Section 4 discusses these results in the context of previous work and explores their implications for understanding and predicting hail-producing storms in Argentina.

4.2 Data and Methods

4.2.1 SMASH Dataset

This analysis used the SMASH dataset (Bedka et al. 2010), which identifies and characterizes OTs using GOES-East satellite observations. From 2014-2022, this dataset included both GOES-13 (until December 2017) and GOES-16 (from December 2017) data, providing observations every

30 minutes (GOES-13) and 10 minutes (GOES-16) at spatial resolutions of 4 km and 2 km, respectively. OT detection used the water vapor minus infrared window brightness temperature difference technique, where positive differences indicate water vapor being forced into the warmer lower stratosphere by overshooting updrafts, recorded as a Deep Convection flag (DCflag).

The SMASH dataset provides OT intensity (through tropopause-relative IR brightness temperature), OT prominence relative to the surrounding anvil, and estimates of OT and anvil cloud top characteristics. These parameters are derived by combining satellite observations with the Modern-Era Retrospective analysis for Research and Applications, Version 2 (MERRA-2; Gelaro et al. 2017) reanalysis data. MERRA-2 provides tropopause temperature, pressure, and potential temperature information at 50-km grid spacing, with each OT assigned values from its containing grid cell. OT area calculations in SMASH first identify "cold" pixels with infrared window brightness temperatures ≤ 215 K that exceed the local GFS-derived tropopause temperature. The algorithm then searches within a 6-km radius of these center pixels to identify additional pixels that are at least 50% colder than the mean surrounding anvil brightness temperature, providing a measure of OT extent.

4.2.2 Environmental Parameters

MERRA-2 reanalysis data provides the environmental parameters used to characterize conditions associated with OT occurrence and characteristics. Available hourly at $0.5^\circ \times 0.625^\circ$ (about 50×65 km at the equator) horizontal spatial resolution, MERRA-2 supplies key parameters including MUCAPE, moisture (at the surface and 700 mb), vertical wind shear (0-3 and 0-6 km above the

surface), and Wet Bulb Zero Height. For each OT detection, environmental parameters were extracted from the MERRA-2 grid cell containing the OT location, using data from the nearest timestep preceding the GOES observation.

4.2.3 Analysis Approach

This study focuses on OTs detected by SMASH that coincide with GPM-DPR FlagHail product (Le and Chandrasekar 2023) within a 5-km radius from the OT center. The FlagHail product provides a binary indication of hail presence, where a value of 1 indicates hail was detected in the vertical column and 0 indicates no hail was detected. This spatial criterion accounts for the resolution difference between GPM-DPR FlagHail (5 km x 5 km) and GOES ABI infrared data (2 km x 2 km), ensuring that at least one full GPM-DPR FlagHail pixel is included in the OT analysis area while maintaining the original resolution of both datasets. The relatively small radius focuses on the immediate vicinity of the OT where hail formation is most likely to occur, rather than the broader area where hail might eventually reach the ground. For analysis, we selected only OTs with a probability greater than 0.5, as this is the threshold above which SMASH calculates OT area and depth measurements (Bedka et al. 2010). These OTs considered likely to be associated with hail-producing storms must also be associated with a positive DCflag and FlagHail value of 1 (Figure 4.1).

However, accurately matching OT and FlagHail observations requires addressing inherent geometric distortions in satellite imagery. Before performing the matching, geometric corrections were applied to both datasets to account for viewing angle displacements, which manifest

differently in geostationary satellites like GOES-East and polar-orbiting satellites like GPM. The apparent displacement of atmospheric features in satellite imagery occurs in both geostationary and polar-orbiting satellites but through different mechanisms. Geostationary satellites like GOES-16 experience classic parallax displacement due to their fixed position over the equator, which causes tall objects, such as thunderstorms, to appear displaced north and east/west of their true location, with displacements of up to ~ 10 km for mid-latitude storms (Bernal Ayala et al. 2023). In contrast, polar-orbiting satellites like NASA's GPM face a related phenomenon known as swath-edge displacement. While geometric considerations for GPM's scanning pattern and off-nadir observations are documented in the DPR Algorithm Theoretical Basis Document (Meneghini et al. 2021), the specific effects of swath-edge displacement have not been formally addressed in previous literature. This displacement occurs because these satellites observe Earth in swaths perpendicular to their orbital path; features observed off-nadir experience displacement toward the satellite's position due to oblique viewing angles. This displacement should be considered when collocating geostationary satellite data with polar orbiting data sets, needing geolocation algorithms for accurate precipitation profiling.

To correct for swath-edge displacement in GPM observations, a geometric correction algorithm from the University of Washington GPM-based feature database, managed by Stacy Brodzik, has been implemented for this study after being translated from FORTRAN to Python. The algorithm first standardizes input arrays to a consistent (nscan, nray) format, where nscan represents scans along the satellite track and nray represents the 49 rays across the scan swath. It then constructs three fundamental matrices: a height matrix spanning 176 vertical levels from 0 to 22 km at 125 m resolution, an angle matrix containing scan angles from -17° to $+17^\circ$ across the swath, and a

combined angle-range matrix for displacement calculations. Using these matrices, the algorithm calculates horizontal displacements based on the tangent of the viewing angle multiplied by height, converting the resulting distances from kilometers to degrees. The satellite's movement direction is determined by computing azimuth angles between consecutive scans, which is then used to establish shift directions. The correction is applied asymmetrically across the swath: points in the bottom half (rays 0-24) are shifted toward the satellite's forward direction, while points in the top half (rays 25-48) are shifted in the opposite direction. This approach accounts for the systematic displacement of features observed at off-nadir angles, particularly near swath edges where viewing angles are most oblique.

For GOES data, an adapted parallax correction algorithm, originally developed by James P. Nelson III (Cooperative Institute for Meteorological Satellite Studies, University of Wisconsin-Madison) in FORTRAN and translated to Python, was implemented. As discussed in Bernal Ayala et al. (2023), this algorithm accounts for Earth's ellipsoidal shape and the satellite's geostationary position, taking as input the Earth's equatorial and polar radii, the satellite's position (longitude, latitude, and height), the feature's apparent coordinates (longitude and latitude), and the feature's height above the surface. It first converts all angular measurements to radians and transforms both the satellite's and the feature's apparent positions into Cartesian coordinates, accounting for the Earth's ellipticity through a radius ratio parameter. The algorithm then computes the local zenith angle and solves a quadratic equation that determines the intersection of the satellite's line of sight with a surface at the feature's height. This intersection represents the feature's true position, considering both the Earth's curvature and the satellite's viewing geometry. Finally, the corrected

Cartesian coordinates are converted back to geodetic latitude and longitude, accounting for the Earth's ellipsoidal shape in the transformation.

To ensure the effectiveness of these geometric corrections, we validated our approach using a documented case study from Le and Chandrasekar 2023. This case was a verified hailstorm in northern Argentina on 2020-02-14 observed by GPM with orbit #33877, listed as one of the "Champion hail cases" in Battaglia et al. (2022). The corrected GPM-DPR flagHail data was collocated with the parallax-corrected GOES-16 Channel 11 brightness temperatures, with results shown in Figure 4.2. It is important to note that the swath-edge displacement correction was applied directly to the flagHail product. Future studies should examine potential differences between applying the correction to the level 2 flagHail product versus applying it to the raw radar data before calculating the flagHail product. Following validation of the geometric corrections, this algorithm was applied to the full dataset to ensure reliable matching between OTs and FlagHail detections. For matched cases (those within the spatial and temporal criterion), we then analyzed relationships between OT characteristics (area, depth) and environmental parameters from MERRA-2 reanalysis data.

4.3 Results

4.3.1 Spatial Distribution and Temporal Evolution

The analysis of OTs and hail occurrence across Argentina (Figures 4.3, 4.4) reveals distinct spatial patterns that vary with different detection criteria. The unfiltered SMASH-OT dataset (complete dataset before applying any filtering criteria; 2481 detections; Figure 4.3a) shows a broad distribution with higher concentrations in northeastern Argentina, which persists even after initial filtering by the deep convection flag (1298 detections; Figure 4.3b). Both the OT datasets and GPM-DPR FlagHail data (21092 detections; Figure 4.4b) show signals in northeastern Argentina as well as near the SDC, which extends north-south along the western edge of Córdoba Province (marked by the (C) symbol), with the strongest signal concentrated between approximately 30°S and 34°S. The FlagHail signal near the SDC is particularly noteworthy as it was not apparent in previous studies like Bang and Cecil (2019). However, when considering only OTs matched with GPM-DPR hail signals (189 detections; Figure 4.4a), the northeastern signal remains dominant while the SDC signal is substantially reduced. This reduction in matched cases near the SDC is an important consideration for the subsequent analysis of environmental conditions and storm characteristics in this region.

Table 3 quantifies these distributions across the study period (2014-2022), showing the progression from unfiltered to filtered to hail-matched OT counts for each month of the convective season (October-February). The data reveals substantial interannual variability, with total annual counts

ranging from a maximum of 478/227/19 (unfiltered/filtered/hail-matched) in 2015 to a minimum of 34/17/3 in 2022. January consistently shows the highest activity, with peak counts in 2019 (146/89/12) and 2021 (126/99/22). The filtering process typically reduces the total OT count by approximately 50%, while the strict hail-matching criteria further reduces the dataset to about 7-15% of the filtered cases, highlighting the selective nature of our matching approach.

The significant reduction from 2481 unfiltered OTs to 189 hail-matched OTs reflects our strict matching criteria. The filtered OT distributions (those with probabilities greater than 0.5 and DCflag value equal to 1) show a strong northeastern signal similar to Bang and Cecil (2019), and this northeastern dominance persists in the hail-matched distribution. Although the FlagHail product shows a notable signal near the SDC that was not apparent in Bang and Cecil (2019), this signal is less prominent in the matched OT-FlagHail cases, with peaks remaining in northeastern Argentina and in southwest/southern Córdoba.

While these spatial patterns provide insight into the geographic distribution of storms, their temporal evolution reveals distinct diurnal patterns in both the matched and flagHail databases. During the early hours (0-6 UTC, Figure 4.5a), both hail-matched OTs (52 cases) and FlagHail detections (6542 cases; Figure 4.5b) show activity particularly in the northeastern region, with the FlagHail database showing a signal near Córdoba that is less apparent in the matched cases. The mid-morning period (6-12 UTC; Figure 4.6a) sees a decrease in overall activity (39 OTs, 4192 FlagHail; Figure 4.6b), with concentrations primarily in the southern regions. Activity reaches its minimum in the afternoon (12-18 UTC; Figure 4.7a), with isolated occurrences primarily in the eastern regions (20 OTs, 2847 FlagHail; Figure 4.7b). However, it increases substantially during

the late afternoon and evening (18-23 UTC; Figure 4.8a, 78 OTs, 7511 FlagHail; Figure 4.7b), featuring a broader spatial distribution and enhanced activity both near Córdoba and in the northeastern regions. This diurnal pattern, particularly the nighttime maximum (18-23 UTC; Figure 4.8a) and secondary peak in the early morning (0-6 UTC; Figure 4.5a) aligns with previous findings by Bruick et al. (2019) regarding the secondary nocturnal peak of severe storms in subtropical South America.

4.3.2 OT Characteristics and Environmental Parameters

Having established the spatiotemporal distribution of hail-producing storms through our matched database, we next examine how OT characteristics differ between the full filtered OT dataset and the subset of hail-matched cases. This comparison reveals distinguishing characteristics of hail-producing OTs compared to the broader population of filtered OTs. Figure 4.9 presents this comparative analysis. The left panel compares OT areas between filtered and hail-matched OT counts with probabilities greater than 0.5. The filtered OT counts ($n=1298$, which include both hail-matched and non-matched cases) show a median area of around 175 km^2 with numerous outliers extending beyond 800 km^2 , reaching a maximum of approximately 1250 km^2 . The hail-matched counts ($n=189$) exhibit a higher median area ($\sim 225 \text{ km}^2$) and a larger interquartile range, though with fewer extreme outliers. The right panel displays the IR-tropopause temperature difference, a measure of OT penetration depth. Hail-matched cases show consistently more negative values (median $\sim -6\text{K}$) than filtered cases (median $\sim -4\text{K}$), indicating deeper penetration into the tropopause for storms with more confident hail cases. While both plots span similar ranges

from approximately -17K to 5K, with outliers reaching -20K, this deeper penetration in hail-matched cases suggests stronger updrafts.

Beyond the physical characteristics of the storms themselves, the environmental conditions they develop in provide a crucial context for understanding their behavior. Figure 4.10 compares environmental parameters between filtered and hail-matched OT counts through eight key environmental parameters. Regarding thermodynamic parameters, MUCAPE (Figure 4.10a) exhibits similar distributions for both filtered and hail-matched cases with medians between 2000-2500 J/kg and extreme values reaching 7000 J/kg, though hail-matched cases show slightly lower median values. Precipitable water values (Figure 4.10b) cluster between 40-50 mm for both counts, with outliers extending from 20-70 mm. While 0-3 km shear (Figure 4.10c) shows similar distributions (medians 6-8 m/s) for both populations, the 0-6 km shear (Figure 4.10d) displays slightly higher values for hail-matched cases (median ~16 m/s versus ~13 m/s), suggesting deep-layer shear may be a stronger signature in these cases. MUCIN (Figure 4.10e) shows similar distributions for both populations, with median values near 25 J/kg, though filtered cases exhibit numerous outliers extending beyond 400 J/kg. Cloud top heights (Figure 4.10f) are slightly higher in matched cases, with median values around 17.5 km compared to 17 km in filtered cases, and both show outliers reaching 24 km. Wet bulb 0°C heights (Figure 4.10g) are similar between both data sets, with median values near 4.2 km and ranging from approximately 2.5-5.5 km. The 500-700 hPa lapse rates (Figure 4.10h) show similar distributions centered around 6.3°C/km, with matched cases showing slightly less variability than filtered cases, though both range from about 4-8.5°C/km.

Having established these differences between hail-matched and filtered OT cases, we next focus specifically on how environmental conditions evolve throughout the day for the hail-matched cases. Figure 4.11 reveals distinct diurnal patterns across four periods (0-6, 6-12, 12-18, and 18-23 UTC, where local time in Córdoba is UTC-3). MUCAPE (Figure 4.11a) shows a pronounced cycle with peak values during 18-23 UTC (median ~ 3000 J/kg) while maintaining relatively consistent median values (~ 2000 J/kg) during other periods, though substantial variability exists across all time periods with values ranging from near zero to over 6000 J/kg. Precipitable water (Figure 4.11b) shows modest diurnal variation, with slightly higher values during early morning hours (0-6 UTC, median ~ 50 mm) compared to a median of ~ 45 mm during other periods. Wind shear parameters (Figures 11c,d) show the highest values during early morning hours (0-12 UTC) and decrease notably during 18-23 UTC, with low-level shear ranging from ~ 8 m/s to ~ 3 m/s and deep-layer shear varying from ~ 17 m/s to ~ 12 m/s throughout the day. This early morning maximum likely reflects the influence of the SALLJ, which typically reaches peak intensity during these hours (Sasaki et al. 2024). MUCIN (Figure 4.11e) exhibits strongest values during early morning hours (0-6 UTC, median ~ 50 J/kg), gradually decreasing through the day to minimal values during 18-23 UTC (~ 10 J/kg). Cloud top heights (Figure 4.11f) show slight variations, with higher median values during early morning (~ 18 km at 0-6 UTC) and evening hours (~ 17.5 km at 18-23 UTC) and lower values during midday (~ 16.5 km at 12-18 UTC). Wet bulb zero heights (Figure 4.11g) maintain median values around 4.2 km throughout the day, with slightly more variability during evening hours (18-23 UTC). The 500-700 hPa lapse rates (Figure 4.11h) show a subtle diurnal cycle with steeper rates during early morning hours ($\sim 6.7^\circ\text{C}/\text{km}$ at 0-6 UTC, 21-03 local time) and more moderate values during afternoon periods ($\sim 6.0^\circ\text{C}/\text{km}$ at 12-18 UTC, 09-15 local time).

In summary, this analysis of physical characteristics and environmental parameters reveals several key features of Argentina's hail-producing storms. Hail-matched OTs demonstrate larger median areas ($\sim 225 \text{ km}^2$) and deeper penetration into the tropopause (median -6K vs -4K), suggesting stronger updrafts in matched OTs. While some environmental parameters show similar distributions between filtered and matched cases (MUCAPE: 2000-2500 J/kg, precipitable water: 40-50 mm), others, like deep-layer shear, exhibit notable differences (16 m/s vs 13 m/s in matched cases). The diurnal analysis reveals patterns that may be a reflection of the diverse storm modes observed in this region. Afternoon environments (18-23 UTC) feature peak MUCAPE values favorable for discrete storms, aligning with Grover (2021) observations of large, long-lived OTs in supercellular cases. In contrast, early morning hours (0-12 UTC) show enhanced wind shear, likely influenced by the SALLJ, and stronger CIN values, conditions more conducive to organized multicellular systems and MCSs, which Grover (2021) found to be characterized by different OT signatures (shorter-lived but potentially large OTs for MCS cases, and smaller, shorter-lived OTs for multicellular events). While Grover's analysis was limited to three cases during RELAMPAGO, our larger dataset provides broader context for these environmental patterns and their temporal variations and motivates our subsequent correlation analysis, which examines how OT characteristics vary across these different storm environments throughout the diurnal cycle.

4.3.3 Parameter Relationships and Storm Organization

The relationships between environmental parameters and storm characteristics reveal distinct patterns. Figure 4.12 quantifies these relationships through correlation analysis between OT area and various environmental parameters for hail-matched OTs. Cloud top height (Figure 4.12f)

shows the strongest correlation ($r = 0.39$) with OT area, indicating that larger OTs tend to reach higher altitudes, a relationship physically consistent with stronger updrafts supporting both larger OT areas and higher cloud tops. Wind shear parameters (Figure 4.12 c,d) show weak to moderate positive correlations ($r = 0.21$ for 0-3 km and $r = 0.12$ for 0-6 km shear), suggesting that stronger shear environments may support larger OT development. Thermodynamic parameters show varying degrees of correlation: MUCAPE (Figure 4.12a) exhibits a weak positive correlation ($r = 0.16$), as does the 500-700 hPa lapse rate ($r = 0.18$; Figure 4.12h), indicating that while instability plays a role in OT development, the relationship is not strongly linear. The remaining parameters show minimal correlation with OT area: precipitable water ($r = 0.06$; Figure 4.12b), MUCIN ($r = 0.09$; Figure 4.12e), and wet bulb zero height ($r = 0.05$; Figure 4.12g), suggesting these parameters have limited direct influence on OT size. This pattern of correlations suggests that while individual parameters may contribute to OT development, no single parameter strongly determines OT area, pointing to the complexity of processes involved in storm development across different storm modes.

Extending this correlation analysis to examine OT intensity, Figure 4.13 investigates relationships between IR-tropopause temperature difference and environmental parameters. Cloud top height (Figure 4.13f) maintains the strongest correlation ($r = -0.53$), with colder cloud tops (more negative temperature differences) corresponding to higher vertical development, a physically consistent relationship. The 500-700 hPa lapse rate (Figure 4.13h) shows a moderate negative correlation ($r = -0.23$), suggesting that stronger mid-level instability may support deeper OT penetration. Several parameters show weak negative correlations: MUCAPE ($r = -0.15$; Figure 4.13a) and both wind shear parameters ($r = -0.05$ for 0-1 km, Figure 4.13c, and $r = -0.11$ for 0-6 km shear, Figure 4.13d),

indicating a slight tendency for stronger updrafts in more unstable and sheared environments. The remaining parameters show virtually no correlation with IR-tropopause temperature difference: precipitable water ($r = 0.03$; Figure 4.13b), MUCIN ($r = -0.04$; Figure 4.13d), and wet bulb zero height ($r = 0.04$; Figure 4.13g).

Given that both Grover's (2021) case studies and our diurnal analysis suggest different storm modes exhibit distinct combinations of OT characteristics, Figure 4.14 explores how environmental parameters vary jointly with both OT area and depth. Through color-coded scatter plots, we can examine how specific environmental conditions might support different combinations of OT size and penetration depth. The strong negative correlation ($r = -0.72$) between OT area and IR-tropopause temperature difference demonstrates that larger OTs tend to have colder cloud tops, suggesting stronger updrafts support both larger horizontal extent and deeper vertical penetration. MUCAPE values (panel a) show higher values (yellow colors, >5000 J/kg) scattered across various OT sizes but tend to concentrate in intermediate-sized OTs. Precipitable water (panel b) shows higher values (50-70 mm, greener colors) distributed across the size range, with no clear pattern relative to temperature differences. Wind shear parameters (panels c, d) show that stronger shear values (yellow colors) tend to occur with intermediate-sized OTs and moderate temperature differences, particularly for 0-6 km shear. MUCIN (panel e) shows generally lower values (darker colors) across most cases, with occasional higher values scattered throughout. Cloud top heights (panel f) show a clear gradient, with higher tops (yellow colors, >20 km) associated with larger OTs and colder cloud tops. Wet bulb zero heights (panel g) show higher values (yellow colors, >4.5 km) more commonly in moderate-sized OTs. The 500-700 hPa lapse rates (panel h) show steeper rates (yellow colors, $>7^{\circ}\text{C}/\text{km}$) occurring more frequently with

intermediate to larger OTs and colder cloud tops. This multi-parameter analysis reveals that while individual parameters may show specific patterns, the overall storm characteristics appear to result from complex interactions between multiple environmental conditions.

Figure 4.15 further explores these relationships through a correlation between key environmental parameters, with each relationship shown twice, once colored by OT area (top row) and once by IR-tropopause temperature difference (bottom row). The strongest relationship appears between wet bulb zero height and precipitable water (panels d, h, $r = 0.71$), showing the expected physical relationship where higher atmospheric moisture content results in higher wet bulb zero levels. The 500-700 hPa lapse rate shows a notable negative correlation (panels b, f, $r = -0.55$) with wet bulb zero height, suggesting that steeper lapse rates typically occur with lower wet bulb zero heights. This relationship appears particularly strong for cases with moderate OT areas (300-600 km²). Precipitable water maintains a moderate positive correlation (panels c, g, $r = 0.42$) with MUCAPE, showing that more unstable environments tend to have higher moisture content. The deep-layer wind shear shows a weak negative correlation (panels a, e, $r = -0.21$) with MUCAPE, indicating a slight tendency for stronger shear to occur in less unstable environments. The color coding reveals additional insights: larger OTs (yellowish colors in the top row) tend to occur across various parameter combinations, while colder cloud tops (darker blues in the bottom row) are more common with higher MUCAPE values and in environments with moderate to strong wind shear. This multi-parameter analysis suggests that while certain parameter combinations may be more favorable for OT development, hailstorms can occur across various environmental conditions.

The variability in environmental conditions and OT characteristics suggests different storm modes may be present in our dataset. While we cannot directly identify storm modes as Grover (2021) did using Doppler radar data, we can attempt to classify storms based on their spatial and temporal organization. Following, but modifying, Punge et al. (2023)'s method to classify multicellular systems from OTs, we implemented a threshold-based classification approach specifically for our hail-matched OTs. This focus on hail-matched cases, rather than all OTs as in Punge et al. (2023) study, significantly constrains our classification. Our classification uses a Python function that iterates through the hail-matched OT dataset, comparing each hail-matched OT with other hail-matched OTs to determine event membership. Hail-matched OTs detected within 1 hour and 30 kilometers of each other were classified as part of the same multicellular event, while isolated hail-matched OTs were classified as single-cell storms. Figures 4.16 and 4.17 provide a view of storm classification and morphology, with Figure 4.16 mapping the spatial distribution of 181 single-cell storms and the 4 resulting multicellular events. Single-cell storms show a broad distribution across the domain, with notable concentrations in northeastern Argentina and scattered occurrences near the SDC range, which extends north-south along the western edge of Córdoba Province, immediately west of Córdoba city. This distribution, particularly the concentration of storms in northeastern Argentina, reflects the patterns seen in our earlier analysis of matched OT cases, though the limited number of classified multicellular events likely underestimates storm organization due to our strict matching criteria and GPM sampling constraints.

The four multicellular events, captured in Figure 4.17's GOES-16 ABI Band 11 imagery, demonstrate diverse organizational structures across different regions and times. The November 10, 2018 event (21:51 UTC) featured two OTs at (-34.08°S, -56.08°W) and (-34.13°S, -55.76°W),

displaying an extensive system with multiple embedded convective cores. The January 16, 2021, event (19:16 UTC) showed two coincident OTs at (-25.81°S, -65.04°W) in the northern region, characterized by a compact structure with intense cells in close proximity. The February 13, 2021, case (20:24 UTC) near the Rio de la Plata (-34.44°S, -58.72°W) exhibited scattered but interconnected cells, while the February 26, 2021, event (16:59 UTC) in southern Argentina (-38.22°S, -65.67°W) presented a well-defined convective cluster.

Environmental conditions associated with these storm types, as shown in Figure 4.18, show some distinctions between single-cell and multicellular organizations. Single-cell storms (N=181) exhibit greater variability across all parameters, with environments characterized by higher wind shear values (0-1 km shear medians ~6 m/s vs ~2 m/s, and 0-6 km shear medians ~16 m/s vs ~12 m/s), stronger inhibition (CIN up to 350 J/kg), and steeper 500-700 hPa lapse rates (median ~6.3°C/km vs ~6.0°C/km). In contrast, multicellular storms (N=8), despite their limited sample size, show slightly higher median MUCAPE (~2500 vs ~2000 J/kg) but lower precipitable water values (~42 vs ~45 mm). Cloud top heights show similar median values between both types (~17 km), though single cells display greater variability with outliers reaching 24 km. Wet bulb zero heights maintain comparable distributions between the two categories, with medians around 4.2 km, though single cells show a wider range from 2.8 to 5.5 km. The higher shear values in our single-cell cases suggest these may include supercellular storms, while the lower shear values in multicellular cases align with typical MCS environments, though our limited multicellular sample size warrants caution in these interpretations.

The predominance of single-cell classifications (181 versus 4 multicellular events) presents an interesting contrast to previous studies (e.g., Mulholland et al. 2018, Bruick et al. 2019) that suggested multicellular systems are common in this region. This disparity stems from two key limitations in our approach: first, the GPM's limited temporal sampling, with only two overpasses per day at any given location, potentially missing many multicellular events or capturing them at non-optimal times in their life cycle; and second, our strict requirement that all nearby OTs must be associated with hail detections to be classified as multicellular, rather than considering non-hail-producing OTs that might indicate broader storm organization. The temporal coincidence of OT pairs in three of the four multicellular cases (same minute detections) suggests these represent simultaneous intense updrafts within organized convective systems rather than temporally evolving single cells. While the identified relationships between storm characteristics and environmental parameters suggest that storm organization in Argentina depends on multiple interacting factors, from local terrain influences to larger-scale atmospheric conditions, these limitations warrant further investigation with complementary observational approaches that could better capture the full spectrum of storm organization.

4.4 Discussion and Conclusions

This study investigated how OT characteristics relate to their environmental conditions in Argentina's hail-producing storms by testing four hypotheses based on prior literature using different datasets. Using a unique combination of SMASH-OT detections and GPM-DPR FlagHail data during convective seasons from 2014-2022, this analysis examined whether: (1) environmental conditions associated with hail-producing OTs span a distinct range compared to

non-hail-producing OTs, (2) environmental conditions supporting hail production show systematic diurnal variations, (3) OT characteristics (area and depth) can help distinguish between hail-producing and non-hail-producing storms, and (4) specific combinations of environmental parameters correlate with OT characteristics in hail-producing storms.

The analysis revealed distinct characteristics of hail-producing environments in Argentina, with some differences from the broader OT dataset. While some parameters like MUCAPE showed similar distributions between hail-matched and filtered cases (2000-2500 J/kg), deep-layer shear in hail-matched cases (median ~16 m/s) was higher than in the filtered OT dataset (median ~13 m/s), which includes both hail matched and non-hail matched cases, though both remained lower than typically observed in U.S. severe storms (Craven and Brooks 2004; Dennis and Kumjian 2017). This finding extends Mulholland et al.'s (2018) work by demonstrating that while hail-producing storms in Argentina operate in weaker shear environments than their U.S. counterparts, hail-matched cases tend to occur in environments with somewhat stronger deep-layer shear, though with considerable overlap in the distributions.

These environmental conditions showed pronounced temporal variations throughout the day. MUCAPE exhibited an expected clear diurnal cycle with peak values during 18-23 UTC (~3000 J/kg). Wind shear parameters displayed an inverse pattern, with maximum values during early morning hours (0-12 UTC) and minimum values during 18-23 UTC, consistent with Sasaki et al.'s (2024) findings about how the SALLJ enhances low-level directional shear and aligns cloud-layer wind shear parallel to the terrain during overnight hours. While Sasaki et al. (2024) demonstrated this SALLJ influence on general storm organization without specifically addressing hail

production, our previous work (Bernal Ayala et al. 2022, 2024) identified significant hail production in one of their analyzed cases (December 13-14, 2018), suggesting SALLJ-modified environments may be particularly conducive to hail formation when combined with other favorable parameters. MUCIN followed a typical nocturnal pattern, with strongest values during early morning hours (0-6 UTC, ~ 50 J/kg) decreasing to minimal values by late afternoon. This temporal variability aligns with Bruick et al.'s (2019) findings about the nocturnal nature of severe storms in this region, where enhanced shear and stronger CIN during overnight hours favor organized multicellular systems over discrete storms. While our twice-daily sampling provides only a partial view of these variations, the environmental patterns support the transition from afternoon discrete cells in high MUCAPE/lower shear environments to nocturnal multicellular systems in enhanced shear conditions.

These temporal patterns in environmental conditions correspond with distinct characteristics in the OTs themselves. Hail-matched OTs showed larger median areas (~ 225 km² versus ~ 175 km²) and deeper penetration into the tropopause (median -6K versus -4K) compared to non-hail cases. While the northeastern signal remained dominant in our hail-matched cases, the FlagHail database from Le and Chandrasekar (2023) revealed a notable signal near the SDC that was not apparent in Bang and Cecil's (2019) analysis. However, this SDC signal was substantially reduced when requiring temporal and spatial matches between FlagHail detections and OTs, highlighting both the value and limitations of combining these datasets for studying hail-producing storms in this region.

Building on Grover's (2021) initial findings about OT characteristics in different storm modes, our expanded analysis revealed relationships between environmental conditions and OT features

across a larger dataset. Individual parameters showed relatively weak correlations with OT characteristics ($r \leq 0.39$), with cloud top height showing the strongest correlation with OT area ($r = 0.39$). The strong negative correlation between OT area and IR-tropopause temperature difference ($r = -0.72$) supports Grover's 2021 observations that different storm modes exhibit distinct OT signatures, with larger, deeper OTs typically associated with more intense updrafts. The analysis also identified key thermodynamic relationships that influence storm development: the strong correlation between wet bulb zero height and precipitable water ($r = 0.71$) reflects how increased moisture content leads to higher wet bulb zero heights by raising the melting level. This relationship is physically consistent since more moisture in the atmosphere requires more cooling for saturation and freezing to occur. The negative correlation between 500-700 hPa lapse rates and wet bulb zero height ($r = -0.55$) aligns with fundamental thermodynamic principles, steeper lapse rates typically occur in drier environments where rapid cooling with height is less inhibited by latent heat release.

These findings must be considered within several important dataset limitations. Beyond the GPM's temporal sampling constraints (two passes daily) limiting the analysis to snapshots of storm conditions, several methodological choices affected our ability to match OTs with hail occurrence. First, applying the deep convection filter to SMASH and restricting analysis to OTs with >0.5 probability ensured focus on the most intense updrafts but reduced the potential matches. Second, while our 5-km matching radius attempted to account for potential updraft tilting, where OTs might not be vertically aligned with detected hail, this fixed radius might have missed some valid associations. Third, our strict temporal matching criteria likely missed important relationships, as previous studies, including Cintineo et al. (2020) and Bernal Ayala et al. (2022), showed that the

strongest OT signatures often precede hail production by several minutes. These factors help explain why not all FlagHail detections have associated OTs, despite the expectation that hail-producing storms should exhibit overshooting tops. The combination of these constraints particularly affects the identification of organized convective systems, as our criteria require multiple OTs within a system to each have corresponding FlagHail detections during a GPM overpass. This dual requirement of temporal coincidence and hail matches for all OTs likely explains why our classification (181 isolated versus 4 multiple-OT cases) significantly underrepresents the frequency of organized convective systems that Bruick et al. (2019) and Mulholland et al. (2018) found common in this region. However, while these strict spatial, temporal, and quality criteria limited our sample size, they provide confidence in the identification of confirmed hail-producing storms within our dataset.

Despite these constraints, this study provides valuable insight into how environmental conditions support hail production across different storm modes and times in Argentina. While U.S. based studies typically focus on afternoon/evening supercells and multicellular storms, our analysis reveals how hail-producing environments in Argentina support both afternoon discrete cells and nocturnal MCSs. The integration of SMASH OT detections with GPM-DPR FlagHail data enabled us to identify how environmental parameters vary throughout the diurnal cycle, with afternoon environments featuring higher MUCAPE favorable for discrete storms, while nocturnal periods show enhanced shear and CIN values more conducive to organized systems. These findings suggest that traditional U.S. based environmental thresholds for hail prediction may need regional adaptation, particularly in areas where nocturnal convection plays a significant role. Future work should expand this analysis using higher-temporal-resolution datasets and ground validation to

better understand how environmental conditions support different hail-producing storm modes across various geographical regions.

Based on these findings and limitations, several recommendations should be considered for future research:

1. Evaluate the sensitivity of satellite dataset matching to different spatial thresholds and geometric corrections. This includes quantifying the impact of parallax and swath-edge displacement corrections on OT-FlagHail matching accuracy, particularly important when combining these datasets with ground-based radar observations and surface hail reports.
2. Expand the multicellular classification scheme to include non-hail-producing OTs in proximity to hail-matched OTs. This would better capture organized convective systems where not all updrafts simultaneously produce hail, providing a more complete picture of storm organization patterns in this region.
3. Integrate ground-based radar observations where available to validate and complement satellite-based hail detection, following approaches like Galligani et al. (2024). This would help verify FlagHail detections and provide additional information about storm structure and evolution between satellite overpasses.
4. Develop methods to better identify and track hail-producing storms between GPM overpasses by incorporating GOES-derived storm tracking information, helping to connect

non-simultaneous observations and better understand how environmental conditions influence storm evolution.

Ultimately, this research demonstrates that satellite-based approaches can provide valuable insights into severe storm environments in regions with limited ground-based observations. The methodology developed here could be adapted for other regions globally where traditional observational networks are sparse, potentially improving our understanding of severe storm environments worldwide. Applying these techniques to other documented global hail hotspots would enable the development of a consistent, worldwide database of hail-producing storm environments. Such a database would facilitate direct comparisons between regions and advance our understanding of how different environmental conditions and geographical features influence hail development across diverse climate regimes.

4.5 Figures

Table 3: Monthly and annual OT counts for October (10) through February (02) from 2014-2022, showing three categories: unfiltered / filtered / hail-matched detections. Filtered counts include only OTs with probabilities greater than 0.5 and deep convection flag equal to 1, while hail-matched counts represent OTs successfully matched with GPM-DPR FlagHail detections. Total annual counts are shown in the bottom row.

Total OT Counts (No filter / Filtered / Hail matched)									
	2014	2015	2016	2017	2018	2019	2020	2021	2022
01	0 / 0 / 0	129 / 68 / 7	83 / 39 / 1	105 / 42 / 3	53 / 35 / 2	146 / 89 / 12	93 / 61 / 11	126 / 99 / 22	20 / 7 / 0
02	0 / 0 / 0	84 / 26 / 4	140 / 36 / 1	80 / 28 / 1	67 / 38 / 7	88 / 41 / 6	96 / 54 / 10	46 / 29 / 5	14 / 10 / 3
10	37 / 24 / 2	53 / 23 / 1	45 / 31 / 3	68 / 28 / 7	76 / 61 / 17	0 / 0 / 0	38 / 14 / 5	18 / 15 / 4	0 / 0 / 0
11	46 / 13 / 0	78 / 31 / 3	45 / 27 / 2	27 / 7 / 0	51 / 31 / 9	0 / 0 / 0	28 / 19 / 0	11 / 9 / 0	0 / 0 / 0
12	84 / 45 / 6	134 / 79 / 4	71 / 21 / 2	72 / 30 / 3	90 / 62 / 18	0 / 0 / 0	30 / 18 / 6	9 / 8 / 2	0 / 0 / 0
Total	167 / 82 / 8	478 / 227 / 19	384 / 154 / 9	352 / 135 / 14	337 / 227 / 53	234 / 130 / 18	285 / 166 / 32	210 / 160 / 33	34 / 17 / 3

Spatial Representation of OT Data Filtering
with GPM-DPR FlagHail
Case study: 2020-2-14

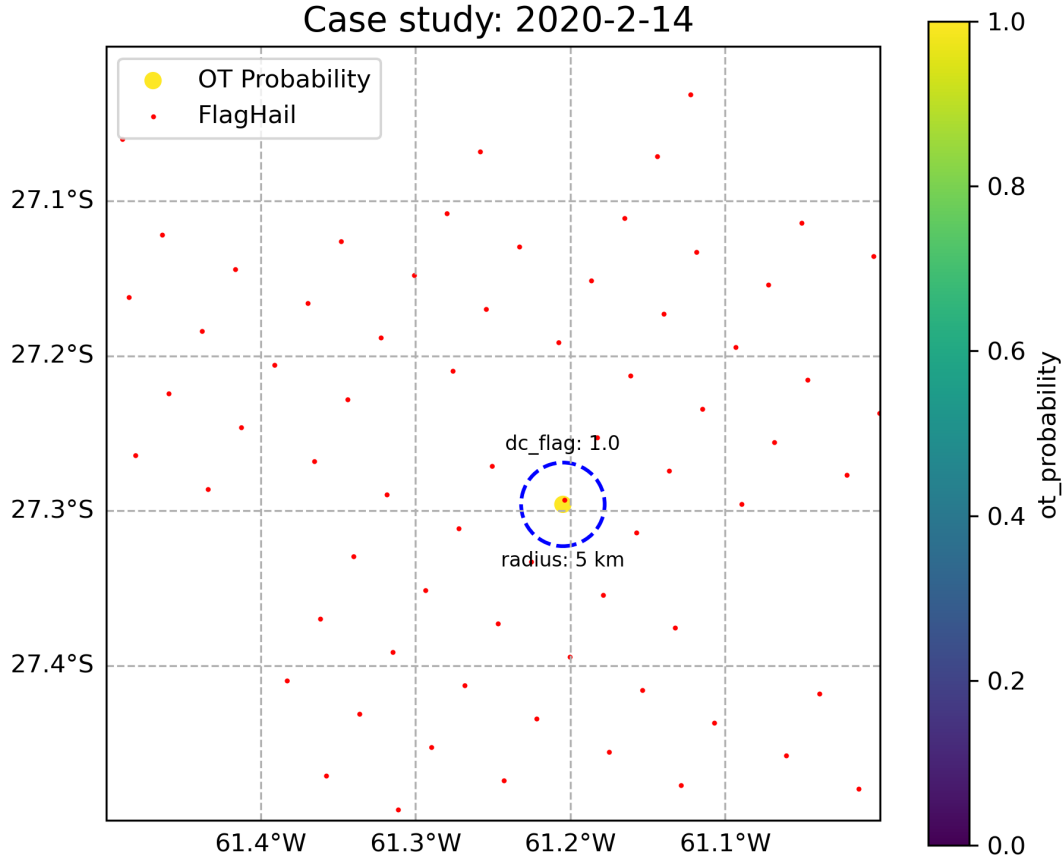


Figure 28: Example of the spatial matching process between SMASH OT detections (probability in filled colors) and GPM-DPR FlagHail data (red dots) for February 14, 2020. The blue dashed circle illustrates the 5-km radius search area around the OT used for matching with FlagHail detections. This OT has a deep convection (dc) flag value of 1.0, indicating it meets the deep convection criteria.

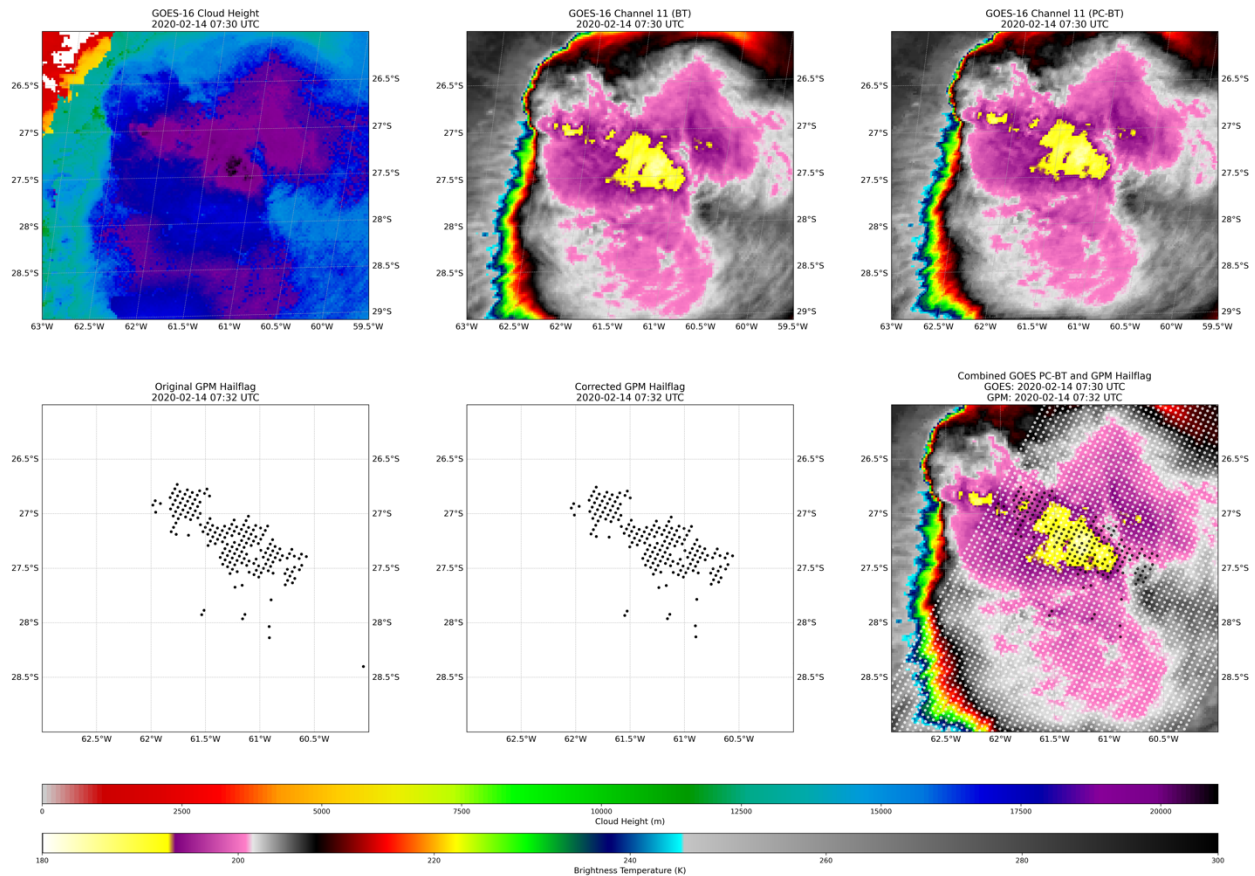


Figure 29: Demonstration of the GPM-DPR FlagHail and GOES data matching process for a case study on February 14, 2020, around 0730 UTC. Top row shows GOES-16 data: (left) cloud height in m, (center) Channel 11 brightness temperature in K (BT), and (right) parallax-corrected Channel 11 brightness temperature (PC-BT). Bottom row shows: (left) original GPM FlagHail detections, (center) swath-edge displacement corrected FlagHail detections, and (right) the combined visualization of parallax-corrected GOES imagery with corrected FlagHail detections. Yellow regions in the BT images indicate areas meeting OT detection criteria, while pink shading shows the anvil cloud extent.

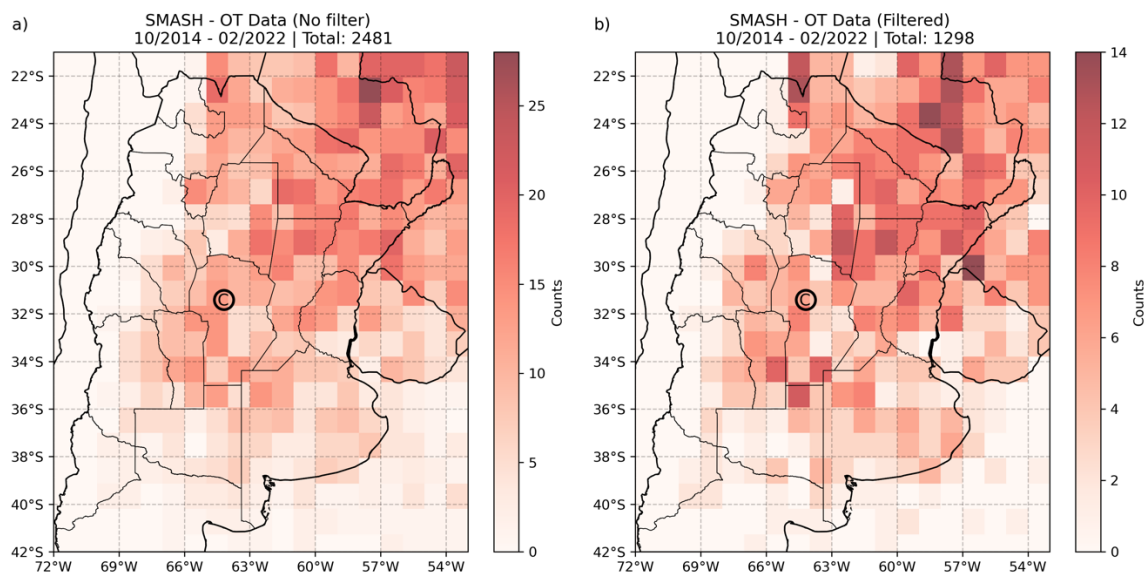


Figure 30: Spatial distribution of SMASH OT detections from October 2014 through February 2022. (a) Unfiltered OT counts (total: 2481) showing all detected OTs. (b) Filtered OT counts (total: 1298) showing only OTs with probability values greater than 0.5 and deep convection flag equal to 1. Both panels use a $1^\circ \times 1^\circ$ grid, with color intensity indicating the number of OTs per grid cell. The circled C marks the location of Córdoba city.

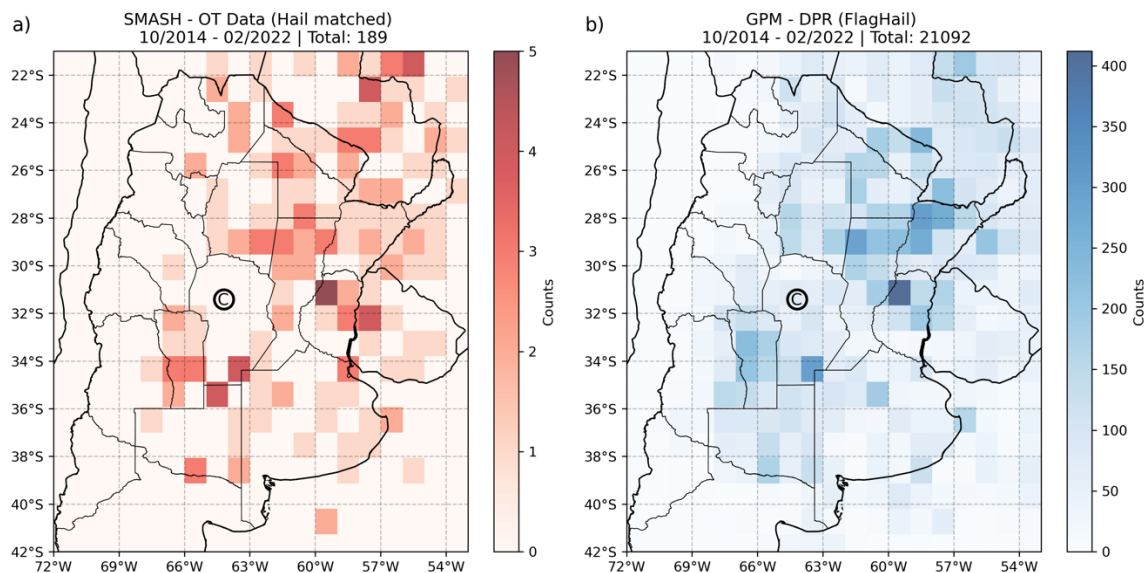


Figure 31: Comparison of (a) hail-matched SMASH OT detections (total: 189) and (b) GPM-DPR FlagHail detections (total: 21092) across Argentina from October 2014 through February 2022. Both panels use a $1^\circ \times 1^\circ$ grid, with the circled C marking Córdoba city. Panel (a) shows OTs that were successfully matched with FlagHail detections using spatial and temporal criteria, with counts per grid cell (in red shading). Panel (b) displays the total FlagHail detections, with counts per grid cell in blue shading.

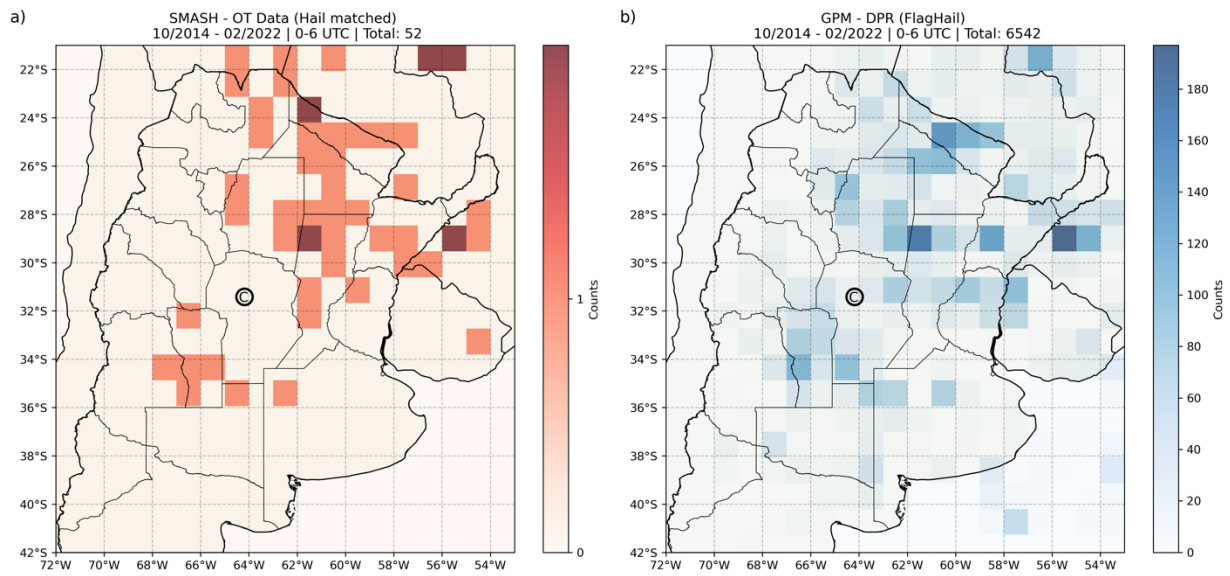


Figure 32: As in Figure 4.4 but for 0-6 UTC, 21-03 local time.

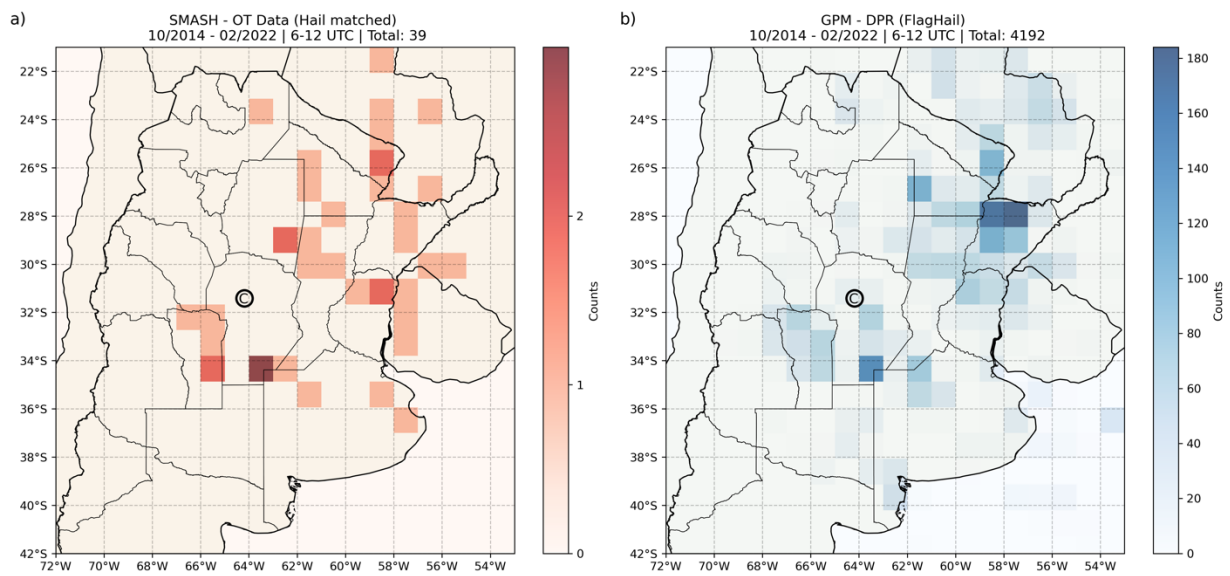


Figure 33: As in Figure 4.4 but for 6-12 UTC, 03-09 local time.

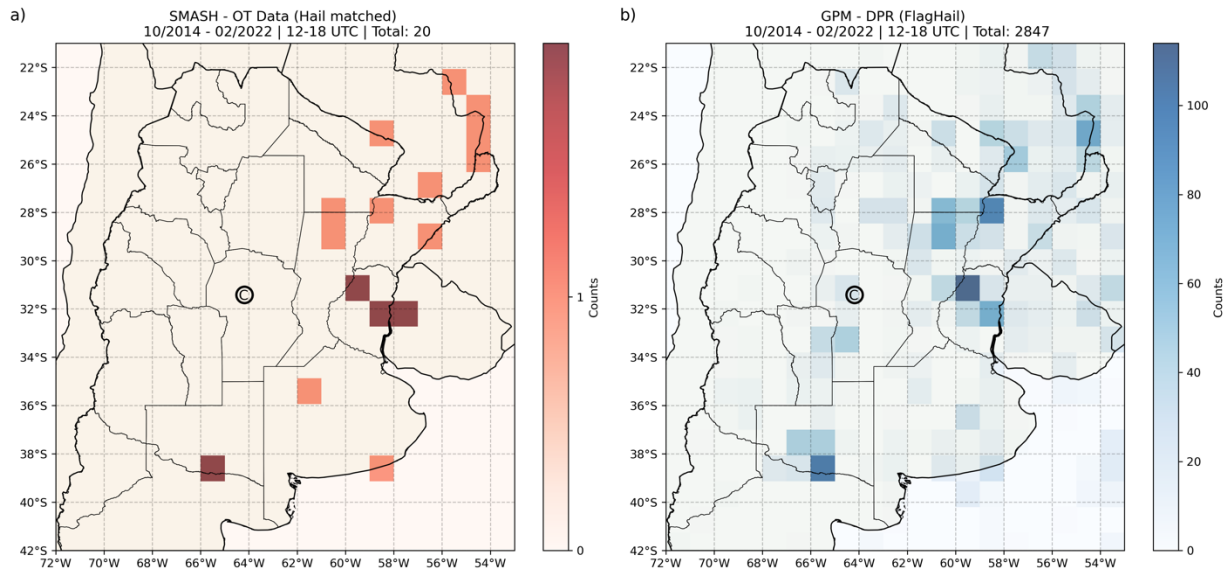


Figure 34: As in Figure 4.4 but for 12-18 UTC, 09-15 local time.

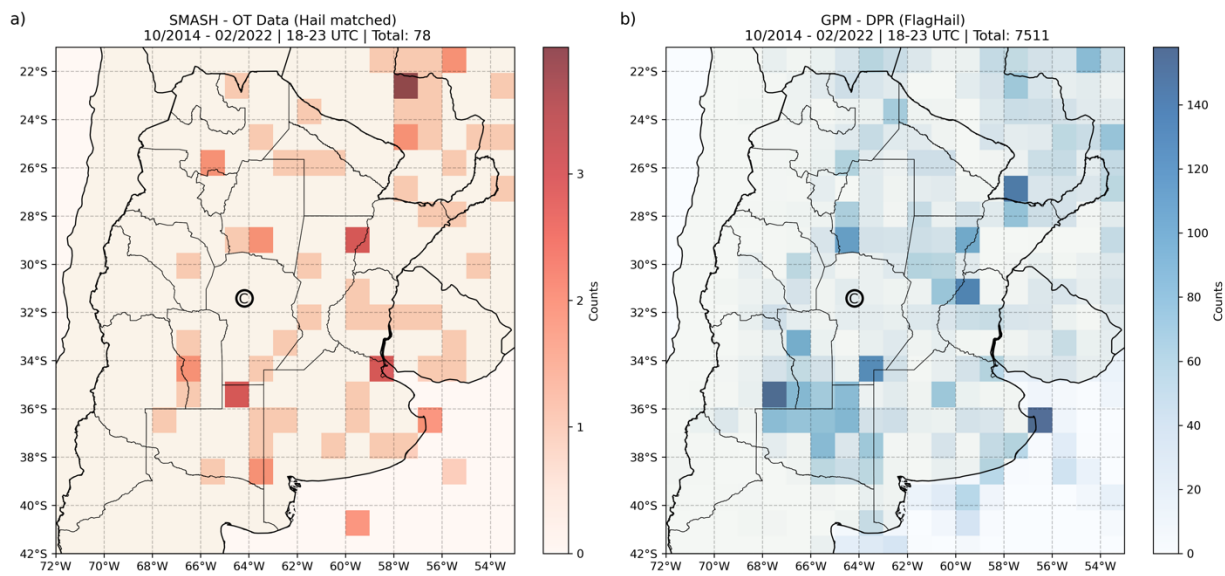


Figure 35: As in Figure 4.4 but for 18-23 UTC, 15-20 local time.

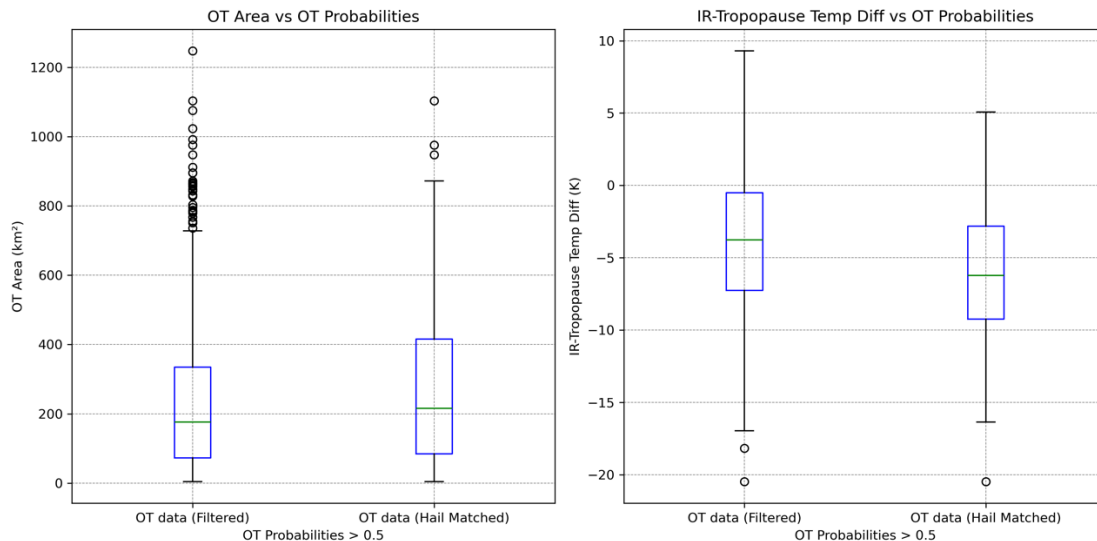


Figure 36: Comparison of OT characteristics between filtered ($n=1298$) and hail-matched ($n=189$) cases from October 2014 through February 2022. Left panel shows OT area distributions (km²). Right panel shows IR-tropopause temperature differences (K). Both panels include only OTs with probability values greater than 0.5. Box plots show median (green line), interquartile range (blue box), whiskers extending to 1.5 times the interquartile range, and outliers (black circles).

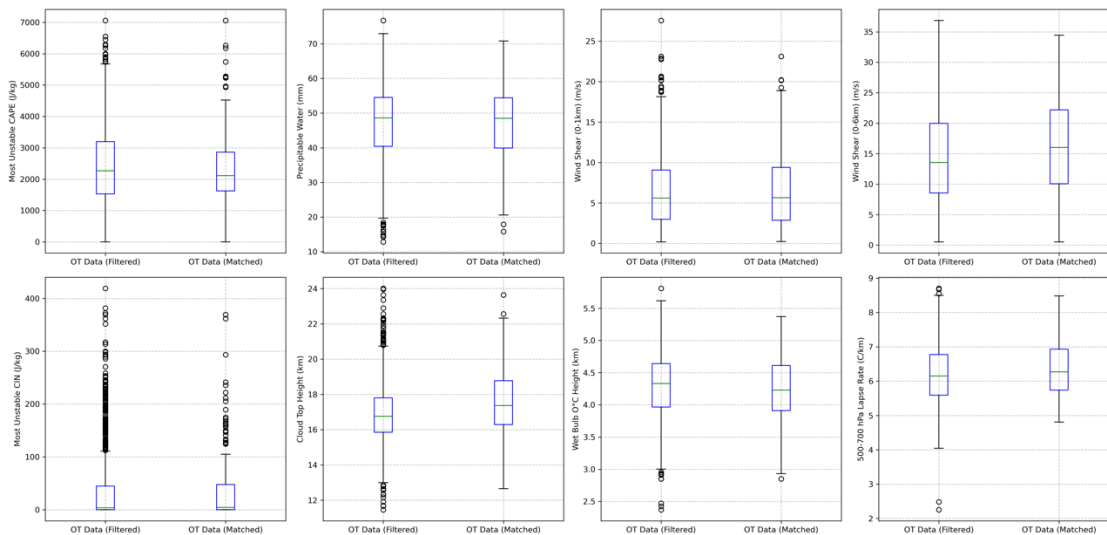


Figure 37: Comparison of environmental parameters between filtered ($n=1298$) and hail-matched ($n=189$) OT cases from October 2014 through February 2022. Parameters shown are: (a) MUCAPE (J/kg), (b) precipitable water (mm), (c) 0-3 km wind shear (m/s), (d) 0-6 km wind shear (m/s), (e) MUCIN (J/kg), (f) cloud top height (km), (g) wet bulb zero height (km), and (h) 500-700 hPa lapse rate (°C/km). Box plots show median (green line), interquartile range (blue box), whiskers extending to 1.5 times the interquartile range, and outliers (black circles). Note that filtered cases include both hail-matched and non-matched OTs.

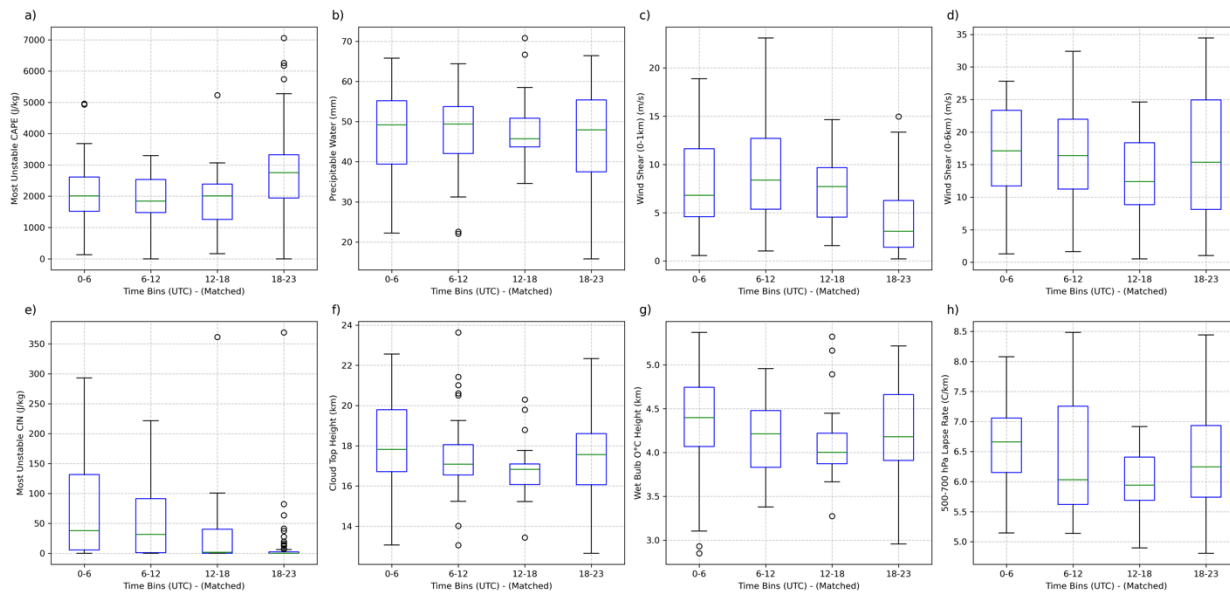


Figure 38: Diurnal variation of environmental parameters for hail-matched OTs across four time periods (0-6, 6-12, 12-18, and 18-23 UTC, where local time is UTC-3). Parameters and box plot lines are as in Figure 10. Sample sizes for each time period are: 0-6 UTC (52), 6-12 UTC (39), 12-18 UTC (20), and 18-23 UTC (78).

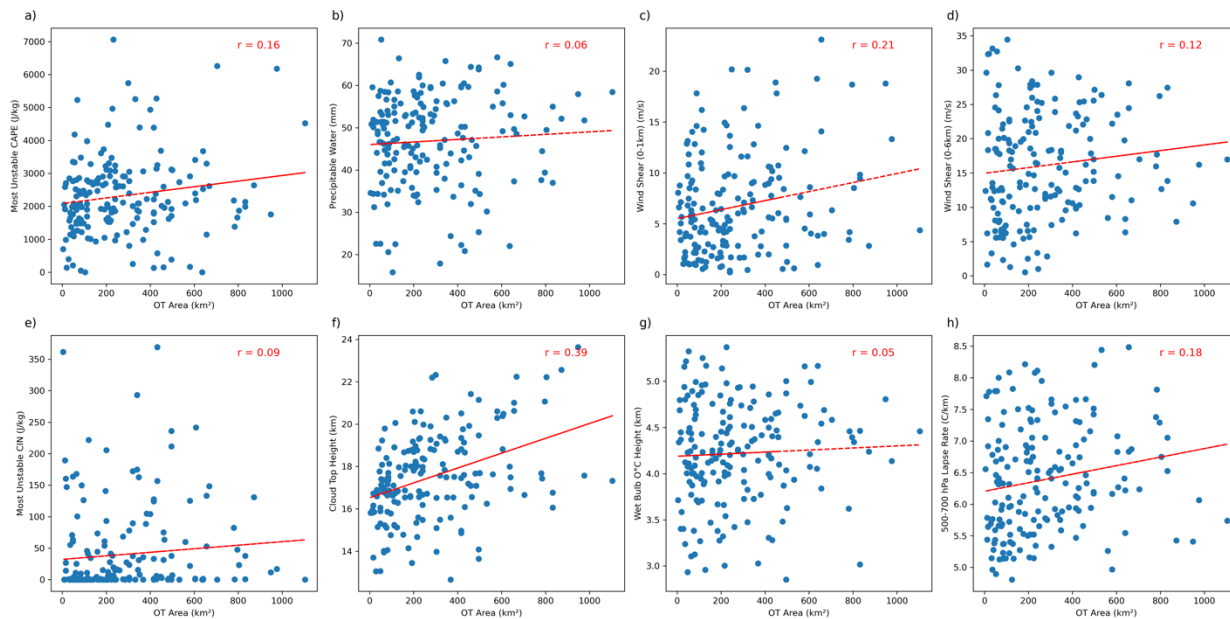


Figure 39: Scatterplots of environmental parameters as in Figure 4.10 as a function of OT area (km²) for hail-matched OTs (n=189). Each panel shows individual cases (blue dots), linear regression fit (red line), and correlation coefficient (r).

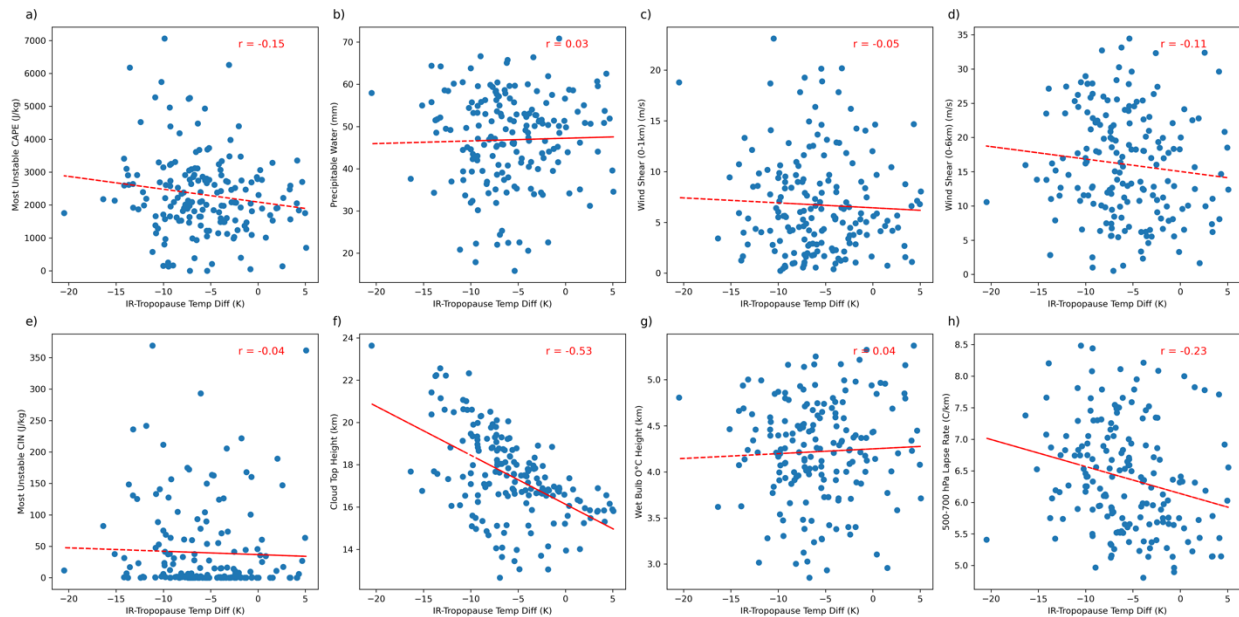


Figure 40: As in Figure 4.12 but for IR-Tropopause Temperature difference (K).

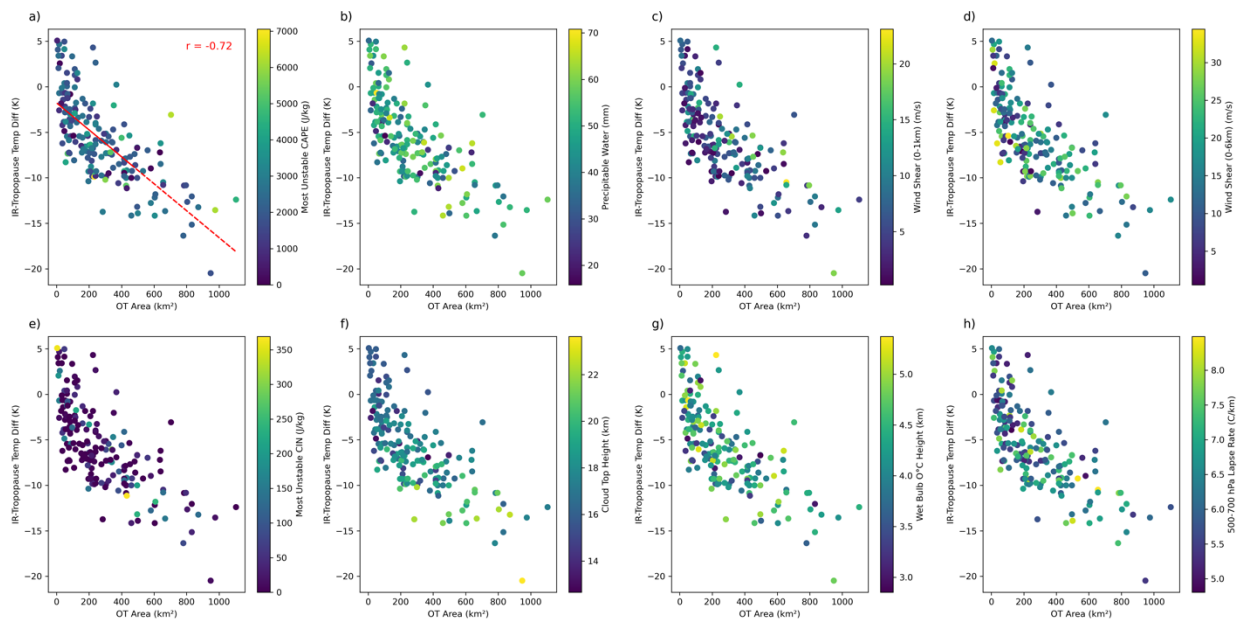


Figure 41: Multi-parameter analysis of relationships between OT characteristics and environmental conditions for hail-matched cases ($n=189$). Each panel shows OT area (x-axis, km²) versus IR-tropopause temperature difference (y-axis, K), with points colored by: (a) MUCAPE (J/kg), (b) precipitable water (mm), (c) 0-3 km wind shear (m/s), (d) 0-6 km wind shear (m/s), (e) MUCIN (J/kg), (f) cloud top height (km), (g) wet bulb zero height (km), and (h) 500-700 hPa lapse rate (°C/km). Each panel shows individual cases (color dots), linear regression fit (red line), and correlation coefficient (r).

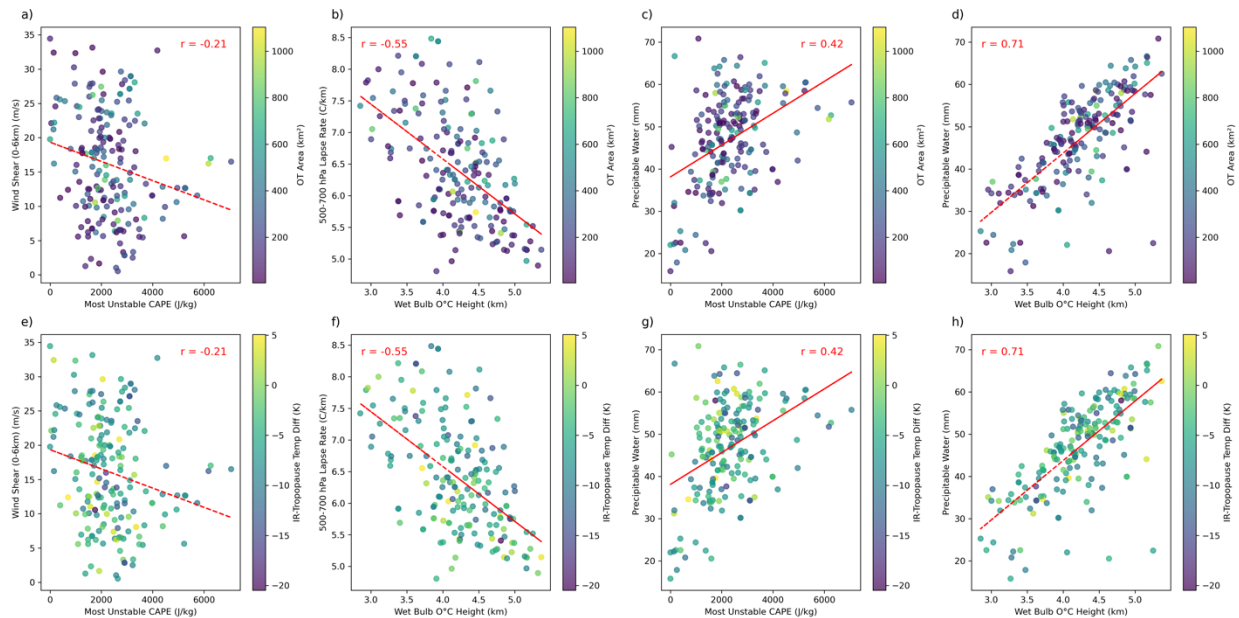


Figure 42: Correlations between environmental parameters for hail-matched cases ($n=189$), shown twice with different color coding. Top row (a-d) shows points colored by OT area (km²), while bottom row (e-h) shows points colored by IR-tropopause temperature difference (K). Relationships shown are: (a,e) MUCAPE vs 0-6 km wind shear, (b,f) wet bulb zero height vs 500-700 hPa lapse rate, (c,g) MUCAPE vs precipitable water, and (d,h) wet bulb zero height vs precipitable water. Each panel shows individual cases (color dots), linear regression fit (red line), and correlation coefficient (r).

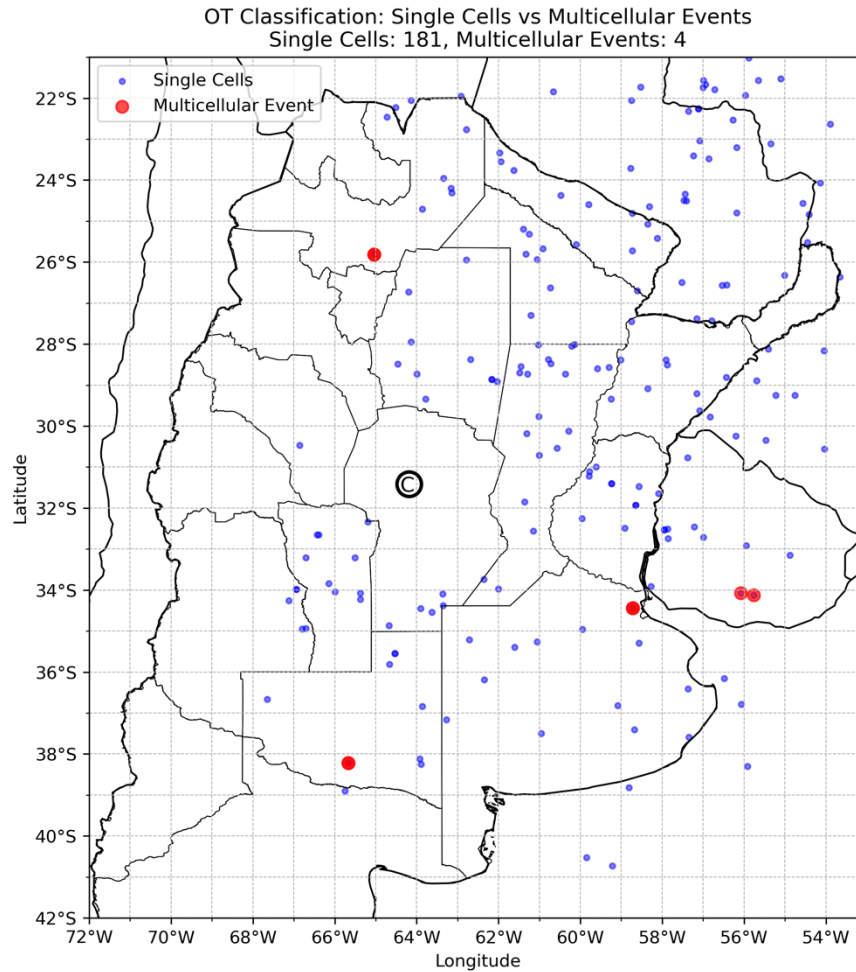


Figure 43: Spatial distribution of overshooting tops (OTs) classified as single-cell storms (blue dots, $n=181$) and multicellular events (red dots, $n=4$) across Argentina during 2014-2022. Cordoba city is marked with (C). Multicellular events are observed in four distinct locations: the central region (26°S), along the Uruguay border (34°S), and in southern Argentina (38°S).

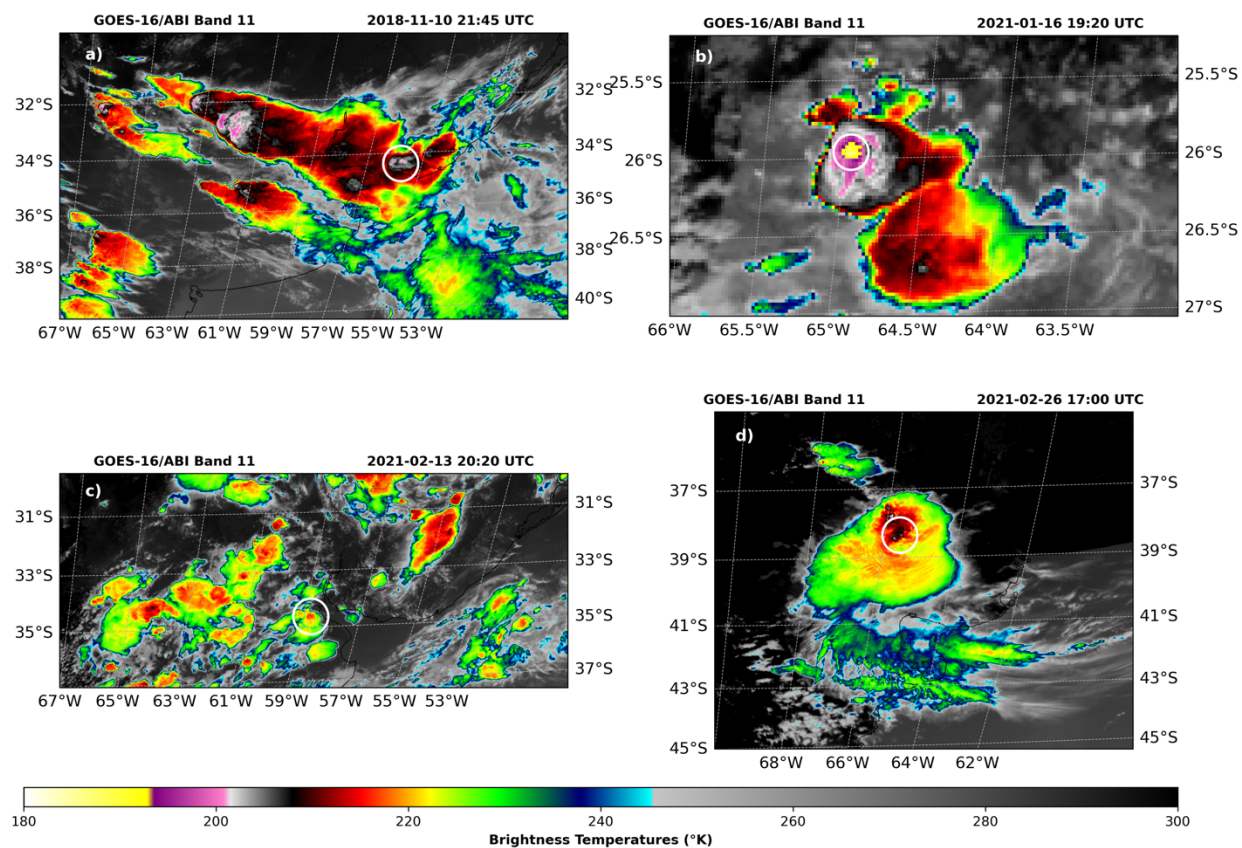


Figure 44: GOES-16 ABI Band 11 ($8.4 \mu\text{m}$) brightness temperature (K) observations showing OTs classified as multicellular as defined in the text. Images are from: a) November 10, 2018 at 21:45 UTC, b) January 16, 2021 at 19:20 UTC, c) February 13, 2021 at 20:20 UTC, and d) February 26, 2021 at 17:00 UTC. White circles highlight the location of the OTs of interest.

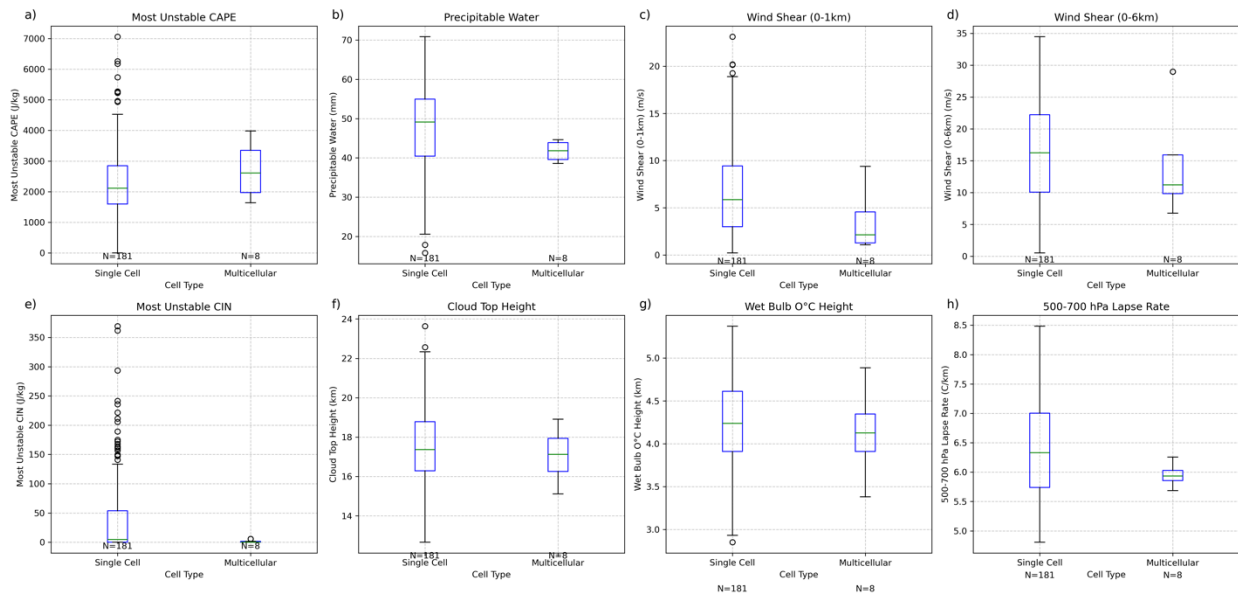


Figure 45: Comparison of environmental parameters between single-cell ($n=181$) and multicellular ($n=8$) events. Box plots show: (a) Most Unstable CAPE (J/kg), (b) Precipitable Water (mm), (c) 0-1 km Wind Shear (m/s), (d) 0-6 km Wind Shear (m/s), (e) Most Unstable CIN (J/kg), (f) Cloud Top Height (km), (g) Wet Bulb 0°C Height (km), and (h) 500-700 hPa Lapse Rate (°C/km).

Chapter 5

Conclusions and Future Work

5.1 Broader Motivation and Goals

Despite the significant impacts of hailstorms worldwide, fundamental gaps remain in our understanding of hail formation processes and the environmental conditions that support them, particularly in regions outside the U.S. The need to better understand these processes is especially critical in regions like Central Argentina, where traditional observational networks are sparse, yet some of the most intense storms occur. While laboratory studies, field observations, and numerical modeling have revealed much about the basic processes of hail formation, two key knowledge gaps motivated this research: first, the limited understanding of how particle characteristics influence hail formation in different regions, and second, the need to better characterize the environmental conditions that support hail production in apparently less favorable conditions than typically observed in U.S. storms. These limitations in our understanding become particularly evident when studying hail-producing storms in regions with unique environmental conditions or complex terrain.

This dissertation aimed to address these knowledge gaps through a multi-scale analysis of hail formation processes, focusing on central Argentina, a global hotspot for hail. The research uniquely combined new methodological approaches with satellite observations and environmental analysis to provide insights into hail formation and development, addressing fundamental questions while simultaneously developing new tools and frameworks for studying severe storms in traditionally under-observed regions.

5.2 Research Questions and Key Results

The dissertation was structured in three chapters based on three published or soon-to-be submitted papers, with key results of each summarized here.

Chapter 2 addressed the question: How can we preserve and analyze the spatial distribution of particles within hailstones to understand their formation processes? This methodological chapter introduced an innovative microscopy analysis technique that overcomes previous limitations related to melting hailstone samples. The key advance was the development of a method to preserve in situ non-soluble particles within hailstones using a protective porous plastic coating, combined with the application of both Confocal Laser Scanning Microscopy (CLSM) and Scanning Electron Microscopy with Energy-Dispersive Spectroscopy (SEM-EDS). The results demonstrated successful preservation of particles as small as 1 μm while maintaining their spatial distribution relative to the hailstone's growth layers. The technique therefore provided reliable results of particle distribution and spatial relationships across multiple hail samples, providing confidence in its application for detailed analysis of particles involved in the hail formation and growth processes.

Building on this methodological foundation, Chapter 3 investigated: What are the characteristics of particles within hailstones from different storm modes in Central Argentina, and what are their potential source regions? This chapter applied the newly developed microscopy technique in chapter 2 to analyze hailstones collected from two distinct storm types: a supercell (V-7) and a mesoscale convective system (NG-1). The analysis provided the first detailed characterization of

non-soluble particles in hailstones from South America, examining particle size distributions, elemental compositions, and their spatial distribution within the hailstone structure. Through combined microscopy analysis and air mass trajectory modeling, this study linked particle characteristics to specific regional sources and land use types.

Key findings revealed distinct particle characteristics between storm modes. The V-7 supercell hailstone (4-cm) contained particles ranging from 2-150 μm , with agglomerated mineral/organic particles (2-75 μm) and agglomerated salts (5-150 μm) dominant throughout. Notably, the largest particle (150 μm) was an agglomerated salt in the embryo, linked to a nearby dry lakebed. In contrast, the NG-1 MCS hailstone (8-cm) showed particles from 1-256 μm with greater compositional diversity. While also dominated by agglomerated mineral/organics (4-109 μm), it uniquely contained Cu-Zn-Cl-rich particles (6-78 μm) and larger lithics (up to 181 μm) potentially linked to agricultural practices and more distant source regions. These contrasting compositions aligned with their environmental conditions: V-7 formed in stronger deep-layer shear with local source influence, while NG-1 developed in weaker shear but higher MUCAPE conditions typical of Argentine MCS environments, with particle sources linked to broader regional transport.

Chapter 4 scaled up to examine: How do environmental conditions and storm-scale characteristics relate to hail production in Argentina? This analysis uniquely combined the SMASH OT dataset with GPM-DPR hail detections to investigate relationships between storm characteristics and their environments. The study implemented geometric correction techniques to accurately match observations from different satellite platforms, addressing a significant technical challenge in combining these datasets.

The analysis revealed distinct characteristics of hail-producing environments in Argentina. While some parameters like MUCAPE showed similar distributions between hail-matched and all filtered OT cases (2000-2500 J/kg), deep-layer shear in hail-matched cases (median ~16 m/s) exceeded filtered cases (median ~13 m/s). Though these shear values are generally lower than those typically associated with significant hail in the U.S. (Craven and Brooks 2004; Dennis and Kumjian 2017), the distributions show considerable overlap with a wide range of deep-layer shear values, consistent with the known variety of hail-producing storm modes in Argentina. Hail-producing OTs showed larger median areas (~225 km² versus ~175 km²) and deeper penetration into the tropopause (median -6K versus -4K) compared to all filtered OT cases. The study identified important relationships between OT characteristics and environmental conditions, with larger and deeper OTs occurring in environments characterized by higher moisture content and elevated wet bulb zero heights, particularly when combined with steeper mid-level lapse rates. The GPM-DPR FlagHail database showed the highest concentrations of hail occurrence in central Argentina, especially around the Sierras de Córdoba region, providing a more accurate representation of hail distribution compared to previous satellite-based climatologies that showed a northeastern bias in OT detections.

5.3 Synthesis of Physical Insights

The integration of findings across scales, from individual particles to storm environments, provides new insights into hail formation processes that both align with and challenge our current

understanding. This synthesis reveals both generalizable findings that likely apply across different regions and unique aspects specific to central Argentina's hail-producing storms.

The analysis revealed important connections between particle characteristics and storm-scale processes. The presence of large particles ($>100\ \mu\text{m}$) in hailstone embryos across different storm modes suggests that strong updrafts capable of supporting significant hail growth are not limited to supercellular convection in this region. This finding challenges the traditional U.S. centric view that links severe hail primarily to supercell thunderstorm environments. Instead, the results support that different storm modes can produce hail in Argentina when environmental conditions support appropriate combinations of updraft strength and duration, including in nocturnal MCSs that characterize this region near Córdoba.

The relationship between particle composition and storm environment proved particularly illuminating. In the supercell case (V-7), the dominance of local source regions aligned with environmental conditions showing strong upslope flow along the Sierras de Córdoba. In contrast, the MCS case (NG-1) showed influence from more distant sources, consistent with the presence of the SALLJ in its environment. These connections between particle sources and storm-scale flow patterns provide new insight into how different storm modes may access and incorporate potential INP. While these relationships were observed in Argentina, several key findings from this research have broader implications for understanding hail formation globally.

The relationship between OT characteristics and particle properties reveals critical connections between storm-scale dynamics and microphysical processes. Hail-producing OTs showed larger

areas ($\sim 225 \text{ km}^2$) and deeper penetration into the tropopause (median -6K) compared to non-hail cases, with a strong negative correlation ($r = -0.72$) between area and IR-tropopause temperature difference. These characteristics varied diurnally, with afternoon environments (18-23 UTC, peak MUCAPE $\sim 3000 \text{ J/kg}$) supporting discrete storms like the one in supercell 8 February, where local particle sources dominated. In contrast, early morning conditions (0-12 UTC) featured enhanced wind shear and stronger CIN, favoring organized systems like the MCS on 13-14 December that accessed more diverse and distant particle sources. This temporal pattern in storm organization and environmental conditions helps explain the observed differences in particle composition and size distributions between storm modes. Several factors affected our ability to match OTs with hail occurrence. The deep convection filter and >0.5 probability threshold for SMASH OTs ensured focus on the most intense updrafts. The 5-km matching radius balanced the need to account for potential updraft tilting while maintaining confident spatial association. The temporal matching criteria may have missed some relationships, as previous studies including Cintineo et al. 2020 and Bernal Ayala et al. 2022 showed strongest OT signatures often precede hail production. Future work should examine extended temporal windows to better capture this evolution.

These findings have important implications for future research approaches. The demonstrated importance of particle characteristics in hail formation suggests that models need to better represent the diversity of potential INP and their sources. The successful integration of satellite datasets provides a template for future remote sensing studies, particularly in regions with limited ground-based observations. However, the identified limitations in temporal sampling highlight the need for complementary observational approaches, including ground-based radar networks and in-situ measurements. These implications are particularly relevant given the complex interactions

observed between particle characteristics, storm environments, and terrain influences in central Argentina.

Several findings from this research likely apply beyond central Argentina. First, the prevalence of agglomerated mineral/organic particles in both analyzed hailstones suggests these may be particularly important for hail formation across different regions. The large size range of these particles (1 to 256 μm) and their presence throughout all hailstone layers indicates their role in nucleation, or simply how were they trapped during the growth phase. This finding builds off previous studies of ice nucleation on mineral dust and biological material (Lamb and Verlinde 2011; Vali et al. 2015), including those showing that organic-rich soil dust can serve as more efficient INPs than mineral desert dust (Steinke et al. 2016; Cornwell et al. 2024). Additionally, the influence of land use on particle sources represents another generalizable finding. The connection between agricultural regions and specific particle types (including agglomerated mineral/organics and various metallic compositions) suggests that land use patterns may significantly influence the availability of potential INPs. This relationship could be particularly important for understanding how changing land use practices might affect hail formation globally through their effects on available particle types and compositions. Furthermore, the identification of anthropogenic particles, including those potentially linked to agricultural chemicals, emphasizes the feedback between human activities and severe storm microphysics.

The relationship between particle size and its ability to serve as an ice-nucleating particle (INP) is complex and depends on multiple factors, including temperature, composition, and surface properties. Larger particles ($>10 \mu\text{m}$) generally exhibit higher ice-nucleating efficiency per unit

mass because they provide greater surface area and can host diverse mineral or organic phases that promote ice formation (Kiselev et al. 2017). This aligns with our findings of large particles (up to 256 μm) in hailstone embryos, which likely played a role in ice nucleation during hail formation (Bernal Ayala et al., 2024). These coarse particles likely remained suspended for extended periods in convective updrafts due to turbulent mixing, allowing them to aggregate with smaller aerosols and form composite INPs with enhanced nucleation activity (Testa et al., 2021). Their large surface area provided ample nucleation sites for ice formation even at modest supercooling temperatures (-10°C to -20°C), consistent with the temperature range observed in many convective storm systems (Chen et al. 2021). However, smaller particles ($<1 \mu\text{m}$) can dominate ice nucleation at colder temperatures or in environments rich in biological materials. Submicron INPs, such as bacterial fragments or fungal spores, are highly effective ice nucleators even at relatively warm temperatures (-10°C to -15°C), while fine mineral fragments like K-feldspar or quartz nanoparticles are efficient at colder temperatures (-20°C to -30°C) (DeMott et al., 2016; Chen et al., 2021; Beal et al., 2021). Additionally, submicron organic aerosols may modify the ice-nucleating efficiency of larger particles through coating effects, either enhancing or inhibiting their activity depending on the chemical interactions involved. Our method's 1 μm detection limit therefore introduces gaps in understanding certain aspects of hail formation. Therefore, integrating complementary techniques to detect submicron INPs would provide a more comprehensive understanding of the full spectrum of ice-nucleating processes.

The relationship between OT characteristics and hail production also appears generalizable. The finding in our 8-year database that hail-producing OTs show larger areas and deeper penetration into the tropopause suggests these characteristics could help identify potential hail-producing

storms globally. The negative correlation ($r = -0.72$) between OT area and IR-tropopause temperature difference indicates that larger OTs consistently achieve deeper penetration, likely reflecting stronger updrafts capable of supporting hail growth. These characteristics showed distinct patterns throughout the diurnal cycle, with the largest and deepest OTs occurring during afternoon hours (18-23 UTC) when MUCAPE peaked (~ 3000 J/kg), conditions typically favorable for discrete storms and supercells. In contrast, early morning hours (0-12 UTC) featured enhanced wind shear and stronger CIN values more linked to nocturnal organized multicellular systems in this region. This nocturnal hail production by MCSs represents a key difference from U.S. severe storms where significant hail is predominantly associated with afternoon/evening supercells. The ability of Argentine storms to produce hail across different modes and times explains why traditional environmental hail parameters show broader ranges than in U.S.-based studies. While afternoon discrete storms operate in environments similar to U.S. supercells, nocturnal MCSs produce hail under distinctly different conditions, particularly regarding deep-layer shear. The Sierras de Córdoba further modify these environments, suggesting that terrain interactions may help enhance favorable conditions promoting hail production from different storm modes near this unique mountain range.

The integration of OT characteristics with particle properties reveals a picture of hail formation processes across different storm modes and environments. In the supercell case (V-7), the dominance of local particle sources (including the $150\text{-}\mu\text{m}$ agglomerated salt from nearby dry lakebeds) aligned with afternoon OT development (18-23 UTC) characterized by strong upslope flow along the Sierras de Córdoba. This local influence was reflected in both the particle composition and the OT characteristics, with the storm developing in an environment of strong

deep-layer shear and moderate MUCAPE (~2000-2500 J/kg). In contrast, the MCS case (NG-1) demonstrated how broader regional transport patterns influence both particle characteristics and storm development. The presence of diverse particle types (including Cu-Zn-Cl-rich particles and larger lithics up to 181 μm) from agricultural regions coincided with nocturnal OT development (0-12 UTC) in an environment featuring enhanced wind shear and stronger CIN. These connections between particle sources, storm modes, and OT characteristics suggest that the spatial and temporal patterns of hail formation are fundamentally linked to both local and regional environmental conditions. The Sierras de Córdoba's influence on both particle transport and storm development further emphasizes how terrain can shape both the microphysical and storm-scale processes involved in hail formation. This integrated view helps explain why traditional environmental parameters show broader ranges in Argentina compared to U.S.-based studies, as different storm modes can access varying particle sources while developing under distinct environmental conditions.

5.4 Methodological Advances and Limitations

The research developed and implemented several innovative methodological approaches, each with potential for broader application but also important limitations that must be considered in future studies. The development of a new microscopy technique for analyzing hailstone particles represents a significant methodological advance. The method successfully addresses a long-standing challenge in hail research: preserving the spatial distribution of particles within hailstones while enabling detailed analysis of their characteristics. Through careful adaptation of the FORMVAR coating technique and controlled sublimation processes, the method maintains particle

spatial distribution while preventing contamination through precise temperature control. The technique successfully preserves particles as small as 1 μm , enabling unprecedented detail in analyzing hailstone composition and structure. The integration of CLSM and SEM-EDS techniques provides complementary capabilities, combining high-resolution imaging of particle morphology with detailed elemental composition analysis and three-dimensional reconstruction possibilities.

While our analysis didn't reveal dramatic differences in particle composition between embryo and outer layers, the value of our labor-intensive method lies in several key aspects that distinguish it from traditional approaches. First, our method uniquely preserves the spatial distribution of particles within hailstones, allowing us to definitively establish that large particles (1-256 μm) are present throughout the stone, including the embryo region. These findings challenge previous assumptions about particle size distributions in hail formation, which wouldn't be possible with traditional melting techniques. Previous studies like Michaud et al. (2014) and Šantl-Temkiv et al. (2013) could only analyze bulk compositions after melting, losing crucial spatial information about particle distribution and potentially missing relationships between particle location and growth processes.

Second, preserving spatial relationships enables us to understand the complete particle size spectrum across different regions of the hailstone. While earlier methods often focused on specific size ranges or particle types (e.g., Michaud et al.'s 2014 focus on particles $>0.2 \mu\text{m}$ in embryos), our approach captures the full range of non-soluble particles larger than 1 μm throughout the stone.

This view is essential for understanding how different particle populations contribute to hail formation and growth, even if their distributions are more uniform than initially hypothesized.

Third, our method's ability to analyze individual particles in situ provides details about particle characteristics that would be lost through melting or filtering techniques. This detailed analysis reveals how particles of various sizes and compositions can serve as an ice nuclei, contributing to our understanding of ice nucleation processes in clouds. The fact that we found similar particle characteristics throughout the stone suggests that the initial conditions for ice nucleation may persist throughout the growth process, a finding that wouldn't be apparent without our spatial preservation technique. These advantages justify our method's continued use and refinement, particularly when combined with complementary techniques like isotopic analysis or other microscopy methods that could provide additional insights into particle origins and ice formation processes. The method's value lies not just in identifying differences between regions but in providing a complete, spatially resolved picture of particle distributions that helps us understand the initial stages of hail formation.

While our method provided interpretation of particles down to the 1- μm detection limit, the potential interference from the glass substrate in EDS analysis requires careful consideration in data interpretation, particularly for the particles near the detection limit where background signals become more significant. Additionally, the technique's current implementation provides limited ability to distinguish between organic and inorganic carbon, an important distinction for understanding the role of biological particles in hail formation. The time-intensive nature of

individual particle analysis also limits the number of samples that can be processed, potentially affecting the statistical significance of findings.

Sample preparation presents additional challenges that must be considered. The method requires specialized cold room facilities and expertise in the complex coating process, limiting its immediate applicability to laboratories with appropriate infrastructure. The risk of sample damage during cutting and polishing necessitates careful handling and experienced technicians. Storage temperature requirements also pose logistical challenges, particularly when collecting samples in remote locations or during extended field campaigns.

The research advanced methods for combining different satellite datasets to study hail-producing storms, particularly in the integration of GOES series OT detections with GPM-DPR FlagHail data. The development and implementation of geometric correction algorithms, including both parallax and swath-edge displacement corrections, addressed potential spatial mismatches between datasets. Several key methodological choices affected our final matched dataset. The deep convection filter and >0.5 probability threshold for SMASH OTs ensured focus on the most intense updrafts but significantly reduced the sample size. The 5-km matching radius balanced the need to account for potential updraft tilting with maintaining confident spatial association between OTs and hail detection. While these strict criteria enhanced confidence in our matches, they likely excluded some valid cases.

Satellite data integration faces several important limitations. The temporal matching criteria may have missed key relationships, as previous studies, including Bernal Ayala et al. 2022, showed that

the strongest OT signatures often precede hail production. Future work should examine extended temporal windows to better capture this evolution. The limited GPM overpasses, occurring only twice daily at any given location, create challenges in capturing storm evolution and potentially under-sample multicellular systems. This temporal constraint particularly affects the identification of organized convective systems, which may evolve significantly between satellite passes. Additionally, spatial resolution differences between datasets (4/2 km for GOES-13/16 versus 5 km for GPM) and coverage gaps in polar-orbiting data create challenges in storm characterization. These limitations suggest the need for complementary observational approaches, particularly in regions where traditional ground-based networks are sparse.

Both the microscopy analysis and the need to validate satellite-based inferences of hail, highlight the value of citizen science programs in hail research, particularly through the “Cosecheros” program in Cordoba, Argentina. The development of standardized collection protocols, documentation procedures, and sample transfer methods enabled reliable scientific analysis of citizen-collected samples. The establishment of temperature control guidelines and verification procedures helped maintain sample integrity, while careful documentation standards ensured the scientific utility of collected samples. This framework demonstrates how community engagement can effectively support scientific research while providing valuable educational opportunities.

Nevertheless, citizen science programs face their own set of limitations. Spatial bias toward populated areas creates gaps in coverage, while temporal variations in participant engagement affect data consistency. Resource limitations can restrict program expansion, and variable storage conditions in participant homes may affect sample quality. Transportation challenges and potential

contamination risks require careful consideration in program design and implementation. Despite these limitations, the methodological advances developed in this research provide valuable frameworks for future studies, with significant implications for both scientific understanding and practical applications.

5.5 Future Directions

The microscopy-based methodology developed in this research could contribute to future hail research initiatives, particularly the upcoming NSF-funded Investigation of Convective Hail Producing Processes (ICECHIP) field campaign planned for Spring 2025 in the U.S. Central Plains. ICECHIP aims to advance understanding of hail formation through comprehensive environmental measurements, detailed storm-scale observations, and analysis of hailstone properties. The technique's ability to preserve spatial relationships between particles and growth layers could help validate hypotheses about embryo formation and growth trajectories, complementing ICECHIP's multi-scale observational approach. In particular, the potential integration of the microscopy technique with isotopic analysis during ICECHIP could help resolve current limitations in distinguishing particle types, particularly organic versus inorganic carbon. Additionally, the development of automated particle analysis techniques, potentially incorporating machine learning approaches, could address the time-intensive nature of current methods while maintaining analytical precision (Bernal Ayala et al. 2024). Furthermore, the expansion of citizen science programs, building on the COSECHEROS model in Argentina, could provide broader geographical coverage of hail observations while engaging communities in scientific research.

Looking beyond current initiatives, several longer-term research needs become apparent. The development of a global database of hailstone characteristics, combining particle analysis with environmental conditions and satellite inferences, would enable a more comprehensive understanding of regional variations in hail formation processes. Improved integration of multiple observational platforms, including new satellite sensors and ground-based networks, could address current limitations in temporal and spatial coverage. Advanced numerical modeling approaches could better represent the complex interactions involved in hail formation and growth, including how changing climate and land use patterns might affect severe storm characteristics in the future.

6 References

- Allen, J. T., M. K. Tippett, Y. Kaheil, A. H. Sobel, C. Lepore, S. Nong, and A. Muehlbauer, 2017: An Extreme Value Model for U.S. Hail Size. *Monthly Weather Review*, **145**, 4501–4519, <https://doi.org/10.1175/MWR-D-17-0119.1>.
- , I. M. Giammanco, M. R. Kumjian, H. Jurgen Punge, Q. Zhang, P. Groenemeijer, M. Kunz, and K. Ortega, 2020: Understanding Hail in the Earth System. *Reviews of Geophysics*, **58**, e2019RG000665, <https://doi.org/10.1029/2019RG000665>.
- Anderson, S. I., 2014: Characterisation of cells on biomaterial surfaces and tissue-engineered constructs using microscopy techniques. *Tissue Engineering Using Ceramics and Polymers (Second Edition)*, A.R. Boccaccini and P.X. Ma, Eds., Woodhead Publishing, 196–223, <https://doi.org/10.1533/9780857097163.2.196>.
- Arena, L., and A. Crespo, 2019: Recopilación de estudios primarios de caracterización cristalográfica de granizos y de las tormentas que los originan.
- Arena, L. E., 2020: Granizos Gigantes de Córdoba-Argentina I. El Coloso Victoria.
- , 2022: Cosecheros. *Argentina.gob.ar*. Accessed 27 October 2023, <https://www.argentina.gob.ar/ciencia/sact/ciencia-ciudadana/cosecheros-de-granizo-cordoba>.
- Arena, L. E., 2024: Identificación de partículas incluidas en hielos naturales (glaciares, permafrost, granizo) por sublimación adaptada. *ANALES AFA*, **35**, 25–27, <https://doi.org/10.31527/analesafa.2024.35.2.25>.
- Ashbaugh, L. L., W. C. Malm, and W. Z. Sadeh, 1985: A residence time probability analysis of sulfur concentrations at grand Canyon national park. *Atmospheric Environment*, **19**, 1263–1270.
- Bal, S. K., S. Saha, B. B. Fand, N. P. Singh, J. Rane, and P. S. Minhas, 2014: *Hailstorm: Causes, Damage and POst-hail Management in Agriculture*. National Institute of Abiotic Stress Management.
- Bang, S. D., and D. J. Cecil, 2019: Constructing a Multifrequency Passive Microwave Hail Retrieval and Climatology in the GPM Domain. *Journal of Applied Meteorology and Climatology*, **58**, 1889–1904, <https://doi.org/10.1175/JAMC-D-19-0042.1>.
- Battaglia, A., K. Mroz, and D. Cecil, 2022: Chapter 9 - Satellite hail detection. *Precipitation Science*, S. Michaelides, Ed., Elsevier, 257–286, <https://doi.org/10.1016/B978-0-12-822973-6.00006-8>.
- Beal, A., L. D. Martins, J. A. Martins, A. P. Rudke, D. S. de Almeida, L. M. Costa, and C. R. T. Tarley, 2021: Evaluation of the chemical composition of hailstones from triple border

- Paraná, Santa Catarina (Brazil) and Argentina. *Atmospheric Pollution Research*, **12**, 184–192, <https://doi.org/10.1016/j.apr.2021.01.009>.
- Bedka, K., J. Brunner, R. Dworak, W. Feltz, J. Otkin, and T. Greenwald, 2010: Objective Satellite-Based Detection of Overshooting Tops Using Infrared Window Channel Brightness Temperature Gradients. *Journal of Applied Meteorology and Climatology*, **49**, 181–202, <https://doi.org/10.1175/2009JAMC2286.1>.
- Bern, A. M., H. A. Lowers, G. P. Meeker, and J. A. Rosati, 2009: Method Development for Analysis of Urban Dust Using Scanning Electron Microscopy with Energy Dispersive X-ray Spectrometry to Detect the Possible Presence of World Trade Center Dust Constituents. *Environ. Sci. Technol.*, **43**, 1449–1454, <https://doi.org/10.1021/es800865n>.
- Bernal Ayala, A. C., A. K. Rowe, L. E. Arena, and A. R. Desai, 2022: Evaluation of Satellite-Derived Signatures for Three Verified Hailstorms in Central Argentina. *Meteorology*, **1**, 183–210, <https://doi.org/10.3390/meteorology1020013>.
- , J. J. Gerth, T. J. Schmit, S. S. Lindstrom, and J. P. Nelson, 2023: Parallax Shift in GOES ABI Data. *JOM*, <https://doi.org/10.15191/nwajom.2023.1102>.
- , A. K. Rowe, L. E. Arena, and W. O. Nachlas, 2024a: Physical-chemical properties of particles in hailstones from Central Argentina. *EGUsphere*, 1–32, <https://doi.org/10.5194/egusphere-2024-3215>.
- , ———, ———, ———, and M. L. Asar, 2024b: Exploring non-soluble particles in hailstones through innovative confocal laser and scanning electron microscopy techniques. *Atmospheric Measurement Techniques*, **17**, 5561–5579, <https://doi.org/10.5194/amt-17-5561-2024>.
- Blair, S. F., and Coauthors, 2017: High-Resolution Hail Observations: Implications for NWS Warning Operations. *WEATHER FORECAST*, **32**, 1101–1119, <https://doi.org/10.1175/WAF-D-16-0203.1>.
- Borda, L. G., N. J. Cosentino, L. A. Iturri, M. G. García, and D. M. Gaiero, 2022: Is Dust Derived From Shrinking Saline Lakes a Risk to Soil Sodification in Southern South America? *Journal of Geophysical Research: Earth Surface*, **127**, e2021JF006585, <https://doi.org/10.1029/2021JF006585>.
- Brostrøm, A., K. I. Kling, K. S. Hougaard, and K. Mølhav, 2020: Complex Aerosol Characterization by Scanning Electron Microscopy Coupled with Energy Dispersive X-ray Spectroscopy. *Sci Rep*, **10**, 9150, <https://doi.org/10.1038/s41598-020-65383-5>.
- Browning, K. A., and G. B. Foote, 1976: Airflow and hail growth in supercell storms and some implications for hail suppression. *Quarterly Journal of the Royal Meteorological Society*, **102**, 499–533, <https://doi.org/10.1002/qj.49710243303>.

- Bruick, Z. S., K. L. Rassumen, and D. J. Cecil, 2019: Subtropical South American Hailstorm Characteristics and Environments. *Mon. Weather Rev.*, **147**, 4289–4304, <https://doi.org/10.1175/MWR-D-19-0011.1>.
- Burrows, S. M., and Coauthors, 2022: Ice-Nucleating Particles That Impact Clouds and Climate: Observational and Modeling Research Needs. *Reviews of Geophysics*, **60**, e2021RG000745, <https://doi.org/10.1029/2021RG000745>.
- Cecil, D. J., and C. B. Blankenship, 2012: Toward a Global Climatology of Severe Hailstorms as Estimated by Satellite Passive Microwave Imagers. *JCLI*, **25**, 687–703, <https://doi.org/10.1175/JCLI-D-11-00130.1>.
- Changnon, S. A., 2008: Temporal and Spatial Distributions of Damaging Hail in the Continental United States. *Physical Geography*, **29**, 341–350, <https://doi.org/10.2747/0272-3646.29.4.341>.
- Chen, J., Z. Wu, J. Chen, N. Reicher, X. Fang, Y. Rudich, and M. Hu, 2021: Size-resolved atmospheric ice-nucleating particles during East Asian dust events. *Atmos. Chem. Phys.*, **21**, 3491–3506, <https://doi.org/10.5194/acp-21-3491-2021>.
- Christner, B. C., J. A. Mikucki, C. M. Foreman, J. Denson, and J. C. Priscu, 2005: Glacial ice cores: A model system for developing extraterrestrial decontamination protocols. *Icarus*, **174**, 572–584, <https://doi.org/10.1016/j.icarus.2004.10.027>.
- Cintineo, J. L., M. J. Pavolonis, J. M. Sieglaff, L. Cronic, and J. Brunner, 2020: NOAA ProbSevere v2.0—ProbHail, ProbWind, and ProbTor. *Weather and Forecasting*, **35**, 1523–1543, <https://doi.org/10.1175/WAF-D-19-0242.1>.
- Claquin, T., M. Schulz, and Y. J. Balkanski, 1999: Modeling the mineralogy of atmospheric dust sources. *Journal of Geophysical Research: Atmospheres*, **104**, 22243–22256, <https://doi.org/10.1029/1999JD900416>.
- Claxton, N. S., T. J. Fellers, and M. W. Davidson, 2006: Microscopy, Confocal. *Encyclopedia of Medical Devices and Instrumentation*, John Wiley & Sons, Ltd, <https://doi.org/10.1002/0471732877.emd291>.
- Conen, F., C. E. Morris, J. Leifeld, M. V. Yakutin, and C. Alewell, 2011: Biological residues define the ice nucleation properties of soil dust. *Atmospheric Chemistry and Physics*, **11**, 9643–9648, <https://doi.org/10.5194/acp-11-9643-2011>.
- Conny, J. M., R. D. Willis, and D. L. Ortiz-Montalvo, 2019: Analysis and Optical Modeling of Individual Heterogeneous Asian Dust Particles Collected at Mauna Loa Observatory. *Journal of Geophysical Research: Atmospheres*, **124**, 2702–2723, <https://doi.org/10.1029/2018JD029387>.
- Copernicus Climate Change Service, 2019: Land cover classification gridded maps from 1992 to present derived from satellite observation. Copernicus Climate Change Service (C3S)

- Climate Data Store (CDS), accessed 29 March 2023, <https://doi.org/10.24381/cds.006f2c9a>.
- Cornwell, G. C., and Coauthors, 2024: Enrichment of Phosphates, Lead, and Mixed Soil-Organic Particles in INPs at the Southern Great Plains Site. *Journal of Geophysical Research: Atmospheres*, **129**, e2024JD040826, <https://doi.org/10.1029/2024JD040826>.
- Craven, J. P., and H. Brooks, 2004: Baseline climatology of sounding derived parameters associated with deep, moist convection. *Natl. Wea. Dig.*, **28**, 13–24.
- Crespo, A., 2020: Characterization of two hailstorms in Argentina. University of Wisconsin-Madison, <https://search.library.wisc.edu/catalog/9913080671002121>.
- Cziczo, D. J., and Coauthors, 2009: Inadvertent climate modification due to anthropogenic lead. *Nature Geoscience*, **2**, 333–336, <https://doi.org/10.1038/ngeo499>.
- Dahal, S., 2022: The Essential Guide to Raman Microscopy. *Advancing Materials*. Accessed 16 August 2023, <https://www.thermofisher.com/blog/materials/guide-to-raman-microscopy-raman-spectroscopy/>.
- Das, P., 1962: Influence of Wind Shear on the Growth of Hail. *Journal of Atmospheric Sciences*, **19**, 407–414, [https://doi.org/10.1175/1520-0469\(1962\)019<0407:IOWSOT>2.0.CO;2](https://doi.org/10.1175/1520-0469(1962)019<0407:IOWSOT>2.0.CO;2).
- DeMott, P. J., and Coauthors, 2010: Predicting global atmospheric ice nuclei distributions and their impacts on climate. *Proc Natl Acad Sci U S A*, **107**, 11217–11222, <https://doi.org/10.1073/pnas.0910818107>.
- DeMott, P. J., and Coauthors, 2016: Sea spray aerosol as a unique source of ice nucleating particles. *Proceedings of the National Academy of Sciences*, **113**, 5797–5803, <https://doi.org/10.1073/pnas.1514034112>.
- Demšar, J., and Coauthors, 2013: Orange: Data Mining Toolbox in Python. *J. Mach. Learn. Res.*, **14**, 2349–2353.
- Dennis, E. J., and M. R. Kumjian, 2017: The Impact of Vertical Wind Shear on Hail Growth in Simulated Supercells. *JAS*, **74**, 641–663, <https://doi.org/10.1175/JAS-D-16-0066.1>.
- Di Biagio, C., Y. Balkanski, S. Albani, O. Boucher, and P. Formenti, 2020: Direct Radiative Effect by Mineral Dust Aerosols Constrained by New Microphysical and Spectral Optical Data. *Geophysical Research Letters*, **47**, e2019GL086186, <https://doi.org/10.1029/2019GL086186>.
- Dial, G. L., J. P. Racy, and R. L. Thompson, 2010: Short-Term Convective Mode Evolution along Synoptic Boundaries. *Weather and Forecasting*, **25**, 1430–1446, <https://doi.org/10.1175/2010WAF2222315.1>.
- Diep, T., and Coauthors, 2022: Chemical Composition and Immersion Freezing Activities of Aerosol Articles in the European Arctic. **2022**, A12P-1305.

- Donavon, R. A., and K. A. Jungbluth, 2007: Evaluation of a Technique for Radar Identification of Large Hail across the Upper Midwest and Central Plains of the United States. *Weather and Forecasting*, **22**, 244–254, <https://doi.org/10.1175/WAF1008.1>.
- Drouin, D., A. R. Couture, D. Joly, X. Tastet, V. Aimez, and R. Gauvin, 2007: CASINO V2.42: a fast and easy-to-use modeling tool for scanning electron microscopy and microanalysis users. *Scanning*, **29**, 92–101, <https://doi.org/10.1002/sca.20000>.
- Elliott, A. D., 2020: Confocal Microscopy: Principles and Modern Practices. *Curr Protoc Cytom*, **92**, e68, <https://doi.org/10.1002/cpcy.68>.
- Espeche, M. J., and R. Lira, 2022: Ecanndrewsite (ZnTiO₃) in Amphibolites, Sierras de Córdoba, Argentina: Mineral Chemistry and Comparison with Different Worldwide Paragenetic Occurrences. *The Canadian Mineralogist*, **60**, 677–686, <https://doi.org/10.3749/canmin.2100055>.
- Fallica, R., B. Watts, B. Rösner, G. D. Giustina, L. Brigo, G. Brusatin, and Y. Ekinici, 2018: Changes in the near edge x-ray absorption fine structure of hybrid organic–inorganic resists upon exposure. *Nanotechnology*, **29**, 36LT03, <https://doi.org/10.1088/1361-6528/aaccd4>.
- Farber, L., 2019: Microstructure and Mechanical Properties of Granules Formed in High Shear Wet Granulation. *Handbook of Pharmaceutical Wet Granulation*, A.S. Narang and S.I.F. Badawy, Eds., Academic Press, 37–88, <https://doi.org/10.1016/B978-0-12-810460-6.00003-8>.
- Field, P. R., and Coauthors, 2017: Secondary Ice Production: Current State of the Science and Recommendations for the Future, <https://doi.org/10.1175/AMSMONOGRAPHIS-D-16-0014.1>.
- Filmetrics, Inc., 2017: ProfilmOnline 3D imaging and analysis software.
- Fletcher, C., 2011: Physical geology : the science of Earth.
- FMC Argentina,: ZINC 700. Accessed 19 September 2024, <http://www.fmcargentina.com.ar/productos/zinc-700/>.
- Foote, A. G. B., and A. C. Knight, 1977: Hail: A Review of Hail Science and Hail Suppression. *AMS*.
- Fu, Y.-Z., Y.-D. Li, Y.-T. Su, C.-Y. Cai, and D.-Y. Huang, 2021: Application of confocal laser scanning microscopy to the study of amber bioinclusions. *Palaeoentomology*, **4**, 266–278, <https://doi.org/10.11646/palaeoentomology.4.3.14>.
- Galligani, V. S., S. D. Bang, M. Cancelada, P. Salio, H. Bechis, R. Mezher, and A. Granato, 2024: Testing a spaceborne passive-microwave severe hail retrieval over Argentina using ground-based dual-polarization radar data. *Quarterly Journal of the Royal Meteorological Society*, **150**, 5127–5145, <https://doi.org/10.1002/qj.4861>.

- Gao, K., C.-W. Zhou, E. J. B. Meier, and Z. A. Kanji, 2022: Laboratory studies of ice nucleation onto bare and internally mixed soot–sulfuric acid particles. *Atmospheric Chemistry and Physics*, **22**, 5331–5364, <https://doi.org/10.5194/acp-22-5331-2022>.
- Gelaro, R., and Coauthors, 2017: The Modern-Era Retrospective Analysis for Research and Applications, Version 2 (MERRA-2), <https://doi.org/10.1175/JCLI-D-16-0758.1>.
- Gensini, V. A., W. S. Ashley, A. C. Michaelis, A. M. Haberlie, J. Goodin, and B. C. Wallace, 2024: Hailstone size dichotomy in a warming climate. *npj Clim Atmos Sci*, **7**, 1–10, <https://doi.org/10.1038/s41612-024-00728-9>.
- Giordani, A., M. Kunz, K. M. Bedka, H. J. Punge, T. Paccagnella, V. Pavan, I. M. L. Cerenzia, and S. Di Sabatino, 2024: Characterizing hail-prone environments using convection-permitting reanalysis and overshooting top detections over south-central Europe. *Natural Hazards and Earth System Sciences*, **24**, 2331–2357, <https://doi.org/10.5194/nhess-24-2331-2024>.
- Goldstein, J. I., D. E. Newbury, J. R. Michael, N. W. M. Ritchie, J. H. J. Scott, and D. C. Joy, 2017: *Scanning Electron Microscopy and X-Ray Microanalysis*. Springer 554pp.
- Grenier, J.-C., and P. A. Sadok Zair, 1983: Hailstone Growth Trajectories in the Dynamic Evolution of a Moderate Hailstorm. *Journal of Applied Meteorology and Climatology*, **22**, 1008–1021, [https://doi.org/10.1175/1520-0450\(1983\)022<1008:HGTITD>2.0.CO;2](https://doi.org/10.1175/1520-0450(1983)022<1008:HGTITD>2.0.CO;2).
- Grover, M. A., 2021: Estimating Midlevel Updraif characteristics and severe weather intensity through the lens of overshooting tops. University of Illinois at Urbana-Champaign, <https://www.ideals.illinois.edu/items/118424>.
- Gu, L., N. Wang, X. Tang, and H. G. Changela, 2020: Application of FIB-SEM Techniques for the Advanced Characterization of Earth and Planetary Materials. *Scanning*, **2020**, 8406917, <https://doi.org/10.1155/2020/8406917>.
- Gunturi, P., and M. K. Tippett, 2017: *Managing severe thunderstorm risk: Impact of ENSO on U.S. tornado and hail frequencies*. Willis Re.
- Gutierrez, R. E., and M. R. Kumjian, 2021: Environmental and Radar Characteristics of Gargantuan Hail–Producing Storms. *Monthly Weather Review*, **149**, 2523–2538, <https://doi.org/10.1175/MWR-D-20-0298.1>.
- Hersbach, H., and Coauthors, 2020: The ERA5 global reanalysis. *Quarterly Journal of the Royal Meteorological Society*, **146**, 1999–2049, <https://doi.org/10.1002/qj.3803>.
- Heymsfield, A. J., and J. C. Pflaum, 1985: A Quantitative Assessment of the Accuracy of Techniques for Calculating Graupel Growth. *Journal of Atmospheric Sciences*, **42**, 2264–2274, [https://doi.org/10.1175/1520-0469\(1985\)042<2264:AQAOTA>2.0.CO;2](https://doi.org/10.1175/1520-0469(1985)042<2264:AQAOTA>2.0.CO;2).
- Higuchi, K., 1958: The etching of ice crystals. *Acta Metallurgica*, **6**, 636–642, [https://doi.org/10.1016/0001-6160\(58\)90157-3](https://doi.org/10.1016/0001-6160(58)90157-3).

- Higuchi, K., and J. Muguruma, 1958: *Etching of ice crystals by the use of plastic replica film*. Journal of the Faculty of Science.
- Holden, M. A., J. M. Campbell, F. C. Meldrum, B. J. Murray, and H. K. Christenson, 2021: Active sites for ice nucleation differ depending on nucleation mode. *Proceedings of the National Academy of Sciences*, **118**, e2022859118, <https://doi.org/10.1073/pnas.2022859118>.
- Hoose, C., and O. Möhler, 2012: Heterogeneous ice nucleation on atmospheric aerosols: a review of results from laboratory experiments. *Atmospheric Chemistry and Physics*, **12**, 9817–9854, <https://doi.org/10.5194/acp-12-9817-2012>.
- Huang, Y., J. F. Kok, K. Kandler, H. Lindqvist, T. Nousiainen, T. Sakai, A. Adebisi, and O. Jokinen, 2020: Climate Models and Remote Sensing Retrievals Neglect Substantial Desert Dust Asphericity. *Geophysical Research Letters*, **47**, e2019GL086592, <https://doi.org/10.1029/2019GL086592>.
- II, D. J. G., S. E. Haupt, D. W. Nychka, and G. Thompson, 2019: Interpretable Deep Learning for Spatial Analysis of Severe Hailstorms. *Monthly Weather Review*, **147**, 2827–2845, <https://doi.org/10.1175/MWR-D-18-0316.1>.
- International Code Council, 2008: *International Building Code - Structural*. International Code Council, <https://www.iccsafe.org/cs/codes/Documents/2007-08cycle/FAA/IBC-S1-S141-P2.pdf>.
- International Trade Administration, 2023: Argentina - Mining. Accessed 19 September 2024, <https://www.trade.gov/country-commercial-guides/argentina-mining>.
- Iturri, L. A., R. Funk, M. Leue, M. Sommer, and D. E. Buschiazzi, 2017: Wind sorting affects differently the organo-mineral composition of saltating and particulate materials in contrasting texture agricultural soils. *Aeolian Research*, **28**, 39–49, <https://doi.org/10.1016/j.aeolia.2017.07.005>.
- Jeong, G. Y., and T. Nousiainen, 2014: TEM analysis of the internal structures and mineralogy of Asian dust particles and the implications for optical modeling. *Atmospheric Chemistry and Physics*, **14**, 7233–7254, <https://doi.org/10.5194/acp-14-7233-2014>.
- , J. Y. Kim, J. Seo, G. M. Kim, H. C. Jin, and Y. Chun, 2014: Long-range transport of giant particles in Asian dust identified by physical, mineralogical, and meteorological analysis. *Atmospheric Chemistry and Physics*, **14**, 505–521, <https://doi.org/10.5194/acp-14-505-2014>.
- Jeong, G. Y., M. Y. Park, K. Kandler, T. Nousiainen, and O. Kempainen, 2016: Mineralogical properties and internal structures of individual fine particles of Saharan dust. *Atmospheric Chemistry and Physics*, **16**, 12397–12410, <https://doi.org/10.5194/acp-16-12397-2016>.
- Jeong, J.-H., J. Fan, C. R. Homeyer, and Z. Hou, 2020: Understanding Hailstone Temporal Variability and Contributing Factors over the U.S. Southern Great Plains. *Journal of Climate*, **33**, 3947–3966, <https://doi.org/10.1175/JCLI-D-19-0606.1>.

- Jiang, F., B. Chen, F. Qiao, R. Wang, C. Wei, and Q. Liu, 2023: Effects of Microphysics Parameterizations on Forecasting a Severe Hailstorm of 30 April 2021 in Eastern China. *Atmosphere*, **14**, 526, <https://doi.org/10.3390/atmos14030526>.
- Kandler, K., and Coauthors, 2007: Chemical composition and complex refractive index of Saharan Mineral Dust at Izaña, Tenerife (Spain) derived by electron microscopy. *Atmospheric Environment*, **41**, 8058–8074, <https://doi.org/10.1016/j.atmosenv.2007.06.047>.
- Kaye, T. G., and Coauthors, 2015: Laser-Stimulated Fluorescence in Paleontology. *PLoS One*, **10**, e0125923, <https://doi.org/10.1371/journal.pone.0125923>.
- Kemppinen, O., T. Nousiainen, and G. Y. Jeong, 2015: Effects of dust particle internal structure on light scattering. *Atmospheric Chemistry and Physics*, **15**, 12011–12027, <https://doi.org/10.5194/acp-15-12011-2015>.
- Ketterer, M. E., 2010: Geology and Mineralogy Applications of Atomic Spectroscopy. *Encyclopedia of Spectroscopy and Spectrometry (Second Edition)*, J.C. Lindon, Ed., Academic Press, 757–761, <https://doi.org/10.1016/B978-0-12-374413-5.00004-X>.
- Kiselev, A., F. Bachmann, P. Pedevilla, S. J. Cox, A. Michaelides, D. Gerthsen, and T. Leisner, 2017: Active sites in heterogeneous ice nucleation, the example of K-rich feldspars. *Science*, **355**, 367–371, <https://doi.org/10.1126/science.aai8034>.
- Knight, C. A., and N. C. Knight, 1970: Hailstone Embryos. *J ATMOS SCI*, **27**, 659–666.
- , and ———, 2001: Hailstorms. *Severe Convective Storms*, C.A. Doswell, Ed., American Meteorological Society, 223–254, https://doi.org/10.1007/978-1-935704-06-5_6.
- Koga, D., S. Kusumi, M. Shibata, and T. Watanabe, 2021: Applications of Scanning Electron Microscopy Using Secondary and Backscattered Electron Signals in Neural Structure. *Frontiers in Neuroanatomy*, **15**.
- Kozjek, M., and Coauthors, 2023: Dissecting giant hailstones: A glimpse into the troposphere with its diverse bacterial communities and fibrous microplastics. *Sci Total Environ*, **856**, 158786, <https://doi.org/10.1016/j.scitotenv.2022.158786>.
- Krueger, B. J., V. H. Grassian, J. P. Cowin, and A. Laskin, 2004: Heterogeneous chemistry of individual mineral dust particles from different dust source regions: the importance of particle mineralogy. *Atmospheric Environment*, **38**, 6253–6261, <https://doi.org/10.1016/j.atmosenv.2004.07.010>.
- Kubota, R., K. Nakamura, S. Torigoe, and I. Hamachi, 2020: The Power of Confocal Laser Scanning Microscopy in Supramolecular Chemistry: In situ Real-time Imaging of Stimuli-Responsive Multicomponent Supramolecular Hydrogels. *ChemistryOpen*, **9**, 67–79, <https://doi.org/10.1002/open.201900328>.

- Kumjian, M. R., and K. Lombardo, 2020: A Hail Growth Trajectory Model for Exploring the Environmental Controls on Hail Size: Model Physics and Idealized Tests. *Journal of the Atmospheric Sciences*, **77**, 2765–2791, <https://doi.org/10.1175/JAS-D-20-0016.1>.
- , Z. J. Lebo, and A. M. Ward, 2019a: Storms Producing Large Accumulations of Small Hail. *Journal of Applied Meteorology and Climatology*, **58**, 341–364, <https://doi.org/10.1175/JAMC-D-18-0073.1>.
- , ———, and ———, 2019b: Storms Producing Large Accumulations of Small Hail. *Journal of Applied Meteorology and Climatology*, **58**, 341–364, <https://doi.org/10.1175/JAMC-D-18-0073.1>.
- , and Coauthors, 2020: Gargantuan Hail in Argentina. *Bulletin of the American Meteorological Society*, **101**, E1241–E1258, <https://doi.org/10.1175/BAMS-D-19-0012.1>.
- Kuronen, M., 2022: A Deeper Dive into the Very Severe Hail Designation | Building Enclosure. Accessed 16 February 2025, <https://www.buildingenclosureonline.com/articles/91170-a-deeper-dive-into-the-very-severe-hail-designation>.
- Lamb, D., and J. Verlinde, 2011: *Physics and Chemistry of Clouds*. Cambridge University Press, <https://doi.org/10.1017/CBO9780511976377>.
- Laskin, A., R. C. Moffet, M. K. Gilles, J. D. Fast, R. A. Zaveri, B. Wang, P. Nigge, and J. Shutthanandan, 2012: Tropospheric chemistry of internally mixed sea salt and organic particles: Surprising reactivity of NaCl with weak organic acids. *Journal of Geophysical Research: Atmospheres*, **117**, <https://doi.org/10.1029/2012JD017743>.
- Lata, N. N., and Coauthors, 2021: Aerosol Composition, Mixing State, and Phase State of Free Tropospheric Particles and Their Role in Ice Cloud Formation. *ACS Earth Space Chem.*, **5**, 3499–3510, <https://doi.org/10.1021/acsearthspacechem.1c00315>.
- Le, M., and V. Chandrasekar, 2021: Graupel and Hail Identification Algorithm for the Dual-frequency Precipitation Radar (DPR) on the GPM Core Satellite. *Journal of the Meteorological Society of Japan. Ser. II*, **99**, 49–65, <https://doi.org/10.2151/jmsj.2021-003>.
- Lehmann, J., and Coauthors, 2005: Near-edge X-ray absorption fine structure (NEXAFS) spectroscopy for mapping nano-scale distribution of organic carbon forms in soil: Application to black carbon particles. *Global Biogeochemical Cycles*, **19**, <https://doi.org/10.1029/2004GB002435>.
- Levi, L., and A. N. Aufdermaur, 1970: Crystallographic Orientation and Crystal Size in Cylindrical Accretions of Ice. *JAS*, **27**, 443–452.
- Lewis, K. A., J. Tzilivakis, D. J. Warner, and A. Green, 2016: An international database for pesticide risk assessments and management. *Human and Ecological Risk Assessment: An International Journal*, **22**, 1050–1064, <https://doi.org/10.1080/10807039.2015.1133242>.

- Li, L., and I. N. Sokolik, 2018: The Dust Direct Radiative Impact and Its Sensitivity to the Land Surface State and Key Minerals in the WRF-Chem-DuMo Model: A Case Study of Dust Storms in Central Asia. *Journal of Geophysical Research: Atmospheres*, **123**, 4564–4582, <https://doi.org/10.1029/2017JD027667>.
- Li, X., Q. Zhang, T. Zhu, Z. Li, J. Lin, and T. Zou, 2018: Water-soluble ions in hailstones in northern and southwestern China. *Sci Bull (Beijing)*, **63**, 1177–1179, <https://doi.org/10.1016/j.scib.2018.07.021>.
- Lin, T.-C., Y.-J. Shen, and M.-R. Wang, 2014: Agglomeration Processes and Mechanisms of CO₂ Snow Inside a Tube. *Aerosol Science and Technology*, **48**, 228–237, <https://doi.org/10.1080/02786826.2013.868597>.
- Lin, Y., and M. R. Kumjian, 2022: Influences of CAPE on Hail Production in Simulated Supercell Storms. *Journal of the Atmospheric Sciences*, **79**, 179–204, <https://doi.org/10.1175/JAS-D-21-0054.1>.
- Liu, E., S. Vega, M. D. Treiser, H.-J. Sung, and P. V. Moghe, 2011: Fluorescence Imaging of Cell–Biomaterial Interactions. *Comprehensive Biomaterials*, P. Ducheyne, Ed., Elsevier, 291–303, <https://doi.org/10.1016/B978-0-08-055294-1.00101-X>.
- Ludlam, F. H., 1980: *Clouds and Storms: The Behavior and Effect of Water in the Atmosphere*. First Edition. The Pennsylvania State University Press 405pp.
- Mahoney, K., 2020: Extreme Hail Storms and Climate Change: Foretelling the Future in Tiny, Turbulent Crystal Balls? *Bulletin of the American Meteorological Society*, **101**, S17–S22, <https://doi.org/10.1175/BAMS-D-19-0233.1>.
- Malečić, B., M. Telišman Prtenjak, K. Horvath, D. Jelić, P. Mikuš Jurković, K. Čorko, and N. S. Mahović, 2022: Performance of HAILCAST and the Lightning Potential Index in simulating hailstorms in Croatia in a mesoscale model – Sensitivity to the PBL and microphysics parameterization schemes. *Atmospheric Research*, **272**, 106143, <https://doi.org/10.1016/j.atmosres.2022.106143>.
- Mandrioli, P., G. L. Puppi, N. Bagni, and F. Prodi, 1973: Distribution of Microorganisms in Hailstones. *Nature*, **246**, 416–417, <https://doi.org/10.1038/246416a0>.
- Manoj, P., 2023: *Copper Oxychloride Market Report 2024 (Global Edition)*. Cognitive Market Research, accessed 2 September 2024, <https://www.cognitivemarketresearch.com/copper-oxychloride-market-report>.
- Martius, O., A. Hering, M. Kunz, A. Manzato, S. Mohr, L. Nisi, and S. Trefalt, 2018: Challenges and Recent Advances in Hail Research. *Bulletin of the American Meteorological Society*, **99**, ES51–ES54, <https://doi.org/10.1175/BAMS-D-17-0207.1>.
- Meneghini, R., T. Iguchi, S. Seto, N. Yoshida, J. Awaka, and T. Kubota, 2021: GPM/DPR Level 2 Algorithm Theoretical Basis Document (ATBD) | NASA Global Precipitation Measurement Mission. Accessed 4 February 2025,

<https://gpm.nasa.gov/resources/documents/gpmdpr-level-2-algorithm-theoretical-basis-document-atbd>.

- Mercer, I. P., 2005: PHYSICAL APPLICATIONS OF LASERS | Industrial Applications. *Encyclopedia of Modern Optics*, R.D. Guenther, Ed., Elsevier, 169–184, <https://doi.org/10.1016/B0-12-369395-0/00947-7>.
- Michaud, A. B., J. E. Dore, D. Leslie, W. B. Lyons, D. C. Sands, and J. C. Priscu, 2014: Biological ice nucleation initiates hailstone formation. *J. Geophys. Res. Atmos.*, **119**, 12,186–12,197, <https://doi.org/10.1002/2014JD022004>.
- Miller, L. J., J. D. Tuttle, and C. A. Knight, 1988: Airflow and Hail Growth in a Severe Northern High Plains Supercell. *Journal of the Atmospheric Sciences*, **45**, 736–762, [https://doi.org/10.1175/1520-0469\(1988\)045<0736:AAHGIA>2.0.CO;2](https://doi.org/10.1175/1520-0469(1988)045<0736:AAHGIA>2.0.CO;2).
- Moffet, R. C., A. V. Tivanski, and M. K. Gilles, 2011: *Scanning Transmission X-ray Microscopy: Applications in Atmospheric Aerosol Research*. Lawrence Berkeley National Lab. (LBNL), Berkeley, CA (United States), accessed 5 August 2023, <https://www.osti.gov/biblio/1005004>.
- Mokkapatil, S. P., 2009: Simulation of particle agglomeration using dissipative particle dynamics, accessed 9 March 2025, <https://hdl.handle.net/1969.1/ETD-TAMU-1149>.
- Mulholland, J. P., S. W. Nesbitt, R. J. Trapp, K. L. Rasmussen, and P. V. Salio, 2018: Convective Storm Life Cycle and Environments near the Sierras de Córdoba, Argentina. *Monthly Weather Review*, **146**, 2541–2557, <https://doi.org/10.1175/MWR-D-18-0081.1>.
- Munich RE, 2017: *TOPICS Geo Natural Catastrophes 2017*. Munich RE.
- Munich Re, 2018: Hail – An underestimated and growing risk. Accessed 16 February 2025, <https://www.munichre.com/en/insights/natural-disaster-and-climate-change/hail.html>.
- , 2020: Severe weather damage in Europe. Accessed 16 February 2025, <https://www.munichre.com/en/company/media-relations/media-information-and-corporate-news/media-information/2020/causing-billions-in-losses-dominate-nat-cat-picture-2019.html>.
- Murillo, E. M., and C. R. Homeyer, 2019: Severe Hail Fall and Hailstorm Detection Using Remote Sensing Observations. *JAMC*, **58**, 947–970, <https://doi.org/10.1175/JAMC-D-18-0247.1>.
- Murray, B. J., D. O’Sullivan, J. D. Atkinson, and M. E. Webb, 2012: Ice nucleation by particles immersed in supercooled cloud droplets. *Chem. Soc. Rev.*, **41**, 6519–6554, <https://doi.org/10.1039/C2CS35200A>.
- Nam, K. Y., and C. J. Lee, 2013: Characterization of Silver Nanoparticles Incorporated Acrylic-Based Tissue Conditioner with Antimicrobial Effect and Cytocompatibility. *Nanobiomaterials in Clinical Dentistry*, K. Subramani, W. Ahmed, and J.K. Hartsfield,

- Eds., William Andrew Publishing, 283–295, <https://doi.org/10.1016/B978-1-4557-3127-5.00014-3>.
- Narwade, S., M. C. Gaikwad, K. Fartade, S. Pawar, M. Sawdekar, and P. Ingale, 2014: *Mass Mortality of Wildlife due to Hailstorms in Maharashtra, India*. The Institute for Bird Population.
- Nelson, S. P., 1983: The Influence of Storm Flow Structure on Hail Growth. *Journal of Atmospheric Sciences*, **40**, 1965–1983, [https://doi.org/10.1175/1520-0469\(1983\)040<1965:TIOSFS>2.0.CO;2](https://doi.org/10.1175/1520-0469(1983)040<1965:TIOSFS>2.0.CO;2).
- Nesbitt, S. W., and Coauthors, 2021: A Storm Safari in Subtropical South America: Proyecto RELAMPAGO. *Bulletin of the American Meteorological Society*, **102**, E1621–E1644, <https://doi.org/10.1175/BAMS-D-20-0029.1>.
- Ni, X., C. Liu, D. J. Cecil, and Q. Zhang, 2017: On the Detection of Hail Using Satellite Passive Microwave Radiometers and Precipitation Radar. *J. Appl. Meteorol. Climatol.*, **56**, 2693–2709, <https://doi.org/10.1175/JAMC-D-17-0065.1>.
- Nixon, C. J., J. T. Allen, and M. Taszarek, 2023: Hodographs and Skew Ts of Hail-Producing Storms. *Weather and Forecasting*, **38**, 2217–2236, <https://doi.org/10.1175/WAF-D-23-0031.1>.
- Nousiainen, T., E. Zubko, J. V. Niemi, K. Kupiainen, M. Lehtinen, K. Muinonen, and G. Videen, 2009: Single-scattering modeling of thin, birefringent mineral-dust flakes using the discrete-dipole approximation. *Journal of Geophysical Research: Atmospheres*, **114**, <https://doi.org/10.1029/2008JD011564>.
- O'Connor, B., 1996: Confocal laser scanning microscopy; a new technique for investigating and illustrating fossil Radiolaria. *Micropaleontology*, **42**, 395–401.
- Orlando, A., F. Franceschini, C. Muscas, S. Pidkova, M. Bartoli, M. Rovere, and A. Tagliaferro, 2021: A Comprehensive Review on Raman Spectroscopy Applications. *Chemosensors*, **9**, 262, <https://doi.org/10.3390/chemosensors9090262>.
- Patnaude, R. J., R. J. Perkins, S. M. Kreidenweis, and P. J. DeMott, 2021: Is Ice Formation by Sea Spray Particles at Cirrus Temperatures Controlled by Crystalline Salts? *ACS Earth Space Chem.*, **5**, 2196–2211, <https://doi.org/10.1021/acsearthspacechem.1c00228>.
- Petrenko, V. F., and R. W. Whitworth, 1999: *Physics of Ice*. OUP Oxford 390pp.
- Pilorz, W., M. Zięba, J. Szturc, and E. Łupikasza, 2022: Large hail detection using radar-based VIL calibrated with isotherms from the ERA5 reanalysis. *Atmospheric Research*, **274**, 106185, <https://doi.org/10.1016/j.atmosres.2022.106185>.
- Pruppacher, H. R., 1972: Self-Diffusion Coefficient of Supercooled Water. *The Journal of Chemical Physics*, **56**, 101–107, <https://doi.org/10.1063/1.1676831>.

- Pruppacher, H. R., and J. D. Klett, 1980: *Microphysics of Clouds and Precipitation*. Springer Netherlands.
- Pucik, T., C. Castellano, P. Groenemeijer, T. Kuhne, A. T. Radler, B. Antonescu, and E. Faust, 2019: Large Hail Incidence and Its Economic and Societal Impacts across Europe. *Mon. Weather Rev.*, **147**, 3901–3916, <https://doi.org/10.1175/MWR-D-19-0204.1>.
- Punge, H. J., and M. Kunz, 2017: Hail observations and hailstorm characteristics in Europe: A review. *Atmospheric Research*, **176–177**, 159–184, <https://doi.org/10.1016/j.atmosres.2016.02.012>.
- , K. M. Bedka, M. Kunz, S. D. Bang, and K. F. Itterly, 2023: Characteristics of hail hazard in South Africa based on satellite detection of convective storms. *Natural Hazards and Earth System Sciences*, **23**, 1549–1576, <https://doi.org/10.5194/nhess-23-1549-2023>.
- Raja, P. M. V., and A. R. Barron, 2016: An Introduction to Energy Dispersive X-ray Spectroscopy. *Chemistry LibreTexts*. Accessed 3 August 2023, [https://chem.libretexts.org/Bookshelves/Analytical_Chemistry/Physical_Methods_in_Chemistry_and_Nano_Science_\(Barron\)/01%3A_Elemental_Analysis/1.12%3A_An_Introduction_to_Energy_Dispersive_X-ray_Spectroscopy](https://chem.libretexts.org/Bookshelves/Analytical_Chemistry/Physical_Methods_in_Chemistry_and_Nano_Science_(Barron)/01%3A_Elemental_Analysis/1.12%3A_An_Introduction_to_Energy_Dispersive_X-ray_Spectroscopy).
- Rangno, A. L., and P. V. Hobbs, 1991: Ice particle concentrations and precipitation development in small polar maritime cumuliform clouds. *Quarterly Journal of the Royal Meteorological Society*, **117**, 207–241, <https://doi.org/10.1002/qj.49711749710>.
- Rasmussen, K. L., and R. A. Houze Jr., 2016: Convective Initiation near the Andes in Subtropical South America. *Monthly Weather Review*, **144**, 2351–2374, <https://doi.org/10.1175/MWR-D-15-0058.1>.
- Rasmussen, K. L., M. D. Zuluaga, and R. A. Houze Jr., 2014: Severe convection and lightning in subtropical South America. *Geophysical Research Letters*, **41**, 7359–7366, <https://doi.org/10.1002/2014GL061767>.
- Raupach, T., and Coauthors, 2021a: The effects of climate change on hailstorms. *Nature Reviews Earth & Environment*, **2**, <https://doi.org/10.1038/s43017-020-00133-9>.
- Raupach, T. H., and Coauthors, 2021b: The effects of climate change on hailstorms. *Nat Rev Earth Environ*, **2**, 213–226, <https://doi.org/10.1038/s43017-020-00133-9>.
- Rausch, J., D. Jaramillo-Vogel, S. Perseguers, N. Schnidrig, B. Grobety, and P. Yajan, 2022: Automated identification and quantification of tire wear particles (TWP) in airborne dust: SEM/EDX single particle analysis coupled to a machine learning classifier. *Science of The Total Environment*, **803**, 149832, <https://doi.org/10.1016/j.scitotenv.2021.149832>.
- Raval, N., R. Maheshwari, D. Kalyane, S. R. Youngren-Ortiz, M. B. Chougule, and R. K. Tekade, 2019: Importance of Physicochemical Characterization of Nanoparticles in Pharmaceutical Product Development. *Basic Fundamentals of Drug Delivery*, R.K. Tekade, Ed., *Advances*

- in Pharmaceutical Product Development and Research*, Academic Press, 369–400, <https://doi.org/10.1016/B978-0-12-817909-3.00010-8>.
- Recuperar S.R.L.: Fábrica de fertilizantes | Recuperar S.R.L. | Córdoba. *RECUPERAR*. Accessed 9 October 2024, <https://www.recuperarsrl.com.ar>.
- Ren, L., Y. Yang, H. Wang, P. Wang, L. Chen, J. Zhu, and H. Liao, 2021: Aerosol transport pathways and source attribution in China during the COVID-19 outbreak. *Atmospheric Chemistry and Physics*, **21**, 15431–15445, <https://doi.org/10.5194/acp-21-15431-2021>.
- Ritchie, N. W. M., 2010: Using DTSA-II to simulate and interpret energy dispersive spectra from particles. *Microsc Microanal*, **16**, 248–258, <https://doi.org/10.1017/S1431927610000243>.
- Rizobacter, Status ZN. Accessed 19 September 2024, <https://rizobacter.com.ar/es/productos/argentina/status-zn>.
- Rogers, R. R., and M. K. Yau, 1989: *A Short course in cloud physics*. 3rd ed. Burlington, Mass.: Butterworth Heinemann.
- Rosinski, J., and T. C. Kerrigan, 1969: The Role of Aerosol Particles in the Formation of Raindrops and Hailstones in Severe Thunderstorms.
- Sanchez-Marroquin, A., and Coauthors, 2020: Iceland is an episodic source of atmospheric ice-nucleating particles relevant for mixed-phase clouds. *Science Advances*, **6**, eaba8137, <https://doi.org/10.1126/sciadv.aba8137>.
- Sander, J., J. F. Eichner, E. Faust, and M. Steuer, 2013: Rising Variability in Thunderstorm-Related U.S. Losses as a Reflection of Changes in Large-Scale Thunderstorm Forcing. *Weather, Climate, and Society*, **5**, 317–331, <https://doi.org/10.1175/WCAS-D-12-00023.1>.
- Šantl-Temkiv, T., K. Finster, T. Dittmar, B. M. Hansen, R. Thyraug, N. W. Nielsen, and U. G. Karlson, 2013: Hailstones: A Window into the Microbial and Chemical Inventory of a Storm Cloud. *PLOS ONE*, **8**, 1–7, <https://doi.org/10.1371/journal.pone.0053550>.
- Sasaki, C. R. S., A. K. Rowe, L. A. McMurdie, and K. L. Rasmussen, 2022: New Insights into the South American Low-Level Jet from RELAMPAGO Observations. *Monthly Weather Review*, **150**, 161, <https://doi.org/10.1175/MWR-D-21-0161.1>.
- , ———, ———, A. C. Varble, and Z. Zhang, 2024: Influences of the South American Low-Level Jet on the Convective Environment in Central Argentina Using a Convection-Permitting Simulation, <https://doi.org/10.1175/MWR-D-23-0122.1>.
- Schaefer, V. J., 1941: A Method for Making Snowflake Replicas. *Science*, **93**, 239–240, <https://doi.org/10.1126/science.93.2410.239>.
- Schnell, G., S. Staehlke, U. Duenow, J. B. Nebe, and H. Seitz, 2019: Femtosecond Laser Nano/Micro Textured Ti6Al4V Surfaces—Effect on Wetting and MG-63 Cell Adhesion. *Materials*, **12**, 2210, <https://doi.org/10.3390/ma12132210>.

- Schütz, L., and M. Sebert, 1987: Mineral aerosols and source identification. *Journal of Aerosol Science*, **18**, 1–10, [https://doi.org/10.1016/0021-8502\(87\)90002-4](https://doi.org/10.1016/0021-8502(87)90002-4).
- Shanklin, R. L., 1989: *Wet Bulb Zero Heights as an Indicator of Surface Hail Size for the April 3, 1989 Severe Weather Episode*. National Weather Service Office.
- Smith, B. T., R. L. Thompson, J. S. Grams, C. Broyles, and H. E. Brooks, 2012: Convective Modes for Significant Severe Thunderstorms in the Contiguous United States. Part I: Storm Classification and Climatology. *Weather and Forecasting*, **27**, 1114–1135, <https://doi.org/10.1175/WAF-D-11-00115.1>.
- Soderholm, J. S., and M. R. Kumjian, 2023: Automating the analysis of hailstone layers. *Atmospheric Measurement Techniques*, **16**, 695–706, <https://doi.org/10.5194/amt-16-695-2023>.
- Sokolik, I. N., and O. B. Toon, 1996: Direct radiative forcing by anthropogenic airborne mineral aerosols. *Nature*, **381**, 681–683, <https://doi.org/10.1038/381681a0>.
- , and ———, 1999: Incorporation of mineralogical composition into models of the radiative properties of mineral aerosol from UV to IR wavelengths. *Journal of Geophysical Research: Atmospheres*, **104**, 9423–9444, <https://doi.org/10.1029/1998JD200048>.
- Stein, A. F., R. R. Draxler, G. D. Rolph, B. J. B. Stunder, M. D. Cohen, and F. Ngan, 2015: NOAA's HYSPLIT Atmospheric Transport and Dispersion Modeling System. *Bulletin of the American Meteorological Society*, **96**, 2059–2077, <https://doi.org/10.1175/BAMS-D-14-00110.1>.
- Steinke, I., and Coauthors, 2016: Ice nucleation activity of agricultural soil dust aerosols from Mongolia, Argentina, and Germany. *Journal of Geophysical Research: Atmospheres*, **121**, 13,559–13,576, <https://doi.org/10.1002/2016JD025160>.
- Takahashi, T., 1987: Hawaiian Hailstones—30 January 1985. *Bulletin of the American Meteorological Society*, **68**, 1530–1534, [https://doi.org/10.1175/1520-0477\(1987\)068<1530:HHJ>2.0.CO;2](https://doi.org/10.1175/1520-0477(1987)068<1530:HHJ>2.0.CO;2).
- Tarn, M. D., and Coauthors, 2018: The study of atmospheric ice-nucleating particles via microfluidically generated droplets. *Microfluid Nanofluidics*, **22**, 52, <https://doi.org/10.1007/s10404-018-2069-x>.
- Tegen, I., and A. A. Lacis, 1996: Modeling of particle size distribution and its influence on the radiative properties of mineral dust aerosol. *Journal of Geophysical Research: Atmospheres*, **101**, 19237–19244, <https://doi.org/10.1029/95JD03610>.
- Testa, B., and Coauthors, 2021: Ice Nucleating Particle Connections to Regional Argentinian Land Surface Emissions and Weather During the Cloud, Aerosol, and Complex Terrain Interactions Experiment. *Journal of Geophysical Research: Atmospheres*, **126**, e2021JD035186, <https://doi.org/10.1029/2021JD035186>.

- Turner, J. N., S. Lasek, and D. H. Szarowski, 2001: Confocal Optical Microscopy. *Encyclopedia of Materials: Science and Technology*, K.H.J. Buschow, R.W. Cahn, M.C. Flemings, B. Ilshner, E.J. Kramer, S. Mahajan, and P. Veysseyre, Eds., Elsevier, 1504–1509, <https://doi.org/10.1016/B0-08-043152-6/00271-0>.
- U.S. Geological Survey (USGS), 2019: *Minerals Yearbook, 2017-2018, Latin American And Canada*. U.S. Government Publishing Office 1069pp.
- Vali, G., P. J. DeMott, O. Möhler, and T. F. Whale, 2015: Technical Note: A proposal for ice nucleation terminology. *Atmospheric Chemistry and Physics*, **15**, 10263–10270, <https://doi.org/10.5194/acp-15-10263-2015>.
- Vander Wood, T. B., 1994: Automated Particle Analysis by Microscopy, A Primer. *Microscopy Today*, **2**, 13–17, <https://doi.org/10.1017/S1551929500063008>.
- Vander Wood, T. B., 2017: Particle Sizing in Emissions Samples by Scanning Electron Microscopy. *POWER Magazine*. Accessed 17 August 2023, <https://www.powermag.com/particle-sizing-in-emissions-samples-by-scanning-electron-microscopy/>.
- Varble, A. C., and Coauthors, 2021: Utilizing a Storm-Generating Hotspot to Study Convective Cloud Transitions: The CACTI Experiment, <https://doi.org/10.1175/BAMS-D-20-0030.1>.
- Wagner, J., Z.-M. Wang, S. Ghosal, and S. Wall, 2019: Source Identification on High PM_{2.5} Days Using SEM/EDS, XRF, Raman, and Windblown Dust Modeling. *Aerosol Air Qual. Res.*, **19**, 2578–2530, <https://doi.org/10.4209/aaqr.2019.05.0276>.
- Wang, S., and I. V. Larina, 2017: High-resolution imaging techniques in tissue engineering. *Monitoring and Evaluation of Biomaterials and their Performance In Vivo*, R.J. Narayan, Ed., Woodhead Publishing, 151–180, <https://doi.org/10.1016/B978-0-08-100603-0.00008-0>.
- Wang, S., L. Mu, C. Wang, X. Li, J. Xie, Y. Shang, H. Pu, and M. Dong, 2024: Modeling and Simulation of Micron Particle Agglomeration in a Turbulent Flow: Impact of Cylindrical Disturbance and Particle Properties. *ACS Omega*, **9**, 49302–49315, <https://doi.org/10.1021/acsomega.4c06441>.
- Wang, X., C. Zhang, T. Shi, D. Zhang, P. Zhao, and P. Zhao, 2023: Case Investigation on the Influence of In-Snow Particles' Size and Composition on the Snow Light Absorption and Albedo. *Geophysical Research Letters*, **50**, e2023GL103362, <https://doi.org/10.1029/2023GL103362>.
- Wu, W., W. Huang, L. Deng, and C. Wu, 2022: Investigation of Maximum Hail-Size Forecasting Using Bulk Microphysics Schemes. *Monthly Weather Review*, **150**, 2503–2525, <https://doi.org/10.1175/MWR-D-21-0312.1>.
- Yadav, S. K., S. K. Kompalli, B. R. Gurjar, and R. K. Mishra, 2021: Aerosol number concentrations and new particle formation events over a polluted megacity during the COVID-19

- lockdown. *Atmospheric Environment*, **259**, 118526, <https://doi.org/10.1016/j.atmosenv.2021.118526>.
- Zaccarini, F., G. Garuti, A. Ortiz-Suarez, and A. Carugno-Duran, 2004: THE PARAGENESIS OF PYROPHANITE FROM SIERRA DE COMECHINGONES, CÓRDOBA, ARGENTINA. *The Canadian Mineralogist*, **42**, 155–168, <https://doi.org/10.2113/gscanmin.42.1.155>.
- Zhang, Z., Y. Zhou, X. Zhu, L. Fei, H. Huang, and Y. Wang, 2020: Applications of ESEM on Materials Science: Recent Updates and a Look Forward. *Small Methods*, **4**, 1900588, <https://doi.org/10.1002/smt.201900588>.
- Zhao, B., and Coauthors, 2019: Ice nucleation by aerosols from anthropogenic pollution. *Nat*, **12**, 602–607, <https://doi.org/10.1038/s41561-019-0389-4>.
- Zhou, Z., Q. Zhang, J. T. Allen, X. Ni, and C.-P. Ng, 2021: How Many Types of Severe Hailstorm Environments Are There Globally? *Geophysical Research Letters*, **48**, e2021GL095485, <https://doi.org/10.1029/2021GL095485>.
- Zipser, E. J., S. W. Nesbitt, C. Liu, and D. P. Yorty, 2006: Where Are the Most Intense Thunderstorms on Earth? *B AM METEOROL SOC*, 1057–1071, <https://doi.org/10.1175/BAMS-87-8-1057>.